Doctoral Dissertation

博士論文

Role of Mean Motion Resonances in Planetesimal Accretion onto Proto-Gas Giant Planets

(原始巨大ガス惑星への微惑星集積における平均運動共鳴の役割)

A Dissertation Submitted for the Degree of Doctor of Philosophy
December 2020

令和 2 年 12 月博士（理学）申請

Department of Earth and Planetary Science, Graduate School of Science
The University of Tokyo

東京大学大学院理学系研究科地球惑星科学専攻

Sho Shibata

柴田 翔

Abstract

The formation of gas giant planets is a complicated process composed of many underlying physical sub-processes such as circumstellar disk evolution, core formation, gas accretion, and planetary migration. Thanks to progresses in respective theoretical studies, we can construct unified planetary formation models from planetesimals to gas giant planets; however, there are still many uncertainties related to each process and initial conditions. The bulk composition of gas giant planets is used for retrieving the information of planetary formation because the composition evolution of gas giant planets is strongly related to the evolution paths of gas giant planets. According to the theoretical estimation (Thorngren et al. 2016, The Astrophysical Journal, 831, 64) based on transit observations, close-in gas giant planets contain large amounts of heavy elements, suggesting need for an additional process for increasing the amount of heavy elements other than the standard formation processes. Planetesimal accretion is regarded as one of the main sources of such massive heavy elements; however, how many planetesimals can be captured by a gas giant planet has not been known because of a lack of understanding about the role of mean motion resonances in planetary migration phase. In this thesis, we focus on the role of mean motion resonances in the planetesimal accretion onto a migrating proto-gas giant planet. Using numerical simulations, we show that mean motion resonances play an important role in the planetesimal accretion. Comparing the numerical results with the theoretical estimations of heavy elements contents, we discuss the formation history of gas giant planets.

Chapter 1 is the introduction and chap. 2 is the review of the important physics in planetesimal accretion and mean motion resonances. Using those parameters, we show the reason why the mean motion resonances are expected to play important roles in planetesimal accretion onto a migrating proto-gas giant planet.

In chap 3, we consider the limiting case where the mean motion resonances with a migrating planet work most strongly with the aim to reveal the fundamental physics of mean motion resonances in planetesimal accretion. Using direct orbital integration of planetesimals, we find that mean motion resonances play important roles in planetesimal accretion. Planetesimal accretion is inhibited by two kinds of shepherding, aerodynamic shepherding and resonant shepherding. When both shepherdings become ineffective, planetesimal accretion occurs efficiently. The relatively narrow region of a circumstellar disk where planetesimal accretion occurs is named as the sweet spot in this thesis. The total amount of planetesimals captured by the migrating planet increases with the amount of planetesimals shepherded into the sweet spot during the planetary migration. Deriving the conditions of the sweet spot analytically, we find that the location of the sweet spot barely depends on the structure and evolution of the circumstellar

disk.

In chap 4, we focus on the effects of high-velocity mutual collisions of planetesimals. Such collisions have a possibility to break the resonant trapping, which is an important process triggered by mean motion resonances. We derive the condition for breaking the resonant trapping analytically and find that the planetesimal collisions are strong enough to break the resonant trapping. Including the effect of planetesimal collisions in orbital integration code, we investigate the effect of high-velocity collisions on planetesimal accretion. Using the numerical simulations, we find that high-velocity collisions break the resonant trapping and change the total amount of captured planetesimals by a factor of ~ 2 at most. On the other hand, the location of the sweet spot is barely changed by the high-velocity collisions.

In chap. 5, we discuss the effect of planetesimal accretion on the composition evolution of gas giant planets. Using the results obtained above, we construct a simple model for estimating the amount of heavy elements brought by planetesimal accretion. Our model shows that a Jupiter-mass planet can capture the large amount of planetesimals if the core forms in the outer disk. The amount of heavy elements in gas giant planets increases with the semi-major axis of core formation location and strongly depends on the planetesimal disk mass. Due to the planetesimal accretion in planetary migration phases, gas giant planets currently observed in the region interior to the sweet spot have more heavy elements than those exterior to the sweet spot. Comparing the theoretically and observationally estimated amounts of heavy elements in close-in gas giant planets, we conclude that close-in gas giant planets migrated over tens AU in their formation stages and the migration distance was longer for heavier planets. The large scattering in the amount of heavy elements likely comes from the circumstellar disk diversity. Our model also suggests that the extremely enriched close-in gas giant planets with more than $\sim 100 M_\oplus$ heavy elements formed via gravitational instability. The planetesimal accretion model can explain the various characteristics found in the heavy element contents of close-in gas giant planets. If we can observe the amount of heavy elements in gas giant planets orbiting far from their central star, we can constrain the source of heavy elements more strongly.

In chap. 6, we make future prospects and summarise this thesis.

In this thesis, we have focused on the role of mean motion resonances in planetesimal accretion, which is neglected in previous studies of the formation of gas giant planets. We have found that mean motion resonances regulate the location where planetesimal accretion occurs and increase the efficiency of planetesimal accretion. The numerical calculations performed in this thesis shed light on the importance of mean motion resonances and show that mean motion resonances affect the heavy element contents in gas giant planets. The amounts of heavy elements in gas giant planets mainly depend on the migration distance of those planets and the size of the planetesimal disk. These results show that the migration distances of gas giant planets can be retrieved from the amounts of heavy elements and that the various features found in the heavy element contents in close-in gas giant planets can be explained by the planetesimal accretion. The findings in this thesis make a great contribution in linking the current composition of gas giant planets with their formation history. Along with the future development of observation and characterisation of exoplanets, the formation paths of gas giant planets will be constrained by the models including the effects

of planetesimal accretion in planetary migration phase.

Contents

Chapter 1

General Introduction

The formation of gas giant planets is one of the main topics in planetary science. The final goal of the field of giant planets formation is clarifying when and where formation of gas giant planets starts and how the planets evolve in a circumstellar disk and explaining the observed diversity of exoplanetary systems.

Formation of gas giant planets is a complicated process composed of many underlying physical sub processes. The main ingredients of planet formation are circumstellar disk evolution, core formation, gas accretion and planetary migration. Thanks to progresses in respective theoretical studies, we can construct unified planetary formation models from the growth of planetesimals to the termination of gas giant planet formation. However, there are still many uncertainties related with each processes and initial conditions, which are not observable in current planetary systems. Updating proposed theories using observed physical parameters is crucial for understanding the formation of gas giant planets. Along with the development of observation and characterisation of exoplanets, many studies have tried to validate theoretically proposed formation models and give constraints to the initial parameters shaping the formation fields of gas giant planets. Chemical composition of gas giant planets is one of the notable characteristics because the formation history of gas giant planets is imprinted in the current composition of gas giant planets. Recently, composition data of exoplanets have been obtained and used for retrieving the initial conditions of planetary formation. Studies connecting the observed composition and formation processes of gas giant planets are required for further progress in the field of planet formation.

1.1 Formation of gas giant planets

There are two competing theories for gas giant planet formation. The first one is referred to the *disk instability model*, where gas giant planets form directly from the circumstellar disk gas. A massive gaseous disk triggers gravitational instability and formed fragments collapse into massive planets. The possibility of disk instability was suggested in Kuiper (1951) and Cameron (1978). Recent computational methods enable a quantitative discussion of disk instability (e.g. Boss 1997, 2019). The final mass of gas giant planets formed through disk instability is regulated by the wavelength of the instability and the typical planet mass is a few Jupiter-masses (Rafikov 2005). The second formation model is referred to the *core accretion model*, where a massive solid core triggers the

rapid accretion of surrounding disk gas on top of the core (Perri & Cameron 1974; Mizuno 1980). In the core accretion model, the final mass of gas giant planets is regulated by the amount of available disk gas around the planets. The core accretion model has a potential to form gas giant planets with various masses as observed in our solar system and exoplanetary systems (Tanigawa & Ikoma 2007; Tanigawa & Tanaka 2016; Tanaka et al. 2020). In this thesis, we consider the formation of gas giant planets through the core accretion model.

The core accretion model requires a seed object, the mass of which exceeds a certain critical mass prior to the dissipation of the circumstellar disk gas. The critical mass of the seed object, which ends up a core of a giant planet, is estimated as tens of Earth-masses for a solar-composition envelop (Perri & Cameron 1974; Mizuno 1980; Ikoma et al. 2000). Hori & Ikoma (2011) investigated the contraction of envelopes polluted by falling solid materials and found that the critical core mass was reduced by the envelope pollution. The critical core mass is theoretically estimated to be much smaller than $\sim 10 M_\oplus$ (Venturini et al. 2015, 2016). Cores of the critical mass must be formed by the dissipation time of circumstellar disks, which is typically estimated as a few Myr (Haisch, Jr. et al. 2001; Briceño et al. 2001; Hillenbrand et al. 2008). Formation of solid cores of the critical mass within a few Myr is a long standing problem in gas giant planet formation, as described below.

There are two typical formation processes of cores of gas giant planets; planetesimal accretion and pebble accretion. In the case of planetesimal accretion, planetesimals continue to grow by their mutual collisions. The growth speed of planetesimals depends on the gravitational focusing effect, which increases the planetesimal-planetesimal collision cross-section. Small relative velocities between planetesimals enhances the gravitational focusing effect and results in a high collision probability. Due to the aerodynamic gas drag, collisional damping and dynamical friction, relative velocities are kept small enough to trigger the so-called *runaway growth* (Greenberg et al. 1978; Wetherill & Stewart 1989, 1993; Kokubo & Ida 1996). In the runaway growth mode, growth timescale is shorter for larger planetesimals, which brings a situation where a small difference in mass originated among planetesimals is rapidly magnified. As a consequence of the runaway growth, a small population of large bodies called planetary embryos, or simply embryos, is formed. These embryos keep their orbital separations. The growth of the embryos are brought by the accretion of surrounding small planetesimals. The relative velocities between the embryos and the planetesimals increase with the embryos mass and the gravitational focusing effect vanishes for massive embryos. After the end of the runaway growth, the embryos grow in the so-called *oligarchic growth* mode (Kokubo & Ida 1998, 2000). In the oligarchic growth mode, growth timescale is longer for larger embryos. The oligarchic growth mode leads to the formation of a small number of roughly-equal-mass protoplanets.

The growth of protoplanets in the runaway/oligarchic growth modes continues until planetesimals around the protoplanets are depleted. The final mass of protoplanets is determined by the isolation mass. The orbital separation between protoplanets is about 10 mutual Hill radii (Kokubo & Ida 2000, 2002). In this case, the isolation mass of protoplanets around 5 AU in the minimum-mass solar nebula (Hayashi 1981) is $\sim 3 M_\oplus$. The final mass of protoplanets, however, is reduced by other effects. For massive protoplanets ($\sim 1 M_\oplus$), close encounters

with protoplanets tend to result in scattering of planetesimals away rather than accretion of planetesimals (Lin & Ida 1997). Scattering of planetesimals reduces the collision probability and limits the growth of the protoplanet (Levison et al. 2010). On the other hand, the fragmentation of planetesimals brought by collisions between planetesimals results in depletion of planetesimals (Inaba & Ikoma 2003; Kobayashi et al. 2010). The relative velocities between planetesimals are excited by the gravitational scattering of protoplanets. High-velocity collisions lead to breaking planetesimals and ejecting numerous fragments. Ejected fragments trigger the further destructive collisions; such a phenomena is called the collision cascade (e.g. Tanaka et al. 1996; Kobayashi & Tanaka 2010). At the end of the collision cascade, fragments are small ($\sim 10\mathrm{m}$) enough to drift out from the formation region of planets before being accreted by the protoplanets. The depletion of planetesimals stop the growth of protoplanets and makes it difficult to form solid cores triggering rapid gas accretion in outer disk (Inaba & Ikoma 2003; Kobayashi et al. 2011). To solve this problem, Inaba & Ikoma (2003) investigated the effects of protoplanet's atmosphere, which enhances the collision probability of small fragments, and Kobayashi et al. (2016) and Kobayashi & Tanaka (2018) investigated the effects of turbulent disk, which weakens the depletion of planetesimals. According to their results, the cores with critical mass can be formed before disk dissipation.

The second formation path of solid cores triggering rapid gas accretion is the pebble accretion (mm-cm size solid materials). The pebble accretion was first suggested by Ormel & Klahr (2010) and investigated in detail by Lambrechts & Johansen (2012). The pebble-protoplanet collision cross-section is much larger than that of planetesimal-protoplanet or planetesimal-planetesimal. If the orbits of pebbles are deflected by the protoplanet gravity, the pebbles feel strong gas drag due to the increased relative velocity with the surrounding disk gas. The gas drag exerted on pebbles is much stronger than that of planetesimals and comparable to the protoplanet gravity. The orbit of pebbles are deflected in the direction onto the protoplanet. For the optimally-accreted pebbles, the accretion radius of pebbles extends to the Bondi radius, which is defined using the relative velocity between protoplanets and pebbles instead of the sound speed of disk gas, and the pebble accretion rate increases with the protoplanet mass (Lambrechts & Johansen 2012). Due to the rapid drift of pebbles from the outer disk, protoplanets continue pebble accretion without the depletion of solid materials. If a seed protoplanet of Moon-mass is formed in the disk, pebble accretion can form a core of several Earth-masses before disk dissipation (Johansen & Lambrechts 2017). Pebble accretion continues until the protoplanet reaches the pebble isolation mass (Morbidelli & Nesvorny 2012), at which a gap is opened in the circumstellar gas disk and pebbles are halted at the local pressure bump. The pebble isolation mass depends on the disk condition, such as disk viscosity and disk scale height, and is estimated from several Earth-masses to several tens Earth-masses (Bitsch et al. 2018). Thus, the formation path of cores with critical mass exists in the pebble accretion scenario.

The formation of gas giant planets' cores has still been actively discussed. However, both planetesimal accretion model and pebble accretion model (and combined model) enable the formation of cores with critical mass in the wide range of gas giant planets before disk dissipation. Thus, gas giant planets can start their formation in the wide region of circumstellar disk (Bitsch et al. 2015;

Kobayashi & Tanaka 2018; Bitsch et al. 2019). After reaching the critical core mass, the protoplanet enters the so-called *runaway gas accretion phase*. The gas accretion rate in this runaway phase is investigated by the 1D (Pollack et al. 1996; Tajima & Nakagawa 1997; Ikoma et al. 2000) and 3D numerical simulations (Kurokawa & Tanigawa 2018; Lambrechts et al. 2019). In both simulations, the gas accretion rate is regulated by the quasi-static contraction, or cooling, of a nearly hydrostatic envelope. The accretion rate increases with the planetary mass because the surface area of the contracting envelop expands and total luminosity increases. In any simulations, the gas accretion timescale of a Jupiter-mass planet is much shorter than the disk dissipation timescale. This rapid gas accretion is halted by the supply limitation of disk gas. The gas accretion mode shifts into the so-called *detached phase*, or *supply-limited phase*, when the potential gas accretion rate in the runaway mode exceeds the maximum supply rate of disk gas. The maximum supply rate of disk gas is determined by the local gas flow around the Hill sphere (Tanigawa & Watanabe 2002; Machida et al. 2010) and global radial disk flow, or disk accretion rate (Tanigawa et al. 2014; Tanaka et al. 2020). Using 2D hydrodynamic simulations of accretion flow onto a growing planet, Tanigawa & Watanabe (2002) found the existence of accretion bands through which disk gas flows into the Hill sphere. These accretion bands were also found in 3D hydrodynamic simulations (Machida et al. 2010) and the gas accretion rate decreases with planetary mass once the planet mass exceeds a certain mass. The gap formation in a circumstellar disk is also suggested as a cause of reducing the gas accretion rate in the supply-limited phase (Tanigawa & Ikoma 2007; Tanigawa et al. 2014). The gas accretion onto gas giant planets is finally terminated by disk dissipation. The timing of the onset of runaway gas accretion is an important parameter that determines the final mass of forming gas giant planets.

Another important mechanism in the formation of gas giant planets is planetary migration. Planets embedded in a circumstellar disk exert positive torques on the outer part of the disk and negative torques on the inner part of the disk through the gravitational interaction (e.g. Lin & Papaloizou 1979; Goldreich & Tremaine 1980). If the planet is small, the gravitational torque is smaller than the disk's viscous torque that the differential rotating annuli of the disk exert on each other and the global surface density profile is not changed. In this case, the planet migrates in the type I regime (e.g. Ward 1997; Tanaka et al. 2002; Paardekooper et al. 2010). Once the gravitational torque overwhelms the disk's viscous torque, the planet opens a gap in the gas disk around its orbit. Planetary migration regime shits into the type II regime (e.g. Lin & Papaloizou 1993). The mass of planets at which a gap opens in the disk depends on the disk conditions, however, protoplanets open the gap and their migration shift to the type II regime soon after the onset of the runaway gas accretion.

In the classical model of type II migration, planets migrate with the disk gas which radially drifts due to the viscous torque because the gap is assumed to be deep enough that disk gas cannot cross the gap bottom. The planet is locked in the gap and viscously accreting disk gas pushes the planet. Hydrodynamic simulations, however, showed that the gap is not deep enough even if the planet is as massive as Jupiter (Duffell & Macfadyen 2013; Fung et al. 2014; Kanagawa et al. 2015, 2016, 2017). Due to the existence of gas flow crossing the gap bottom, the planetary migration timescale differs from that in the classical regime (Duffell

et al. 2014; Dürmann & Kley 2015; Kanagawa et al. 2018). Kanagawa et al. (2018) suggested that the torque exerted on the planet came from the Lindblad torques at the gap bottom. The formulae obtained in Kanagawa et al. (2018) showed that planetary migration speed in the type II regime is slower than that in the classical picture with appropriate disk viscosity. The planetary migration is also stopped by the disk dissipation.

After the onset of runaway gas accretion, the formation of gas giant planets is controlled by the gas accretion and planetary migration. The recent population synthesis models focus on the evolution track of planets with respect to semi-major axis and planetary mass (Ida & Lin 2004a,b, 2005, 2008, 2010; Mordasini et al. 2009a,b; Bitsch et al. 2015; Ndugu et al. 2018). Ida et al. (2018) suggested that the distribution of observed gas giant planets in exoplanetary systems could be reproduced by the effect of slow type II planetary migration suggested by Kanagawa et al. (2018). Assuming that not only the planetary migration timescale but also the gas accretion timescale depends on the gap structure, Tanaka et al. (2020) also modeled the evolution track of gas giant planets and found that the mass distribution of observed gas giant planets in exoplanetary systems can be explained with the observed mass distribution of circumstellar disks. Considering the pebble accretion for the formation of cores with critical mass, Bitsch et al. (2015) suggested that gas giant planets observed in the inner disk region had migrated over several tens AU radial distances. The differences between above models come from the different formation ingredients, such as core formation, gas accretion and planetary migration, used in each models. Each formation process has uncertainties coming from the model assumptions or numerical simulation settings. In addition, some of these processes are related with each other because both gas accretion and planetary migration processes are affected by the density profile of surrounding disk gas and the planet also affects on the disk gas profile. Comparing with the observed physical parameters, we can constrain the complicated formation models. Thus, it is important to use the various observed physical parameters not only the semi-major axis and mass of gas giant planets.

1.2 Composition evolution of gas giant planets

Recent observations and characterisation of exoplanets shed light on the chemical composition of gas giant planets. Metallicity and amount of heavy elements are most used composition parameters for gas giant planets. Heavy elements are materials heavier than hydrogen and helium and the metallicity is the mass fraction of heavy elements. The composition of gas giant planets was first constrained for the solar-system giant planets Jupiter and Saturn (e.g. Guillot 1999; Saumon & Guillot 2004). Gravitational moments observed by spacecrafts observations give the constraints on the mass distribution in gas giant planets. The bulk amount of heavy elements and the distribution of heavy elements have been estimated in Jupiter and Saturn. The gravitational moments observed by Juno spacecraft (Bolton et al. 2017) show the possibility of discontinuity in the heavy elements distribution in Jupiter envelope (Wahl et al. 2017; Nettelmann 2017; Guillot et al. 2018). Using various internal models suggested by the observed gravitational moments, Wahl et al. (2017) estimated the bulk amount of heavy

elements in Jupiter $M_{\rm Z,Jup}$ as $\sim$ 24-46$M_\oplus$ ($M_\oplus$: Earth mass), which is the sum of the core $\sim$ 6.2-24$M_\oplus$ and the heavy elements in envelope $\sim$ 3.3-40$M_\oplus$. The gravitational moments for Saturn have been observed by Cassini spacecraft. The estimated bulk amount of heavy elements in Saturn $M_{\rm Z,Sat}$ is $\sim$ 16-30$M_\oplus$, which is the sum of the core $\sim$ 5-20$M_\oplus$ and the heavy elements in envelope $\sim$ 0-7$M_\oplus$ (e.g. Helled 2019). The existence of cores is consistent with the core accretion model; however, the enriched envelope of Jupiter and the difference of metallicity between Jupiter and Saturn bring a question for the origin of those heavy elements. The gaseous envelopes come from the circumsolar disk gas whose bulk composition is the same as the solar composition. Due to the condensation of solid materials, the metallicity of circumsolar disk gas is less than the solar metallicity. Both Jupiter and Saturn, however, have higher bulk metallicities than the solar metallicity and core of critical mass is not enough to explain the origin of the estimated bulk metallicity.

In exoplanetary systems, the enrichment of gas giant planet metallicity has also been discovered (Guillot et al. 2006; Miller & Fortney 2011; Thorngren et al. 2016). After the end of the rapid gas accretion, gas giant planets keep loosing their internal thermal energy through their surface radiative emission. The radius of gas giant planets shrinks with time and this process is called thermal evolution. Given the planetary mass, radius and age, a thermal evolution model constrains the internal bulk metallicity of a gas giant planet. According to the results by Thorngren et al. (2016), close-in gas giant planets contain large amounts of heavy elements. The bulk metallicities of those planets are much higher than the central star's metallicity. Surprisingly, some of those planets contain more than $\sim 100M_\oplus$ heavy elements.

From the above observational facts, the metallicity enhancement of gas giant planets is considered as an universal process accompanying the formation of gas giant planets. High metallicity of gas giant planets requires the enrichment of disk gas metallicity or the additional accretion of solid materials. The disk enrichment mechanisms are proposed to be brought by the dissipation of disk gas due to photo-evaporation concentrating heavy elements (Guillot et al. 2006). Pebbles drifting in radial direction transport condensed materials from outer to inner disk and increase the metallicity of disk gas around snow lines due to the sublimation of volatile ices (Booth et al. 2017; Booth & Ilee 2019). Accretion of these enriched disk gas brings large amount of heavy elements in gas giant planets. The enrichment of disk gas metallicity is at most 20 times larger than the metallicity of central star, however, such highly enriched disk is limited in the narrow region around the snow lines. The additional accretion of solid materials is also regarded as potential sources of large amounts of heavy elements. The pebble accretion is halted by the gap formation as above, so the accretion of larger solid materials than pebbles is required for the accretion of large amounts of heavy elements. Giant impact of protoplanets was investigated as a source of massive heavy element contents (Ikoma et al. 2006; Liu et al. 2015, 2019; Ginzburg & Chiang 2020). Liu et al. (2019) investigated the giant impact of embryos to explain the heavy element distribution in Jupiter. Ginzburg & Chiang (2020) focused on the multiple giant impacts and derived the frequency of giant impacts of equally growing gas giant planets. In their model, the highly enriched planets more than $M_{\rm Z,tot} \sim 100M_\oplus$ needs several times impacts of planets containing massive solid core $\sim 30M_\oplus$ The critical core mass, however, is

estimated smaller as shown above. Accretion of enriched disk gas and giant impact of other protoplanet increases the metallicity of gas giant planets, however, the accretion of $\gtrsim 100 M_\oplus$ heavy elements as found in Thorngren et al. (2016) is difficult.

Planetesimal accretion after the onset of runaway gas accretion is also considered as a source of heavy elements in gas giant planets. Even after the onset of runaway gas accretion, planetesimals are left around the growing protoplanet. With the rapid increase of planetary mass, the feeding zone of the protoplanet (see the definition in sec. 2.3) expands and engulfs the surrounding planetesimals. Continuous supply of planetesimals to the feeding zone also brings a large amount of planetesimals onto the growing protoplanet (Zhou & Lin 2007; Shiraishi & Ida 2008; Shibata & Ikoma 2019). In addition, additional supply of planetesimals to the feeding zone takes place by the planetary migration (Tanaka & Ida 1999; Alibert et al. 2005; Mordasini et al. 2016). The amount of planetesimals accreting onto gas giant planets would depend on the radial migration distance of the planets. The migration distance largely differs between formation models of gas giant planets and is from less than few AU (Tanaka et al. 2020) to more than tens AU (Bitsch et al. 2015, 2019). If the planetesimal accretion occurs in planetary migration phase, the amounts of heavy elements in gas giant planets would indicate the migration distance of the planets. It is important to investigate the planetesimal accretion along the evolution track of gas giant planets for clarifying the origin of heavy elements observed in gas giant planets.

Considering the composition evolution of gas giant planets, many studies try to retrieve the initial formation conditions from the observed composition of exoplanets (Madhusudhan et al. 2014, 2017; Mordasini et al. 2016; Hasegawa et al. 2018, 2019; Notsu et al. 2020). Changing the formation area of solid cores, Madhusudhan et al. (2017) estimated the final composition of gas giant planets considering the enrichment of envelopes due to pebble accretion. They succeeded in linking the current atmospheric composition with where the solid core formed in the disk. Hasegawa et al. (2018, 2019) considered planetesimal accretion after the onset of the runaway gas accretion and estimated the metallicity of gas giant planets. Their result suggests that close-in gas giant planets had migrated from outer disk region. Mordasini et al. (2016) also linked the atmospheric composition of gas giant planets with their formation history using the population synthesis model. In above models, the effects of planetesimal accretion in planetary migration phase is neglected (Madhusudhan et al. 2017; Hasegawa et al. 2018, 2019) or included but simplified using an analytical model (Madhusudhan et al. 2014; Mordasini et al. 2016). The difference of the modeling about planetesimal accretion comes from the lack in the understanding of planetesimal accretion in planetary migration phase. The basic physics of planetesimal accretion during migration of gas giant planets is not clear because of the lack in the numerical simulations using direct orbital integration in the planetary migration phase. The accretion of planetesimals onto a migrating planet was investigated by Tanaka & Ida (1999). They used the direct orbital integration of planetesimals; however their main purpose was accelerating the formation of Jupiter core and the numerical calculation was performed with planets of a few Earth-masses. In the cases of Jupiter-mass planets, their result might be significantly altered by the mean motion resonances, the effects of which are neglected in Tanaka & Ida (1999). Mean motion resonances are more effective for heavier

planets (e.g. Murray & Dermott 1999) and known to play important roles in the orbital evolution of planetesimals (Walsh et al. 2011; Batygin & Laughlin 2015). We will give a detailed review in sec. 2. Thus, we need to investigate the planetesimal accretion onto a migrating proto-gas giant planet using the direct orbital integration method.

1.3 Objective of this doctoral thesis

Formation of gas giant planets is a complicated process composed of many underlying physical sub processes. We can construct unified planetary formation models from the growth of planetesimals to the termination of gas giant planet formation, however, there are still many uncertainties related with each processes and initial conditions. Along with the development of observation and characterisation of exoplanets, many studies have tried to validate theoretically proposed formation models and give constraints to the initial conditions of planetary formation. Recently, composition data of exoplanets have been obtained and used for retrieving the initial conditions. Studies connecting the observed composition and formation processes of gas giant planets are required for further progress in the field of planet formation. Planetesimal accretion is considered as an important source of heavy elements in gas giant planets, however, the basic physics of planetesimal accretion during migration of gas giant planets is not clear because of the lack in the numerical simulations. In this study, we focus on the effects of mean motion resonances on planetesimal accretion which have not been investigated so far.

The main purpose of this thesis is investigating the role of mean motion resonances in the planetesimal accretion onto gas giant planets. In chap. 2, we review the important physics of planetesimal accretion, including Jacobi energy and mean motion resonances. We show the importance of mean motion resonances for planetesimal accretion onto a migrating Jupiter-mass planet. In chap. 3, we consider the extreme cases where the effects of mean motion resonances work most effectively. Using the orbital integration method, we investigate the planetesimal accretion onto a migrating gas giant planet and reveal the fundamental roles of mean motion resonances in planetesimal accretion. Standing on the results obtained in chap. 3, we focus on the break of resonant trapping in chap. 4. We consider the break of mean motion resonances via mutual collisions of planetesimals and investigate the effect of resonant breaking on the planetesimal accretion. In chap. 5, we investigate the possibility of massive planetesimal accretion during the formation of gas giant planets using the results in chap. 3 and 4. We discuss the origin of heavy elements in gas giant planets in exoplanetary systems and in the solar system. And in chap. 6, we conclude and summarise this thesis.

Chapter 2

Review of mean motion resonances and planetesimal accretion

2.1 Mean motion resonances

In this section, we review the basic physics of mean motion resonances and introduce some important resonance parameters. We consider the motion of two particles with mass m and m' orbiting around a central star with mass m_c. The orbital elements of the inner particle are given by a (semi-major axis), e (eccentricity), i (inclination), Ω (longitude of ascending node), ϖ (longitude of pericenter) and ε (mean longitude at epoch), respectively. λ is a mean longitude defined as

$$\lambda = nt + \varepsilon, \tag{2.1}$$

where n is the mean motion. The orbital parameters of the outer particle are denoted with prime. When the mean motion of the inner particle has a simple relation with that of the outer particle, namely

$$\frac{n'}{n} \sim \frac{p}{p+q}, \tag{2.2}$$

where p and q are integers, the inner particle is in the $p+q:p$ mean motion resonance with the outer one. In this case, the conjunction with the outer particle is limited at some fixed points on the orbit. The accumulative gravitational perturbation from the outer particle deforms the orbit of the inner particle significantly.

2.1.1 Disturbing function and Lagrange's equations

To derive the change rates of orbital elements by mean motion resonances, we introduce the disturbing function $\mathscr{R}$ ($\mathscr{R}'$), which is the potential of the inner (outer) particle associated with perturbation from the outer (inner) particle. The disturbing function is given as (Murray & Dermott 1999)

$$\mathscr{R} = \frac{\mathscr{G}m'}{m_c} \sum_{j_i} S\cos\varphi, \tag{2.3}$$

$$\mathscr{R}' = \frac{\mathscr{G}m}{m_c} \sum_{j_i} S\cos\varphi, \tag{2.4}$$

where

$$S \approx \frac{f(\alpha)}{a'} e^{|j_4|} e'^{|j_3|} s^{|j_6|} s'^{|j_5|}, \tag{2.5}$$

with $\mathscr{G}$ is a gravitational constant, $f(\alpha)$ is a function of Laplace coefficients (see Murray & Dermott 1999), $s = \sin 1/2i$, $s' = \sin 1/2i'$, and ϕ is an argument given by

$$\varphi = j_1\lambda' + j_2\lambda + j_3\varpi' + j_4\varpi + j_5\Omega' + j_6\Omega, \tag{2.6}$$

with j_i being integers that sustain the d'Alembert relation

$$\sum_{i=1}^{6} j_i = 0. \tag{2.7}$$

The function S indicates the strength of each term of the disturbing function. The disturbing function is given as an infinite series and each term contains $\cos\varphi$. Outside the mean motion resonances, $\cos\varphi$ changes on the conjunction timescale because the argument φ increases or decreases with time. Inside the $p+q:p$ mean motion resonance, however, there is a resonant argument that barely changes with time because the time derivative of the resonant argument $\dot{\varphi}$ is given as

$$\dot{\varphi} \sim (p+q)n' - pn \sim 0. \tag{2.8}$$

In the long-term orbital evolution, integrated terms except the resonant terms of the disturbing function are almost zero. Thus, the orbital evolution of particles in mean motion resonances are regulated by only a few resonant terms in the disturbing function.

Considering the long period orbital evolution of each particle, we integrate and average Lagrange's equations of motion below. As discussed above, almost all terms except the resonant terms in the disturbing function are negligibly small. In practice, we use the averaged disturbing function $\langle\mathscr{R}\rangle$ and $\langle\mathscr{R}'\rangle$ given as

$$\langle\mathscr{R}\rangle = \frac{\mathscr{G}m'}{a'}\left[\mathscr{R}_{\rm D}^{(\rm sec)} + e^{|j_4|}e'^{|j_3|}s^{|j_6|}s'^{|j_5|}\{f_{\rm d}(\alpha) + f_{\rm e}(\alpha)\}\cos\varphi\right], \tag{2.9}$$

$$\langle\mathscr{R}'\rangle = \frac{\mathscr{G}m}{a}\left[\alpha\mathscr{R}_{\rm D}^{(\rm sec)} + e^{|j_4|}e'^{|j_3|}s^{|j_6|}s'^{|j_5|}\{\alpha f_{\rm d}(\alpha) + f_{\rm i}(\alpha)\}\cos\varphi\right], \tag{2.10}$$

where $\alpha = a/a'$, $\mathscr{R}_{\rm D}^{(\rm sec)}$ is a secular term, and $f_{\rm d}$, $f_{\rm e}$ and $f_{\rm i}$ are a direct term, external indirect term and internal indirect term, respectively (see also below). The equations of motion in orbital elements are called as Lagrange's equations and written with the disturbing function. The Lagrange's equations in the lowest-order terms in terms of e and i are given by

$$\dot{a} = \frac{2}{na}\frac{\partial\langle\mathscr{R}\rangle}{\partial\lambda}, \tag{2.11}$$

$$\dot{e} = -\frac{1}{na^2e}\frac{\partial\langle\mathscr{R}\rangle}{\partial\varpi}, \tag{2.12}$$

$$\tag{2.13}$$

$p+q:p$	$f_{\rm s}$	$f_{\rm d}$
2:1	0.387627	−1.19049
3:2	1.15279	−2.02521
4:3	2.27923	−2.84042
5:4	3.76541	−3.64962

Table 2.1: Values of the secular term $f_{\rm s}$ and the direct term $f_{\rm d}$ for the first order mean motion resonances.

Hereafter, we consider a restricted three-body problem where the perturbing particle is much heavier than the perturbed particle ($m \ll m'$ or $m \gg m'$) and the former is in a circular orbit. Both particles move on the reference plane. This situation is close to the cases that we consider in the following chapters. The averaged disturbing function is reduced to

$$\langle \mathscr{R} \rangle = \frac{\mathscr{G}m'}{a'} \left[f_{\rm s}(\alpha) e^2 + f_{\rm d}(\alpha) e^{|j_4|} \cos\varphi \right], \tag{2.14}$$

$$\left\langle \mathscr{R}' \right\rangle = \frac{\mathscr{G}m}{a} \left[\alpha f_{\rm s}(\alpha) e^2 + \alpha f_{\rm d}(\alpha) e^{|j_3|} \cos\varphi' \right], \tag{2.15}$$

where $f_{\rm s}$ is a secular term coming from $\mathscr{R}_{\rm D}^{(\rm sec)}$. The resonant arguments are

$$\varphi = j_1\lambda' + j_2\lambda + j_4\varpi, \tag{2.16}$$

$$\varphi' = j_1\lambda' + j_2\lambda + j_3\varpi'. \tag{2.17}$$

We can reduce the above equations of motion for the inner particle into

$$\dot{n} = 3 j_2 C_{\rm r} n e^{|j_4|} \sin\varphi, \tag{2.18}$$

$$\dot{e} = j_4 C_{\rm r} e^{|j_4|-1} \sin\varphi, \tag{2.19}$$

with

$$C_{\rm r} = \frac{m'}{m_{\rm c}} n \alpha f_{\rm d}(\alpha), \tag{2.20}$$

and for the outer particle into

$$\dot{n}' = 3 j_1 C_{\rm r}' n' e'^{|j_3|} \sin\varphi', \tag{2.21}$$

$$\dot{e}' = j_3 C_{\rm r}' e'^{|j_3|-1} \sin\varphi', \tag{2.22}$$

with

$$C_{\rm r}' = \frac{m}{m_{\rm c}} n' f_{\rm d}(\alpha). \tag{2.23}$$

Table 2.1 gives the values of $f_{\rm s}$ and $f_{\rm d}$.

2.1.2 Libration timescale and resonant width

Inside the mean motion resonances, the resonant argument librates on a libration timescale $\tau_{\rm lib}$. Along with the libration of the resonant argument, the semi-major

axis of the inner and outer particle also librate and the maximum change in the semi-major axis $\delta a_{\max}$ and $\delta a'_{\max}$ can be written as (Murray & Dermott 1999)

$$\frac{\delta a_{\max,\pm}}{a} = \pm\left(\frac{16}{3}\frac{|C_{\rm r}|}{n}e\right)^{1/2}\left(1+\frac{1}{27{j_2}^2e^3}\frac{|C_{\rm r}|}{n}\right)^{1/2} - \frac{2}{9j_2e}\frac{|C_{\rm r}|}{n}, \tag{2.24}$$

$$\frac{\delta a'_{\max,\pm}}{a'} = \pm\left(\frac{16}{3}\frac{|C'_{\rm r}|}{n'}e'\right)^{1/2}\left(1+\frac{1}{27{j_1}^2e'^3}\frac{|C'_{\rm r}|}{n'}\right)^{1/2} - \frac{2}{9j_1e'}\frac{|C'_{\rm r}|}{n'}. \tag{2.25}$$

The libration timescale of internal and external resonances are (Murray & Dermott 1999)

$$\tau_{\rm lib} = \frac{2\pi}{n}\left|\left|\frac{j_2}{j_1}\right|^{4/3}\left(\frac{m'}{m_c}\right)^2\frac{{f_{\rm d}}^2(\alpha)}{e^2} - 3{j_2}^2\left|\frac{j_2}{j_1}\right|^{2/3}\frac{m'}{m_c}f_{\rm d}(\alpha)e\right|^{-1/2}, \tag{2.26}$$

$$\tau'_{\rm lib} = \frac{2\pi}{n'}\left|\left(\frac{m}{m_c}\right)^2\frac{{f_{\rm d}}^2(\alpha)}{e'^2} - 3{j_1}^2\frac{m}{m_c}f_{\rm d}(\alpha)e'\right|^{-1/2}. \tag{2.27}$$

Figure 2.1 shows the locations of the three first-order inner mean motion resonances with a Jupiter-mass planet orbiting at 5AU in the a-e plane. Inside the color-coded regions, the resonant arguments librate on a timescale of $\tau_{\rm lib}$ and the semi-major axis and eccentricity of the perturbed particle evolve according to eq. (2.18) and eq. (2.19). The width of the resonance is defined as

$$\Delta a_{\rm res} = |\delta a_{\max,+} - \delta a_{\max,-}|, \tag{2.28}$$

and takes the minimum value at

$$e = \frac{2^{1/3}}{3}\left(|j_1|^{-2/3}|j_2|^{-4/3}f_{\rm d}\frac{m}{m_{\rm c}}\right)^{1/3}. \tag{2.29}$$

2.2 Resonant trapping

When the radial distance between two objects decreases, which is referred to convergent orbital evolution, the objects reach the position of a mean motion resonance and are locked in a resonant state. This phenomena is known as a resonant capture or resonant trapping. Resonant trapping has been discussed in the contexts of formation of satellite pairs (Goldreich 1965; Dermott et al. 1988; Malhotra 1993b), transport of small bodies (Yu & Tremaine 2001; Batygin & Laughlin 2015) and formation of exoplanet pairs (Fabrycky et al. 2014; Goldreich & Schlichting 2014); see references in Batygin (2015). Not all resonant encounters result in the resonant trapping because resonant trapping requires several conditions. Here, we consider the trap of a planetesimal in the inner mean motion resonances with a planet migrating inward. We assume the mass of the planetesimal is negligibly small relative to the mass of the planet. In this case, the resonant trapping requires the following conditions (e.g. Malhotra 1993a): (i) the orbits of the planetesimal and the planet converge with each other, (ii) the eccentricity of the planetesimal before being trapped in the resonance is smaller than the critical value $e_{\rm crit}$ (see eq. (2.31)), (iii) the timescale for the planetesimal

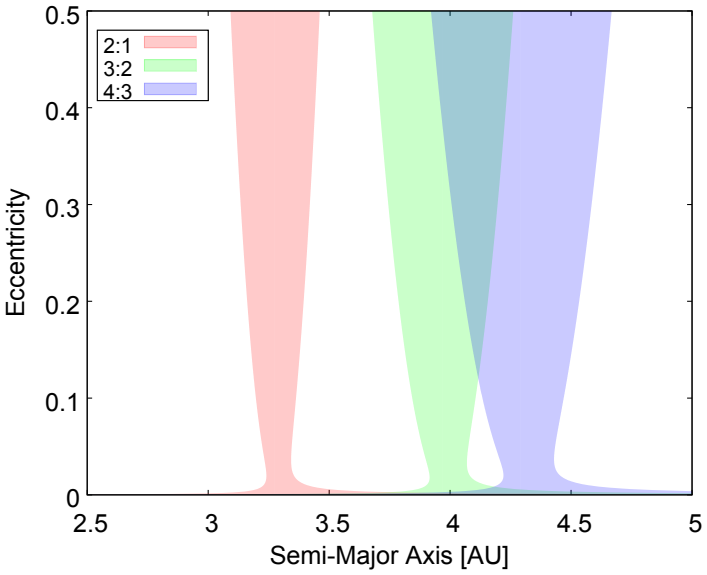

Figure 2.1: The locations of the first-order mean motion resonances with a Jupiter-mass planet at 5AU in the a-e plane. Here, we show the $2:1$ (red), $3:2$ (green) and $4:3$ (blue) resonances.

to cross the resonant width $\tau_{\rm cross}$ is longer than the libration timescale $\tau_{\rm lib}$ (see eq. (2.26) and (2.27)).

The first condition can be obtained by comparing the timescales of change in the semi-major axis of the planetesimal and the planet. In a circumstellar gas disk, orbits of objects shrink or (are damped) by the aerodynamic gas drag and gravitational tidal drag from the disk gas. The former drag is dominant for planetesimal-size objects ($\lesssim 10^{24}$g) and the latter drag is for planet-size objects ($\gtrsim 10^{24}$g) (Zhou & Lin 2007). Given the aerodynamic damping timescale of semi-major axis $\tau_{{\rm damp},a}$ for the planetesimal and the tidal damping timescale of semi-major axis $\tau_{{\rm tide},a}$ for the planet, we obtain the first condition as

$$\tau_{{\rm damp},a} > \tau_{{\rm tide},a}. \tag{2.30}$$

For the $j:j-1$ first-order resonances, the critical eccentricity is given by (e.g. Murray & Dermott 1999)

$$e_{\rm crit} = \sqrt{6}\left[\frac{3}{f_{\rm d}}(1-j)^{4/3}\, j^{2/3}\frac{M_{\rm s}}{M_{\rm p}}\right]^{-1/3}, \tag{2.31}$$

where $M_{\rm p}$ and $M_{\rm s}$ are mass of planet and central star. When $\tau_{{\rm damp},a} \gg \tau_{{\rm tide},a}$, the timescale for the planetesimal to cross the resonant width $\tau_{\rm cross}$ is given as

$$\tau_{\rm cross} = \left|\frac{\Delta a_{\rm res}}{\dot{a}_{\rm c}}\right| \sim \left|\frac{\Delta a_{\rm res}}{a_{\rm c}}\right| \tau_{{\rm tide},a}, \tag{2.32}$$

where $a_{\rm c}$ is the semi-major axis of the resonance centre defined by

$$a_{\rm c} = \left(\frac{j-1}{j}\right)^{2/3} a_{\rm p}, \tag{2.33}$$

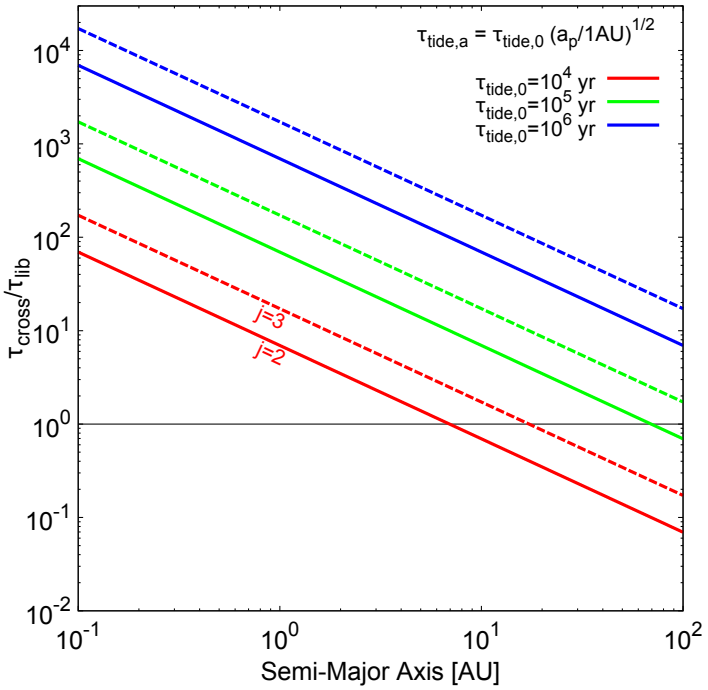

Figure 2.2: The ratio of the crossing timescale $\tau_{\rm cross}$ to the libration timescale $\tau_{\rm lib}$. Here, we consider a Jupiter-mass planet ($M_{\rm p}/M_{\rm s} = 10^{-3}$) and the type II regime for migration timescale $\tau_{{\rm tide},a}$ used in Ida & Lin (2004a), which is the same as the model used in chap. 3. Here, we show the cases of different scaling factor of migration timescale $\tau_{\rm tide,0}$ (see the definition in chap. 3) and $2:1$ (solid) and $3:2$ (dashed) resonances.

where $a_{\rm p}$ is the semi-major axis of the planet. Note that the resonance centre migrates with the same rate of the protoplanet during the planetary migration phase. Substituting eq. (2.29) into eq. (2.28), we obtain the minimum width of the resonance as

$$\left.\frac{\Delta a_{\rm res}}{a_{\rm c}}\right|_{\rm min} = 4.4 j^{-4/9}(j-1)^{1/9} {f_{\rm d}}^{2/3} \left(\frac{M_{\rm p}}{M_{\rm s}}\right)^{2/3}. \tag{2.34}$$

The corresponding libration timescale is

$$\tau_{\rm lib} = 0.87 j^{4/9}(j-1)^{-10/9} {f_{\rm d}}^{-2/3} \left(\frac{M_{\rm p}}{M_{\rm s}}\right)^{-2/3} T_{\rm K}, \tag{2.35}$$

where $T_{\rm K}$ is the Kepler period of the planetesimal. Using eqs. (2.32),(2.34) and (2.35), we obtain the third condition as

$$\frac{\tau_{\rm cross}}{\tau_{\rm lib}} = 5.1 j^{1/9}(j-1)^{2/9} {f_{\rm d}}^{4/3} \left(\frac{M_{\rm p}}{M_{\rm s}}\right)^{4/3} \frac{\tau_{{\rm tide},a}}{T_{\rm K,p}} \gtrsim 1, \tag{2.36}$$

where $T_{\rm K,p}$ is the Kepler period of the migrating planet.

Far from the planet and outside mean motion resonances, the eccentricity of the planetesimal is determined by a balance between the viscous stirring from

the planetesimal swarm and aerodynamic gas drag. The mean value of r.m.s. eccentricities of the planetesimal swarm is on the order of $\lesssim 10^{-2}$ (Ohtsuki et al. 2002). For km-size planetesimals with $e = 10^{-2}$, the radial drift timescale $\tau_{\mathrm{damp},a}$ is longer than the planetary migration timescale in the type II regime ($\tau_{\mathrm{tide},a} \lesssim 10^7$ yr) over a wide region of a circumstellar disk (Adachi et al. 1976). Also, the critical eccentricity is $e_{\mathrm{crit}} \sim 0.15$ for $j = 2$ and $M_{\mathrm{p}}/M_{\mathrm{s}} = 10^{-3}$. Thus, the first and second conditions are easily achieved. Figure 2.2 shows the timescale ratio $\tau_{\mathrm{cross}}/\tau_{\mathrm{lib}}$ as a function of the semi-major axis. Here, we show the case of Jupiter-mass planet ($M_{\mathrm{p}}/M_{\mathrm{s}} = 10^{-3}$) and consider the type II regime for the migration timescale $\tau_{\mathrm{tide},a}$ used in Ida & Lin (2004a) (see chap. 3). The ratio of timescales $\tau_{\mathrm{cross}}/\tau_{\mathrm{lib}}$ is larger than unity except for the case of rapid planetary migration $\tau_{\mathrm{tide},a} \sim 10^4$yr. Thus, we conclude that resonant trapping occurs during the migration of a gas giant planet at least once.

2.3 Feeding zone and planetesimal accretion

Here, we review the planetesimal accretion onto the protoplanet. First, we introduce the important physical parameter, the Jacobi energy E_{J}, and then, review the relation between the planetesimal accretion and the Jacobi energy. The review is based on the discussion in Shibata & Ikoma (2019). Here, we extend the discussion to the planetary migration phase and show the potential role of mean motion resonances in the accretion of planetesimals onto a migrating planet.

2.3.1 Jacobi Energy

In the late formation stage of gas giant planets, the mass of the protoplanet becomes much larger than the total mass of planetesimals surrounding the protoplanet. The gravitational tidal drag from the surrounding disk gas damps the eccentricity of the protoplanet and the orbit of the protoplanet is in almost circular orbit. The orbital evolution of planetesimals can be treated approximately as a restricted three-body problem, where the protoplanet is in a circular orbit and the gravitational forces exerted on the protoplanet from the surrounding planetesimals and mutual interaction among the planetesimals are negligible. In this case, the Jacobi energy is a useful parameter that regulates the orbital evolution of planetesimals (Hayashi et al. 1977). The Jacobi energy is defined as (e.g. Murray & Dermott 1999)

$$E_{\mathrm{jacobi}} \equiv \frac{1}{2} {v'_{\mathrm{pl}}}^2 + U_{\mathrm{jacobi}}, \tag{2.37}$$

$$U_{\mathrm{jacobi}} = -\frac{1}{2} {\Omega_{\mathrm{K,p}}}^2 \left(x'^2 + y'^2 \right) - \mathscr{G} \frac{M_{\mathrm{s}}}{r_{\mathrm{pl,s}}} - \mathscr{G} \frac{M_{\mathrm{p}}}{r_{\mathrm{pl,p}}} + U_0, \tag{2.38}$$

where $r_{\mathrm{pl,s}}$ is the distance between the planetesimal and the central star, $r_{\mathrm{pl,p}}$ is the distance between the planetesimal and the protoplanet, $\Omega_{\mathrm{K,p}}$ is angular velocity of the protoplanet, (x', y') and v'_{pl} are, respectively, the position and velocity of the planetesimal in the coordinate system co-rotating with the protoplanet. The constant U_0 is set such that U_{jacobi} vanishes at the Lagrange L_2 point. With orbital elements, the Jacobi energy of the planetesimal is expressed

as

$$E_{\rm jacobi} = \frac{\mathcal{G}M_{\rm s}}{a_{\rm p}} \left\{ -\frac{a_{\rm p}}{2a} - \sqrt{\frac{a}{a_{\rm p}}(1-e^2)}\cos i + \frac{3}{2} + \frac{9}{2}h^2 + O(h^3) \right\}, \tag{2.39}$$

where h is the reduced Hill radius defined as

$$h = \left(\frac{M_{\rm p}}{3M_{\rm s}} \right)^{1/3}. \tag{2.40}$$

In the vicinity of the protoplanet, eq. (2.39) can be written as

$$E_{\rm jacobi} \sim \frac{\mathcal{G}M_{\rm s}h^2}{a_{\rm p}} \left\{ \frac{1}{2}\left(\tilde{e}^2 + \tilde{i}^2\right) - \frac{3}{8}\tilde{b}^2 + \frac{9}{2} \right\}, \tag{2.41}$$

where

$$\tilde{b} \equiv \frac{a - a_{\rm p}}{h}, \tag{2.42}$$

$$\tilde{e} \equiv \frac{e}{h}, \tag{2.43}$$

$$\tilde{i} \equiv \frac{i}{h}. \tag{2.44}$$

We define the normalised Jacobi energy $\tilde{E}_{\rm jacobi}$ as

$$\tilde{E}_{\rm jacobi} = \frac{a_{\rm p}}{\mathcal{G}M_{\rm s}} \frac{E_{\rm jacobi}}{h^2}. \tag{2.45}$$

If $h \ll 1$, the constant $\tilde{E}_{\rm jacobi}$ lines are fixed in the $\tilde{b} - \tilde{e}$ plane even if the planetary mass increases or the protoplanet migrates in radial direction. Figure 2.3 shows the constant $\tilde{E}_{\rm jacobi}$ lines in the $\tilde{b} - \tilde{e}$ plane where $i \ll 1$ and $M_{\rm p}/M_{\rm s} = 10^{-3}$. The gray region where $\tilde{E}_{\rm jacobi} > 0$ corresponds to the so-called feeding zone.

The Jacobi energy is the total mechanical energy of a planetesimal defined in the coordinate system rotating with the protoplanet. The potential $U_{\rm jacobi}$ is the sum of the centrifugal potential and the gravitational potentials of the central star and the protoplanet. The potential curves in this coordinate are fixed for a given set of mass ratio $M_{\rm p}/M_{\rm s}$ and semi-major axis $a_{\rm p}$. Thus, the Jacobi energy is a constant of motion. As show in Fig. 2.4, there is a potential barrier for planetesimals to enter the Hill sphere of the protoplanet. Planetesimals initially having $\tilde{E}_{\rm jacobi} < 0$ cannot enter the Hill sphere because the gravitational force of the protoplanet does not change the Jacobi energy. Inside the feeding zone, planetesimals can enter the planet's Hill sphere and have possibilities to be captured by the protoplanet. To enter the Hill sphere, or to be captured by the protoplanet, planetesimals with negative value of $E_{\rm jacobi}$ need to increase their Jacobi energy.

The time derivative of the Jacobi energy at the feeding zone boundary is

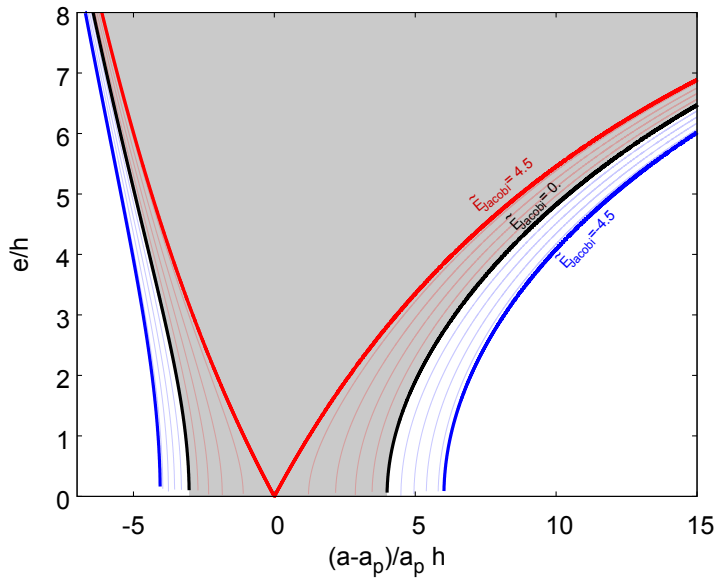

Figure 2.3: The constant $\tilde{E}_{\rm jacobi}$ lines in the $\tilde{b}-\tilde{e}$ plane when the planet-star mass ratio $M_{\rm p}/M_{\rm s}=10^{-3}$. The quantities $\tilde{E}_{\rm jacobi}$, $\tilde{b}$ and $\tilde{e}$ are defined by eqs. (2.45), (2.42) and (2.43), respectively. The red, black and blue lines show $\tilde{E}_{\rm jacobi}=4.5, 0, -4.5$, respectively. The gray region is the feeding zone.

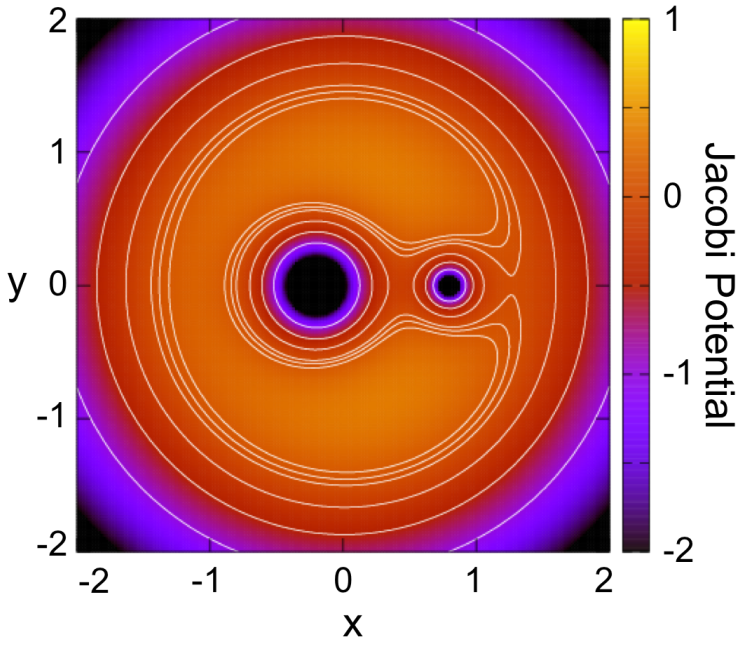

Figure 2.4: The map of the Jacobi potential $U_{\rm jacobi}$ on the rotating frame with the protoplanet. Here the planet-star mass ratio $M_{\rm p}/M_{\rm s}=10^{-1}$ and the mass centre is at the origin of the coordinate.

written as

$$\begin{aligned}\frac{\mathrm{d}\tilde{E}_{\mathrm{Jacobi}}}{\mathrm{d}t} =& \frac{1}{M_{\mathrm{p}}}\frac{\mathrm{d}M_{\mathrm{p}}}{\mathrm{d}t}3h^2 \\ &+\left(\frac{1}{a}\frac{\mathrm{d}a}{\mathrm{d}t}-\frac{1}{a_{\mathrm{p}}}\frac{\mathrm{d}a_{\mathrm{p}}}{\mathrm{d}t}\right)\left\{\frac{a_{\mathrm{p}}}{2a}-\frac{1}{2}\sqrt{\frac{a}{a_{\mathrm{p}}}(1-e^2)}\cos i\right\} \\ &+\frac{1}{e}\frac{\mathrm{d}e}{\mathrm{d}t}\frac{e^2}{\sqrt{1-e^2}}\sqrt{\frac{a}{a_{\mathrm{p}}}}\cos i \\ &+\frac{1}{i}\frac{\mathrm{d}i}{\mathrm{d}t}\sqrt{\frac{a}{a_{\mathrm{p}}}(1-e^2)}i\cos i. \end{aligned} \tag{2.46}$$

There are two factors that lead to increasing the Jacobi energy of planetesimals: (i) mass growth of the protoplanet, and (ii) convergence of the orbits of the planetesimal and protoplanet. The first one is most effective in the runaway gas accretion phase of the protoplanet. The second one is brought by the radial drift of planetesimals due to the aerodynamic gas drag, or planetary migration due to the gravitational tidal drag. As for gas giant planets, the type II migration is the most effective factor of orbital convergence. The eccentricity damping and inclination damping of planetesimals due to the aerodynamic gas drag from the disk gas always decreases the Jacobi energy. Thus, the accretion of planetesimals onto the gas giant planet occurs in the mass growth phase and planetary migration phase.

2.3.2 Planetesimal accretion onto a growing protoplanet

The accretion of planetesimals onto a protoplanet growing in situ via gas accretion has been investigated with numerical orbital integration of planetesimals by a few groups (Zhou & Lin 2007; Shiraishi & Ida 2008; Shibata & Ikoma 2019). Shiraishi & Ida (2008) considered that the accretion rate of planetesimals is determined by the surface density of planetesimals inside the feeding zone. From their numerical simulations, they found that the accretion of planetesimals in the protoplanet's mass growth phase is divided into two cases; *the nongap case* where planetesimals flow into the feeding zone smoothly, and *the gap case* where inflow of planetesimals is regulated by the competition between the expansion speed of the feeding zone and the damping speed of planetesimal orbits (or the competition between the growth timescale and the damping timescale). Shibata & Ikoma (2019) detailed the structure of the circumstellar disk in the vicinity of the massive protoplanet, including the gap formation, and investigated its effect on planetesimal accretion. They improved understanding of the mechanism of planetesimal inflow into the feeding zone using the change rate of the Jacobi energy (see eq. (2.46)). Performing the orbital integration of planetesimals with various disk models, planetary growth models and planetesimal sizes, which determine the value of $\dot{\tilde{E}}_{\mathrm{jacobi}}$, they concluded that the change rate of the Jacobi energy regulates the planetesimal accretion onto gas giant planets. According to the results in Shibata & Ikoma (2019), up to $\sim 30\%$ of planetesimals inside the feeding zone can be captured by the protoplanet until the end of the mass growth phase.

The role of the mean motion resonances on the planetesimal accretion was pointed in Zhou & Lin (2007). From their simulation, they found that the

planetesimals initially located inside mean motion resonances keep standing in for a while. Accretion timing of trapped planetesimals is, thus, delayed by the resonant trapping because trapped planetesimals avoid close-encounters with the protoplanet. The width of mean motion resonances expands with the planetary mass growth (see eq. (2.28)) and adjacent resonances overlap each other when the planet mass becomes larger than a certain mass. This phenomena is called as resonance overlap (e.g. Murray & Dermott 1999), which makes the resonance unstable and breaks the resonant trapping. In the mass growth phase, mean motion resonances change the timing of accretion of trapped planetesimals, but the capture probability is not affected by the resonances.

2.3.3 Planetesimal accretion onto a migrating protoplanet

The accretion of planetesimals onto a migrating planet was first investigated in the context of the formation of Jupiter's core. Ward (1986, 1989) suggested the acceleration of planetesimal accretion by the low-mass planet migrating in the type I regime. Ward & Hahn (1995) investigated whether the migrating planet can capture the planetesimals considering the interaction between the protoplanet and the planetesimal disk, which is a group of planetesimals in circumstellar disk. According to their result, a small protoplanet, which migrates slowly, makes a gap in the planetesimal disk and shepherds the inner planetesimals, which prevents planetesimal accretion. On the other hand, a large protoplanet, which migrates fast, cannot shepherd planetesimals and can capture planetesimals. Direct integration of planetesimal orbits around the migrating planet was performed by Tanaka & Ida (1999). Using the numerical results, they derived the threshold migration timescale for planetesimal accretion as

$$\tau_{\mathrm{tide},a,\mathrm{crit}} = 0.81 \left\{ \sqrt{1 + 0.45 \left(\frac{\tau_{\mathrm{damp},0}}{T_{\mathrm{K,p}}} \right)^{2/3}} + 1 \right\}^2 h^{-2} T_{\mathrm{K,p}}, \tag{2.47}$$

where $\tau_{\mathrm{damp},0}$ is the characteristic timescale of orbital damping due to disk gas drag (see eq. (3.25) in chap. 3). When $\tau_{\mathrm{tide},a} < \tau_{\mathrm{tide},a,\mathrm{crit}}$ (i.e. fast migration), the protoplanet rushes into the planetesimal disk and the planetesimals flow into the feeding zone smoothly. When $\tau_{\mathrm{tide},a} > \tau_{\mathrm{tide},a,\mathrm{crit}}$ (i.e. slow migration), however, planetesimals cannot enter the feeding zone. The former case is called as *predator* and the later case is called as *shepherding*. In their study, all the physical parameters are normalised and their results seem to be applicable for Jupiter-mass or more massive planets. In Tanaka & Ida (1999), however, the effects of mean motion resonances are artificially removed in the way explined below.

The effect of resonant trapping is important for orbital evolution of planetesimals around a migrating protoplanet, as shown in sec. 2.1. Even for the cases of Earth-mass planets, mean motion resonances can trap the planetesimals during planetary migration. Resonant trapping prevents planetesimals from entering the feeding zone of the migrating planet, because it stops their convergent orbital evolution. Tanaka & Ida (1997, 1999), however, assumed that the interactions between planetesimals break the resonant trapping immediately. The interactions between planetesimals like mutual collisions change the planetesimals' orbits and resonant arguments. The possibility of resonant breaking by the

collisions between planetesimals was investigated by Malhotra (1993a). Using the orbital integration, they found that the collision of planetesimals is strong enough to kick the trapped planetesimals out from the mean motion resonances with Earth-mass planets. Following that, Tanaka & Ida (1997, 1999) considered the limiting cases where the effects of mean motion resonances are perfectly removed by the interactions between planetesimals.

In the direct orbital integration, the required number of particles simulating the orbital evolution of planetesimals is larger than $\gtrsim 10^7$ if we consider the equal-size planetesimals of 10^7 cm in minimum mass solar nebula around 5AU. Orbital integration of such a huge number of particles takes too much calculation time. To reduce the calculation costs, many studies (Tanaka & Ida 1997, 1999; Zhou & Lin 2007; Shiraishi & Ida 2008; Levison et al. 2010; Shibata & Ikoma 2019) treated the planetesimals as test particles, which are mass less particles tracking the orbits of planetesimals and never exert gravitational forces on the other particles in the simulations. In the vicinity of the protoplanet, the gravitational scattering from the protoplanet dominates over the mutual gravitational interactions from planetesimals. So treating planetesimals as test particles is an appropriate modeling for investigating the accretion of planetesimals onto the growing protoplanet (Zhou & Lin 2007; Shiraishi & Ida 2008; Shibata & Ikoma 2019). In the planetary migration phase, however, test particles are trapped into the mean motion resonances of the migrating protoplanet. In some mean motion resonances, the interactions between planetesimals are important, as shown in Malhotra (1993a). To include the effect of breaking the resonant trapping, Tanaka & Ida (1997, 1999) artificially input the random perturbations on resonant arguments of test particles. By this artificial perturbations, test particles are free from the effects of mean motion resonances. As mentioned in Tanaka & Ida (1997), this manipulation makes their model the limiting case where the effects of mean motion resonances are perfectly removed. Their assumption is valid for the formation of Jupiter's core where $M_\mathrm{p} \sim M_\oplus$ and $a_\mathrm{p} \sim 5$AU, however not appropriate for the cases of migrating gas giant planets where $M_\mathrm{p} \sim M_\mathrm{Jup}$ and $a_\mathrm{p} \sim$ 1-100AU. The resonant trapping is stronger for heavier protoplanets because the width of resonances is larger for heavier protoplanets (see eq. (2.28)). In addition, the collision frequency of planetesimals decreases with the radial distance from the central star (see chap. 4). Thus, we need to consider the effect of mean motion resonances on the planetesimal accretion in the planetary migration phase of gas giant planets.

As shown in sec. 1, recent formation models of gas giant planets combining the gas accretion and planetary migration have been presented by many authors (Alibert et al. 2005; Madhusudhan et al. 2014, 2017; Mordasini 2018; Hasegawa et al. 2018, 2019). Some of those studies include the effect of planetesimal accretion of a migrating planet using the analytical formulae of solid accretion (e.g. Greenzweig & Lissauer 1992). In their model, the effects of expansion and move of the feeding zone are not included, so the cases where a large amount of planetesimals flow into or eliminate from the feeding zone are not considered. Alibert et al. (2005) considered that the planetesimals flow into the feeding zone smoothly if the condition $\tau_{\mathrm{tide},a} < \tau_{\mathrm{tide},a,\mathrm{crit}}$ is achieved, following Tanaka & Ida (1999), but the effects of mean motion resonances are not included. On the other hand, some studies (Madhusudhan et al. 2017; Hasegawa et al. 2018, 2019) neglect the planetesimal accretion in planetary migration phases because of the

low capture efficiency of planetesimals ($\lesssim 0.1$) for Earth-mass planets shown in Tanaka & Ida (1999). Those studies constructed the planetesimal accretion models standing on the results of Tanaka & Ida (1999), however, as described above, we need to consider the effects of mean motion resonances on planetesimal accretion appropriately especially in the case of massive migrating protoplanets.

Chapter 3

Accretion of Planetesimals under the Effective Resonant Trapping

3.1 Introduction

During the formation stages of gas giant planets, planetesimal accretion onto gas giant planets is an important factor of their composition evolution. Especially in the planetary migration phase, a large amount of planetesimals could accrete onto the planets. Around a massive planet, mean motion resonances are expected to play important roles in the orbital evolution of planetesimals, however, their effects on planetesimal accretion rate are not clear. As shown in chap. 2, mean motion resonances trap planetesimals and prevent the planetesimals from entering the feeding zone of the migrating planet. The accretion rate in this situation must be investigated by the direct orbital integration of planetesimals. In this chapter, we focus on the effects of mean motion resonances on planetesimal accretion onto a migrating proto-gas giant planet. We consider the limiting cases where mean motion resonances work most effectively, in contrast to Tanaka & Ida (1999). Analysing the numerical results, we will derive the required conditions for effective planetesimal accretion. Performing parameter studies with respect to the planetesimal size, migration timescale, migration distance and planet mass, we investigate how many planetesimals are captured by the migrating planet.

The method and model used in this chapter are written in sec. 3.2. In sec. 3.3, we show the results in the reference case. We analyse the results and reveal the fundamental physics which controls the planetesimal accretion in the planetary migration phase. We perform the parameter studies in sec. 3.4. Comparison with Tanaka & Ida (1999) and model limitations are discussed in sec. 3.5. And in sec. 3.6, we summarise this chapter. This chapter contains the results of Shibata et al. (2020).

3.2 Method and Model

In this study we assume the following situation: a giant planet has finished gas accretion and the planet is no longer growing in mass. The planet then migrates radially inward in the type II regime from a given semi-major axis in a circumstellar disk. Initially there are many single-sized planetesimals interior to the planet's orbit. The migrating planet then encounters these planetesimals

and captures some of them. The planetesimals are represented by test particles and, therefore are affected only by the gravitational forces from the central star and planet, and the drag force by the disk gas. The dynamical integration for these bodies is performed using the numerical simulation code developed in Shibata & Ikoma (2019). In the code, we integrate the equation of motion using the forth-order-Hermite integration scheme (Makino & Aarseth 1992). For timestep, we adopt the method of (Aarseth 1985). We summarise the method and the benchmark results in App. A.

3.2.1 Forces exerted on planetesimals and planet

The equation of motion is given by

$$\frac{\mathrm{d}\mathbf{r}_\mathrm{i}}{\mathrm{d}t} = \sum_{i \neq j} \mathbf{f}_{\mathrm{grav},i,j} + \mathbf{f}_\mathrm{aero} + \mathbf{f}_\mathrm{tide}, \tag{3.1}$$

where t is the time, $\mathbf{r}_i$ is the position vector relative to the initial (i.e., $t = 0$) mass centre of the star-planet-planetesimals system, $\mathbf{f}_{\mathrm{grav},i,j}$ is the mutual gravity between particles i and j given by

$$\mathbf{f}_{\mathrm{grav},i,j} = -\mathscr{G}\frac{M_\mathrm{j}}{{r_{i,j}}^3}\mathbf{r}_{i,j} \tag{3.2}$$

with $\mathbf{r}_{i,j}$ being the position vector of particle i relative to particle j ($r_{i,j} \equiv |\mathbf{r}_{i,j}|$), M_j is the mass of particle j, and $\mathscr{G}$ is the gravitational constant, $\mathbf{f}_\mathrm{aero}$ is the aerodynamic gas drag, and $\mathbf{f}_\mathrm{tide}$ is the gravitational tidal drag from the circumstellar disk gas. The central star, planet, and planetesimals are denoted by the subscripts i (or j) = 1, 2, and ≥ 3, respectively. The planetesimals are treated as test particles; therefore $f_{\mathrm{grav},i,j} = 0$ in Eq. (3.1) for $j \geq 3$. Also, given the range of the planetesimal mass ($\sim 10^{16}$-10^{22}g) and planet ($\sim 10^{30}$g), we assume $f_\mathrm{tide} = 0$ for the former and $f_\mathrm{aero} = 0$ for the latter. The central star is not affected by f_aero and f_tide.

3.2.2 Aerodynamic gas drag

The aerodynamic gas drag force is given by (Adachi et al. 1976)

$$\mathbf{f}_\mathrm{aero} = -\frac{\mathbf{u}}{\tau_\mathrm{aero}} = -\frac{1}{2m_\mathrm{pl}} C_\mathrm{d} \pi R_\mathrm{pl}^2 \rho_\mathrm{gas} u \mathbf{u}. \tag{3.3}$$

Here $\mathbf{u} = \mathbf{v}_\mathrm{pl} - \mathbf{v}_\mathrm{gas}$ ($u = |\mathbf{u}|$) is the planetesimal velocity ($\mathbf{v}_\mathrm{pl}$) relative to the ambient gas ($\mathbf{v}_\mathrm{gas}$), τ_aero is the timescale of aerodynamic gas drag, m_pl is the planetesimal's mass, C_d is the non-dimensional drag coefficient and given as $C_\mathrm{d} = 1$, ρ_gas is the gas density, and R_pl is the planetesimal's radius. The velocity and density of the ambient disk gas are calculated from the circumstellar disk model (see Section 3.2.4).

3.2.3 Gravitational tidal drag

We also consider the effect of the planetary migration of the gas giant planet, using the following form of the tidal drag force,

$$\mathbf{f}_\mathrm{tide} = -\frac{\mathbf{v}_\mathrm{p}}{2\tau_{\mathrm{tide},a}}, \tag{3.4}$$

where $\mathbf{v}_\mathrm{p}$ and $\tau_{\mathrm{tide},a}$ are the planet's velocity and the migration timescale, respectively. In this formula, the planet's eccentricity is assumed to be negligibly small. As for $\tau_{\mathrm{tide},a}$, we consider the planetary migration with the dependence on the planet's semi-major axis a_p being:

$$\tau_{\mathrm{tide},a} = \tau_{\mathrm{tide},0} \left(\frac{a_\mathrm{p}}{1\mathrm{AU}} \right)^{1/2}, \tag{3.5}$$

where the constant $\tau_{\mathrm{tide},0}$ is set as a free parameter. In type II regime, the dependence on a_p changes with the condition of surrounding disk gas and $\tau_{\mathrm{tide},0}$ depends on the planetary mass and the disk profiles around the planet (e.g. Lin & Papaloizou 1993; Kanagawa et al. 2018). However, we fix the exponent of a_p as 1/2, which is the limiting case where the planet mass is heavier than the surrounding disk gas, and $\tau_{\mathrm{tide},0}$ as constant in our simulation. This simplification allows a systematic investigation of the effect of planet migration on the efficiency of planetesimal accretion. The dependence of numerical results on migration timescale is discussed in sec. 3.5.1.

3.2.4 Disk model

We adopt the minimum-mass solar nebula model (Hayashi 1981) as our gas disk model. The surface density Σ_gas is expressed as

$$\Sigma_\mathrm{gas} = \Sigma_{\mathrm{gas},0} \left(\frac{r}{1\mathrm{AU}} \right)^{-\alpha_\mathrm{disk}}, \tag{3.6}$$

where r is a radial distance from initial mass centre of the star-planet system, $\Sigma_{\mathrm{gas},0} = 1.7 \times 10^3 \mathrm{g/cm}^3$ and $\alpha_\mathrm{disk} = 3/2$. The temperature of the circumstellar disk T_disk is given by:

$$T_\mathrm{disk} = T_{\mathrm{disk},0} \left(\frac{r}{1\mathrm{AU}} \right)^{-2\beta_\mathrm{disk}}, \tag{3.7}$$

where $T_{\mathrm{disk},0} = 280$ K and $\beta_\mathrm{disk} = 1/4$. The circumstellar disk being assumed to be vertically isothermal, the gas density ρ_gas is expressed as

$$\rho_\mathrm{gas} = \frac{\Sigma_\mathrm{gas}}{\sqrt{2\pi} h_\mathrm{s}} \exp\left(-\frac{z^2}{2{h_\mathrm{s}}^2} \right), \tag{3.8}$$

where z is the height from the disc mid-plane and h_s is the disk's scale height. The aspect ratio of the circumstellar disk is

$$\frac{h_\mathrm{s}}{r} = \frac{c_\mathrm{s}}{r\Omega_\mathrm{K}}, \tag{3.9}$$

where Ω_K is a Kepler angular velocity and c_s is a sound speed of disk gas. The sound speed is given as

$$c_\mathrm{s} = \sqrt{\frac{k_\mathrm{B} T_\mathrm{disk}}{\mu_\mathrm{disk} m_\mathrm{H}}} \propto r^{-\beta_\mathrm{disk}}, \tag{3.10}$$

where k_B is the Boltzmann constant and μ_disk is a mean molecular weight in a unit of proton mass m_H. In this study, μ_disk is set as 2.3 and the aspect ratio of the disk gas at 1AU is ~ 0.03.

The gas in the circumstellar disk rotates with a sub-Keplerian velocity because of pressure gradient; namely

$$v_{\rm gas} = v_{\rm K}\left(1-\eta_{\rm disk}\right) \tag{3.11}$$

with $\eta_{\rm disk}$ defined as

$$\eta_{\rm gas} \equiv -\frac{1}{2}\left(\frac{h_{\rm s}}{r}\right)^2 \frac{{\rm d}\ln P_{\rm gas}}{{\rm d}\ln r}, \tag{3.12}$$

$$= \frac{1}{2}\left(\frac{h_{\rm s}}{r}\right)^2 \left[\frac{3}{2}\left(1-\frac{z^2}{{h_{\rm s}}^2}\right) + \alpha_{\rm disk} + \beta_{\rm disk}\left(1+\frac{z^2}{{h_{\rm s}}^2}\right)\right], \tag{3.13}$$

where $P_{\rm gas}$ is the gas pressure. For deriving the above equation, we assume $\eta_{\rm gas} \ll 1$ and use the ideal-gas relation for isothermal sound speed, i.e., $c_{\rm s}^2 = P_{\rm gas}/\rho_{\rm gas}$.

3.2.5 Treatment of planetesimals

We adopt a simple disk model for the solid surface density $\Sigma_{\rm solid}$, which is expressed as

$$\Sigma_{\rm solid} = \Sigma_{\rm solid,0}\left(\frac{r}{1{\rm AU}}\right)^{-\alpha'_{\rm disk}} \tag{3.14}$$

In our model, we set $\alpha'_{\rm disk} = \alpha_{\rm disk} = 3/2$ and

$$\Sigma_{\rm solid,0} = Z_{\rm s}\Sigma_{\rm gas,0}, \tag{3.15}$$

where $Z_{\rm s}$ is the solid-to-gas ratio, which is assumed equal to the metallicity of the central star. The planetesimal's mass $m_{\rm pl}$ is calculated as $4\pi\rho_{\rm pl}{R_{\rm pl}}^3/3$, where $\rho_{\rm pl}$ is the planetesimal's mean density. The surface number density of planetesimals is given as $\Sigma_{\rm solid}/m_{\rm pl}$ which gives $\sim 10^6$ /AU^2 at maximum. To speed up the numerical integration, we adapt super-particles, which represent the orbits of several planetesimals, for the integration of planetesimal orbits.

We follow the orbital motion of super-particles, each of which contains several equal-size planetesimals. The super-particles are distributed in a given radial region, where the inner and outer edges are denoted by $a_{\rm pl,in}$ and $a_{\rm pl,out}$, respectively. The surface number density of super-particles $n_{\rm s}$ is given as

$$n_{\rm s} = n_{\rm s,0}\left(\frac{r}{1{\rm AU}}\right)^{-\alpha_{\rm sp}} \tag{3.16}$$

where

$$n_{\rm s,0} = \frac{N_{\rm sp}}{2\pi}\frac{2-\alpha_{\rm sp}}{\left(a_{\rm pl,out}/1{\rm AU}\right)^{2-\alpha_{\rm sp}} - \left(a_{\rm pl,in}/1{\rm AU}\right)^{2-\alpha_{\rm sp}}}\left[\frac{1}{\rm AU^2}\right]. \tag{3.17}$$

$N_{\rm sp}$ is the number of super-particles used in a given simulation. In our simulation, we set $N_{\rm sp} = 12{,}000$ and $\alpha_{\rm sp} = 1$, which distribute super-particles uniformly in radial direction. The mass per super-particle $M_{\rm sp}$ is given by

$$M_{\rm sp}(a_0) = \frac{\Sigma_{\rm solid}(a_0)}{n_{\rm s}(a_0)}, \tag{3.18}$$

where a_0 is the initial semi-major axis of the super-particle.

As for eccentricity and inclination, assuming that planetesimals are scattered by their mutual gravitational interaction, we adopt the Rayleigh distribution as the initial eccentricities e and inclinations i of planetesimals. We set $\langle e \rangle^{1/2} = 2\langle i \rangle^{1/2} = 10^{-3}$. The orbital angles Ω, ϖ and ε are distributed uniformly.

During the orbital integration, we judge that a super-particle has been captured by the planet once (i) the super-particle enters the planet's envelope or (ii) its Jacobi energy becomes negative in the Hill sphere. The planet's radius $R_{\rm p}$ is calculated as

$$R_{\rm p} = \left(\frac{3M_{\rm p}}{4\pi\rho_{\rm p}} \right)^{1/3}, \tag{3.19}$$

where $\rho_{\rm p}$ is the planet's mean density. We consider that the planet radius is still expanded because of the rapid gas accretion before planetary migration. We set $\rho_{\rm p} = 0.125$ g cm^{-3}, which gives two times expanded planetary radius for Jupiter-mass planet relative to the current Jupiter radius.

3.2.6 Model settings

In Sec. 3.3, we investigate the fundamental physics of the planetesimal accretion onto the migrating gas giant planet. The planetesimals are initially distributed in $a_{\rm pl,in} < r < a_{\rm pl,out}$ and $a_{\rm pl,in}$ is fixed at 0.3AU in our simulation. The planet is initially located in such a way that the inner boundary of the feeding zone is consistent with the outer edge of the planetesimals disk, namely

$$a_{\rm p,0} = \frac{a_{\rm pl,out}}{1 - 2\sqrt{3}h}. \tag{3.20}$$

The calculation is artificially stopped once the planet reaches the orbit of $a_{\rm p,f} = 0.5$AU. In Sec. 3.3, we investigate the planetesimal accretion in the reference case, where $\tau_{\rm tide,0} = 10^5$ yr, $R_{\rm pl} = 10^7$ cm, $a_{\rm pl,out} = 20$ AU and $M_{\rm p} = 10^{-3} M_{\rm s}$. In the reference case, the total amount of planetesimals are $M_{\rm tot} \sim 43 M_\oplus$. The choices of the parameter values for the reference model are summarised in Table 3.1. In Sec. 3.4, we perform a parameter study for different values of $\tau_{\rm tide,0}$, $R_{\rm pl}$, $a_{\rm pl,out}$ and $M_{\rm p}$ and investigate their effects on the captured heavy-element mass.

Again, in this study, to focus on the effect of planetary migration on the planetesimal accretion, we do not consider planetary growth nor disk evolution. While our setup is simplified, it allows us to identify the parameters that strongly influence the planetesimals orbital evolution and the efficiency of planetesimal accretion. This is discussed in detail in Sec. 3.5.

3.3 Results in reference case

3.3.1 Dynamics of planetesimals around a migrating planet

Figure 3.1 shows three snapshots of the orbital evolution of planetesimals for the reference case in the semimajor-axis vs. eccentricity plane. In each panel, the migrating planet is represented by the orange circle, while planetesimals of $\tilde{E}_{\rm jacobi} > 0$ and $\tilde{E}_{\rm jacobi} < 0$ are indicated by the red and blue circles, respectively.

M_s	Mass of central star	1.0	$M_\odot$
Z_s	Metallicity of central star	0.018	-
M_p	Mass of planet	1.0	M_{Jup}
R_p	Radius of planet	eq. (3.19)	
ρ_p	Mean density of planet	0.125	g cm^{-3}
$a_{p,0}$	Initial semi-major axis of planet	eq. (3.20)	
$a_{p,f}$	Final semi-major axis of planet	0.5	AU
$\tau_{tide,0}$	Scaling factor of migration timescale	1.0×10^5	yr
$\Sigma_{disk,0}$	Surface density of disk gas at 1AU	1.7×10^3	g/cm^2
$T_{disk,0}$	Temperature at 1AU	280	K
α_{disk}	Exponent of disk gas profile	3/2	-
β_{disk}	Exponent of disk temperature profile	1/2	-
R_{pl}	Radius of planetesimal	1.0×10^6	cm
$a_{pl,in}$	Inner edge of planetesimal disk	0.3	AU
$a_{pl,out}$	Outer edge of planetesimal disk	20	AU
α_{sp}	Exponent of test particle distribution	1	-
ρ_{pl}	Mean density of planetesimal	2.0	g cm^{-3}
N_{sp}	Initial number of super-particles	12 000	-

Table 3.1: Parameters used in the reference model.

The positions of the three mean motion resonances (MMRs) with the planet are indicated by the green-dotted lines. The orbital evolution of planetesimals is summarised below.

Panel (a): As the planet migrates inward, planetesimals encounter the planet and are trapped in the mean motion resonances; this phenomenon is referred to resonant trapping. The planetesimals trapped in the mean motion resonances are transported inward together with the migrating planet and their eccentricities are highly enhanced. This phenomena is known as *resonant shepherding* (Batygin & Laughlin 2015). Even entering the feeding zone, the trapped planetesimals are not captured by the planet due to the effect of mean motion resonances. In the resonant trapping, planetesimals are prevented from entering the planet's Hill sphere (see sec. 3.3.2 for more details), so no planetesimal accretion occurs in this phase.

Panel (b): Over the course of time, the resonantly-trapped planetesimals start to escape from the mean motion resonances. This is because the stronger aerodynamic drag in inner regions allows the planetesimals to escape from the mean motion resonances. The breakup of resonant trapping was investigated by Malhotra (1993a) in the context of the formation of Jupiter's core and by Goldreich & Schlichting (2014) in the context of the formation of multiple planetary systems. The break up shown in our simulation can be explained by the overstable liblation found in Goldreich & Schlichting (2014). The eccentricity of trapped planetesimal is excited by the planetary migration and damped by the disk gas drag at the same time. This overstable equilibrium condition makes the planetesimal orbit unstable and breaks the resonant trapping.

Panel (c): In the further inner region, the disk gas becomes dense enough that the resonantly-trapped planetesimals have their eccentricities damped faster than the planetary migration and, therefore, they are outside the feeding zone. We refer to this phenomenon as *aerodynamic shepherding*, which was found by

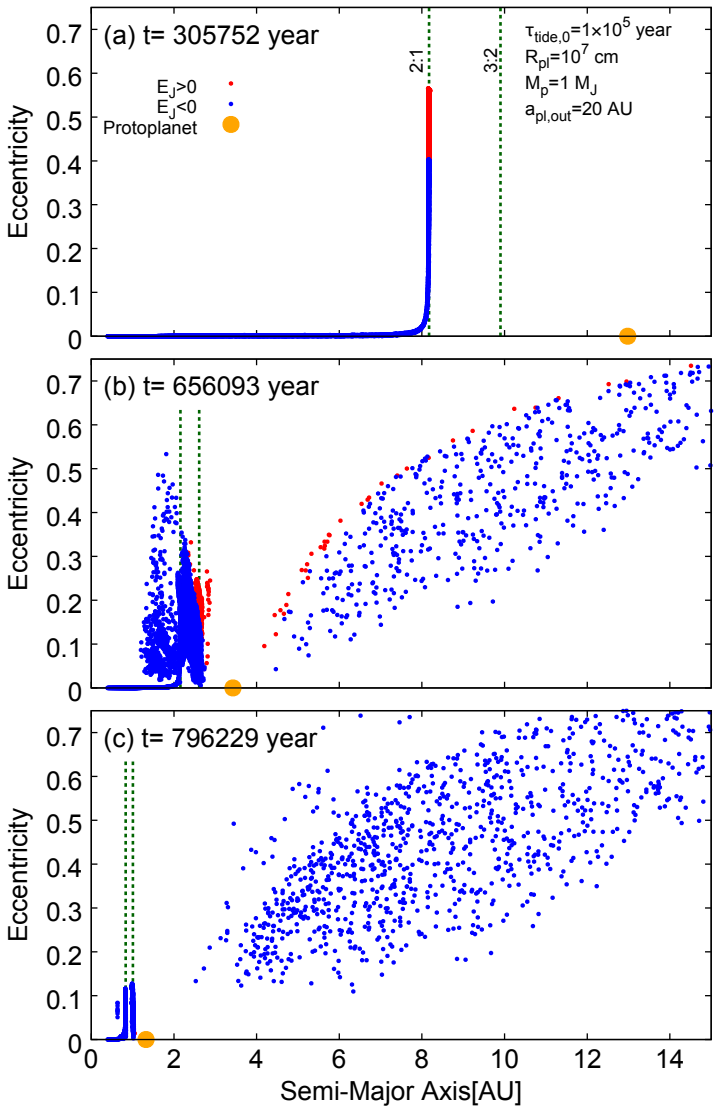

Figure 3.1: Snapshots of the orbital evolution of planetesimals for (a) t = 305,752 yr, (b) 656,093 yr, and (c) 796,229 yr in the reference case (see Table 3.1 for the setting). The horizontal and vertical axes are the semi-major axis and eccentricity, respectively. The red and blue circles indicate the planetesimals with positive and negative values of the Jacobi energy, respectively; the orange circle represents the migrating planet. The green dotted lines indicate the positions of 2:1 and 3:2 mean motion resonances with the planet.

Tanaka & Ida (1999) in the context of terrestrial planet formation.

Figure 3.2 shows the temporal change in the cumulative mass of captured planetesimals. The semi-major axis of the migrating planet is shown in the top x-axis. We find that most of the accreted planetesimals are captured mainly in the period between 4×10^5 and 7×10^5 years, when the planet migrates from ~ 9 to ~ 3 AU; hereafter, we call such a region the *the sweet spot*. As shown in Fig. 3.1, the resonant shepherding and the aerodynamic shepherding work effectively for $t \lesssim 4 \times 10^5$ yrs($a_p \gtrsim 9$AU) and $t \gtrsim 6 \times 10^5$ yrs($a_p \lesssim 3$AU), respectively. Most of the planetesimals are captured when both shepherding pro-

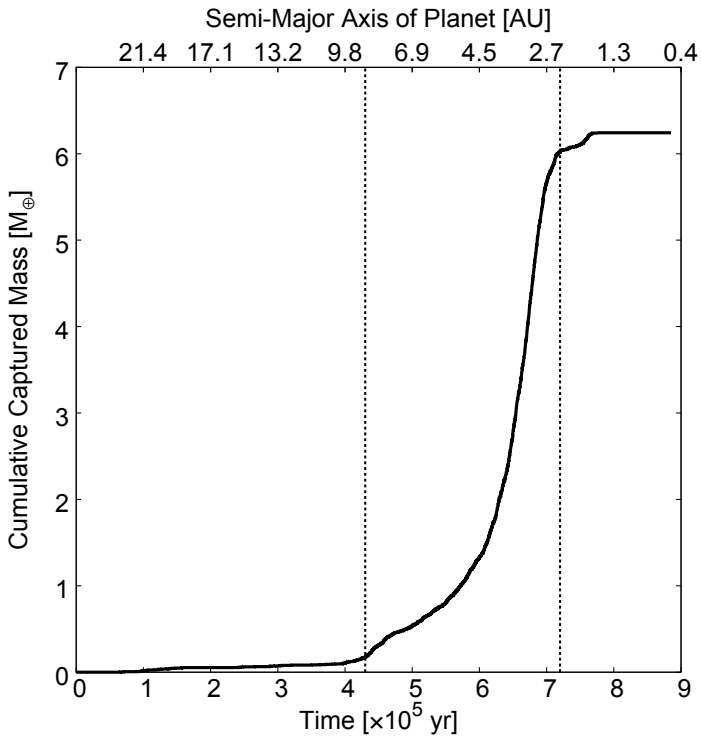

Figure 3.2: The temporal change in the cumulative mass of captured planetesimals in the reference case (see Table 3.1 for the setting). Top x-axis shows the semi-major axis of the migrating planet.

cesses are inefficient. This result demonstrates that the resonant shepherding and the aerodynamic shepherding inhibit planetesimal capture by a migrating giant planet. The cumulative captured mass at the end of the calculation (hereafter, the total captured mass $M_{\rm cap,tot}$) is found to be $\sim 6\ M_\oplus$, which corresponds to $\sim 14\%$ of the total mass of the available planetesimals ($\sim 43\ M_\oplus$ of planetesimals were distributed at the beginning of the simulation).

3.3.2 Role of accretion band

Here, we focus on the orbital evolution of each planetesimals. Figure 3.3 show the orbital evolution of a single planetesimal initially located (a) at 18.0AU (between the $3:2$ and $2:1$ mean motion resonances) and (b) 12.2AU (inner than $2:1$ mean motion resonance), respectively. In the reference case, $3:2$ and $2:1$ mean motion resonances are initially located around 20.1AU and 16.6AU, respectively.

In the case of panel (a), the planetesimal is first trapped by the $3:2$ mean motion resonance. After trapped in the resonance, the convergence in the orbits is halted and the eccentricity starts to increase with the planetary migration. As the planet migrates inward, the aerodynamic gas drag from the disk gas becomes stronger because the planetesimal is shepherded into the inner disk and the eccentricity is excited higher value. Both effects make the aerodynamic gas drag strong (Adachi et al. 1976, see also eq. (3.24)). Around $t \sim 4 \times 10^5$yr, the eccentricity reaches equilibrium value. Under the equilibrium condition,

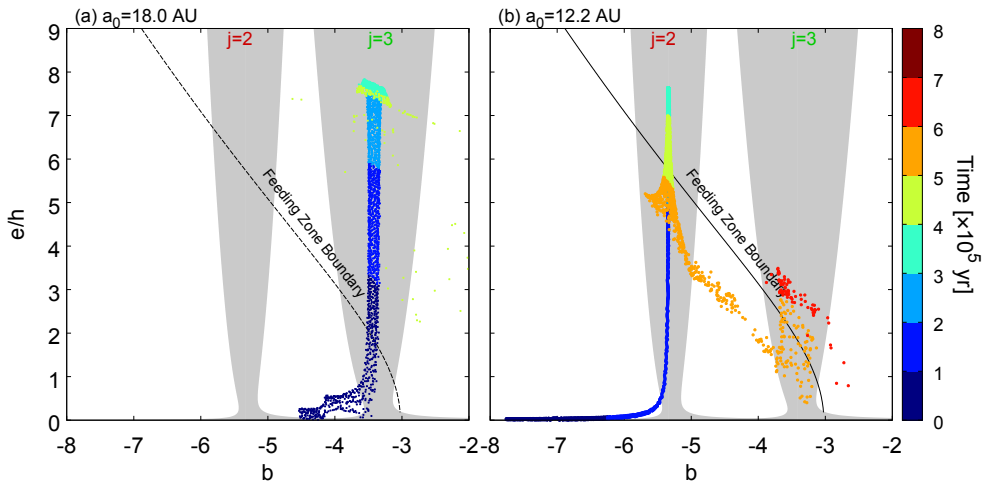

Figure 3.3: Orbital evolution of a single planetesimal initially located at (a) 18.0AU and (b) 12.2AU on $\tilde{b}$-$\tilde{e}$ plane. Gray areas show the $2:1$ and $3:2$ mean motion resonances. The dashed black line shows the boundary of the feeding zone. The color-coding of dots is done according to the simulation time.

the planetesimal orbit becomes unstable due to the overstable libration. As a result of the overstable libration, the planetesimal escapes from the resonance. Being trapped in the resonance, the resonant argument converges to ~ 0 and the conjunction point is aligned with the perihelion of the planet, which prevents close encounters between the trapped planetesimals and the planet.

In the case of panel (b), the planetesimal is first trapped by the $2:1$ mean motion resonance. In contrast to the case of panel (a), the planetesimal once enters the feeding zone, but then gets out of the feeding zone through the 2:1 mean motion resonance before escaping the resonant trapping. This is because the transport of the resonantly-trapped planetesimal to inner high-density region leads to a lowering of the equilibrium eccentricity. After escaping from the 2:1 resonance, the planetesimal undergoes other resonant trappings. We find that the planetesimal escaping from the 2:1 resonance is trapped in the 3:2 resonance. After staying in the 3:2 resonance for a while, the planetesimal ends up entering the feeding zone. Because of the same reason as the 3:2 resonant trapping, the planetesimal never enters the Hill sphere during being trapped in the $2:1$ resonant trapping.

Almost all other planetesimals obey the similar orbital evolution during the planetary migration phase, because $2:1$ and $3:2$ mean motion resonances sweep the planetesimal disk. The way for planetesimals to enter the feeding zone is limited to the regions where the mean motion resonances cross the feeding zone boundary. Hereafter, we call the regions as *accretion bands*. In the reference case, there are two accretion bands, $2:1$ mean motion resonance and $3:2$ mean motion resonance.

From the result in the reference case, we find that: (i) planetesimals enter the feeding zone through the accretion bands, (ii) to be captured by the planet, planetesimals have to escape from the resonant trapping. In the following sections, we derive the conditions required for planetesimal accretion analytically

based on these findings.

3.3.3 Analytical expressions for sweet spot

As shown above, mean motion resonances play important roles in the accretion of planetesimals onto a migrating planet. Hereafter, we focus on the 1st-order inner resonances with the migrating planet (or $j:(j-1)$ resonances). Trapped planetesimals suffer from resonant perturbation and aerodynamic gas drag. The Lagrange's equation of motion under the aerodynamic gas drag is given as

$$\dot{a} = 2(j-1)C_{\rm r} ae \sin\varphi - \frac{a}{\tau_{{\rm damp},a}}, \tag{3.21}$$

$$\dot{e} = -C_{\rm r}\sin\varphi - \frac{e}{\tau_{{\rm damp},e}}, \tag{3.22}$$

where $\tau_{{\rm damp},a}$ and $\tau_{{\rm damp},e}$ are the aerodynamic damping timescales for semi-major axis and eccentricity, which are given as (Adachi et al. 1976)

$$\tau_{{\rm damp},a} = \frac{\tau_{{\rm damp},0}}{2}\left\{(0.97e+0.64i+|\eta_{\rm gas}|)\eta_{\rm gas}\right\}^{-1}, \tag{3.23}$$

$$\tau_{{\rm damp},e} = \tau_{{\rm damp},0}\left(0.77e+0.64i+1.5|\eta_{\rm gas}|\right)^{-1}, \tag{3.24}$$

where

$$\tau_{{\rm damp},0} = \frac{2m_{\rm pl}}{C_{\rm d}\pi {R_{\rm pl}}^2 \rho_{\rm gas} v_{\rm K}}. \tag{3.25}$$

Note that we neglect the high order terms in eccentricity here; however, the eccentricity of the trapped planetesimals is easily excited to $e^2 \sim 0.1$. Even for this approximation, the analysis of the sweet spot shown below reproduces the numerical results well.

3.3.3.1 Orbital evolution under resonant trapping

Hereafter, we consider the case where the resonant trapping occurs. The period ratio between the planet and trapped planetesimal is kept to be

$$\frac{j-1}{j} = \frac{n_{\rm p}}{n} = \left(\frac{a}{a_{\rm p}}\right)^{3/2} = {\rm const.}, \tag{3.26}$$

where $n_{\rm p}$ is the mean motion of the planet. Taking a time derivative of eq. (3.26), we find

$$\frac{a}{\dot{a}} = \frac{a_{\rm p}}{\dot{a}_{\rm p}} = -\tau_{{\rm tide},a}. \tag{3.27}$$

Using eqs. (3.21), (3.22), (3.27) and $\tau_{{\rm damp},a} \gg \tau_{{\rm tide},a}$, we obtain

$$\dot{e} = \frac{1}{2(j-1)e\tau_{{\rm tide},a}} - \frac{e}{\tau_{{\rm damp},e}}, \tag{3.28}$$

$$\sin\varphi = -\frac{1}{2(j-1)C_{\rm r} e\tau_{{\rm tide},a}}. \tag{3.29}$$

Just after trapped into the resonances, e is small and $\dot{e}$ is positive. Equation (3.28) indicates that e increases on a timescale $\sim e^2\ \tau_{\mathrm{tide},a}$ ($\ll \tau_{\mathrm{tide},a}$) and reaches an equilibrium value. Solving eqs. (3.28) and (3.29) with $\dot{e}=0$, we obtain the equilibrium eccentricity and resonant argument as

$$e_{\mathrm{eq}} = \left\{ \frac{1}{2(j-1)} \frac{\tau_{\mathrm{damp},e}}{\tau_{\mathrm{tide},a}} \right\}^{1/2}, \tag{3.30}$$

$$\sin\varphi_{\mathrm{eq}} = -\frac{e_{\mathrm{eq}}}{C_{\mathrm{r}}\tau_{\mathrm{damp},e}}. \tag{3.31}$$

In contrast to the eccentricity, the inclination of the planetesimals are not excited by the migration planet because the planetesimals are far from the planet. When $e \gg i$ and $e \gg \eta_{\mathrm{gas}}$, both are written approximately as

$$e_{\mathrm{eq}} \sim \left\{ \frac{1}{1.54(j-1)} \frac{\tau_{\mathrm{damp},0}}{\tau_{\mathrm{tide},a}} \right\}^{1/3}, \tag{3.32}$$

$$\sin\varphi_{\mathrm{eq}} \sim -\frac{0.77{e_{\mathrm{eq}}}^2}{C_{\mathrm{r}}\tau_{\mathrm{damp},0}}. \tag{3.33}$$

In our simulation, since $\tau_{\mathrm{damp},0}/\tau_{\mathrm{tide},a}$ is assumed to $\propto a^{11/4}$, e_{eq} is higher at larger semi-major axes. Remember that we neglect the high order terms in eccentricity and the equilibrium eccentricity is smaller than that given in eq. (3.30) for $e \gtrsim 0.3$.

3.3.3.2 Condition for aerodynamic shepherding

The trapped planetesimals first undergo a rapid excitation of eccentricity and have their eccentricities gradually reduced after the equilibrium condition is reached. As shown in sec. 3.3.2, planetesimals flow into the feeding zone through the accretion bands. From the above analysis, the condition required for entering the feeding zone is that equilibrium eccentricity e_{eq} is larger than the eccentricity where the resonance centre crosses the feeding zone boundary e_{cross}. Substituting $E_{\mathrm{jacobi}}=0$ and $a/a_{\mathrm{p}} = (j-1/j)^{2/3}$ into eq. (2.39), e_{cross} is obtained as

$$e_{\mathrm{cross}} = \left[1 - \frac{1}{\cos^2 i} \left(\frac{j}{j-1} \right)^{2/3} \left\{ \frac{3}{2} + \frac{9}{2}h^2 - \frac{1}{2} \left(\frac{j}{j-1} \right)^{2/3} \right\}^2 \right]^{1/2}. \tag{3.34}$$

The required condition for trapped planetesimals to enter the feeding zone through the accretion bands is given

$$1.54(j-1){e_{\mathrm{cross}}}^3 < \frac{\tau_{\mathrm{damp},0}}{\tau_{\mathrm{tide},a}}. \tag{3.35}$$

The eccentricity of the crossing point e_{cross} is a function of $M_{\mathrm{p}}/M_{\mathrm{s}}$ and j, according to eq. (3.34). Figure 3.4 shows the relationship between e_{cross}/h and $M_{\mathrm{p}}/M_{\mathrm{s}}$ for different values of j. Note that as the planet mass increases, feeding zone expands and the point where the resonance centre crosses the feeding zone boundary disappears once the planetary mass exceeds a certain value. The accretion bands change with the planetary mass, e.g. there are three accretion bands $j=2,3,4$ when $M_{\mathrm{p}}/M_{\mathrm{s}} = 10^{-3.5}$, however there is only one accretion band $j=2$ when $M_{\mathrm{p}}/M_{\mathrm{s}} = 10^{-2.5}$.

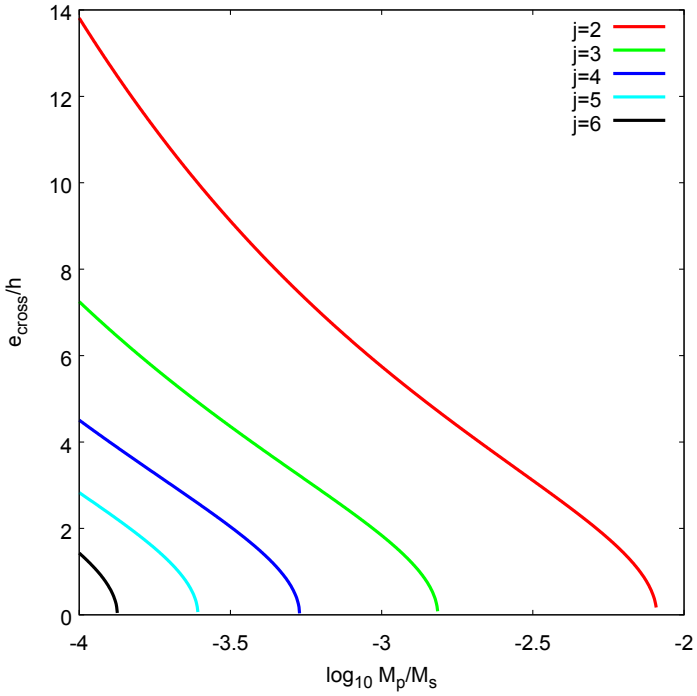

Figure 3.4: The dependence of the eccentricity of the crossing point $e_{\rm cross}$ on the mass ratio $M_{\rm p}/M_{\rm s}$. Solid lines show the cases of $j=2$ (red), $j=3$ (green), $j=4$ (blue), $j=5$ (skyblue) and $j=6$ (black), respectively.

3.3.3.3 Condition for resonant breaking

Planetesimals trapped in the mean motion resonances escape from the resonant trapping due to the aerodynamic force. Under the forces damping and enhancing planetesimal eccentricity, the orbit of the trapped planetesimal becomes unstable and starts to oscillate. Once the amplitude of oscillation exceeds the resonant width, resonant trapping is broken. This phenomena is called overstable libration and found by Goldreich & Schlichting (2014). They derived the condition required for instability to grow, which is given by

$$\tau_a < 0.30 \left\{ \frac{j^{3/2}}{(j-1)} \frac{M_{\rm p}}{M_{\rm s}} \right\}^{-2/3} \tau_e, \tag{3.36}$$

where τ_a and τ_e are timescales of change in semi-major axis and eccentricity.

Adapting this equation to our model, we use $\tau_a = \tau_{{\rm tide},a}$, $\tau_e = \tau_{{\rm damp},e}$. Substituting eqs. (3.24) and (3.30), we obtain the breaking condition for resonant trapping due to overstable libration as

$$3.29 \left(\frac{j}{j-1} \right)^{3/2} \frac{M_{\rm p}}{M_{\rm s}} < \frac{\tau_{\rm damp,0}}{\tau_{{\rm tide},a}}. \tag{3.37}$$

Even once this condition is achieved, it takes time $\sim \tau_{{\rm damp},e}$ for the instability to grow. If $\tau_{{\rm damp},e} > \tau_{{\rm tide},a}$, the trapped planetesimal is shepherded into the

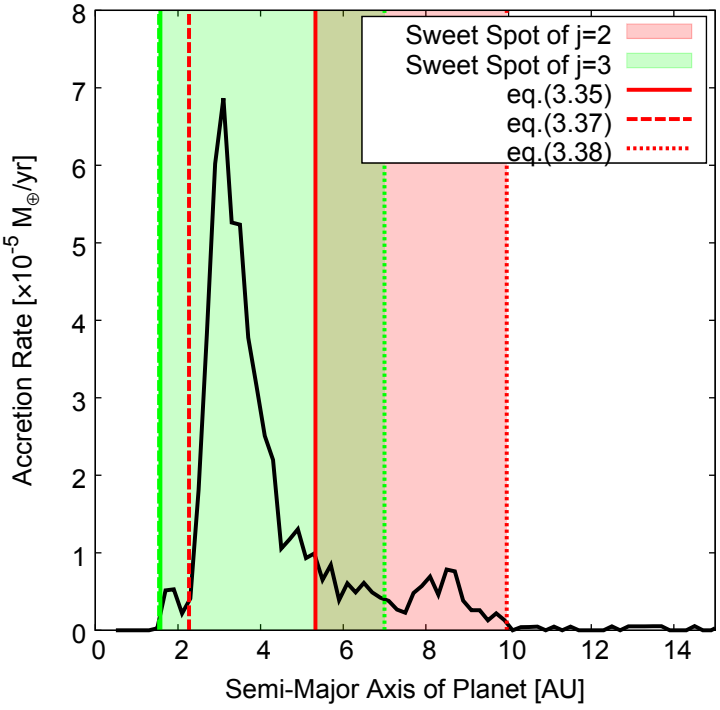

Figure 3.5: The accretion rate of planetesimals with the semi-major axis of the migrating planet. Vertical solid, dashed and dotted lines show the boundaries of the sweet spot written by eqs. (3.35), (3.37) and (3.38). The red lines are for the case of $j = 2$ and the green lines are for $j = 3$. The filled areas are called the sweet spots in this thesis.

inner disk region before escaping the resonance. The second condition required for overstable libration is $\tau_{\mathrm{damp},e} < \tau_{\mathrm{tide},a}$ and approximated into

$$\frac{\tau_{\mathrm{damp},0}}{\tau_{\mathrm{tide},a}} < 0.54(j-1)^{-1/2}. \tag{3.38}$$

3.3.3.4 Short summary and comparison with the numerical result

The location of the sweet spot is determined by the following two conditions,

$$1.54(j-1){e_{\mathrm{cross}}}^3 < \frac{\tau_{\mathrm{damp},0}}{\tau_{\mathrm{tide,a}}},$$

$$3.29\left(\frac{j}{j-1}\right)^{3/2}\frac{M_{\mathrm{p}}}{M_{\mathrm{s}}} < \frac{\tau_{\mathrm{damp},0}}{\tau_{\mathrm{tide,a}}} < 0.54(j-1)^{-1/2},$$

characterised by the ratio of the gas drag damping timescale $\tau_{\mathrm{damp},0}$ and the planetary migration timescale $\tau_{\mathrm{tide},a}$. These equations could apply to general cases where the disk model and planetary migration model are different from those in our model.

In the reference model, the timescale ratio is written as

$$\frac{\tau_{\rm damp,0}}{\tau_{{\rm tide},a}} = \left|\frac{\tau_{\rm damp,0}}{\tau_{{\rm tide},a}}\right|_{\rm 1AU} \left(\frac{j-1}{j}\right)^{1/3} a^{11/4}, \tag{3.39}$$

$$= \left|\frac{\tau_{\rm damp,0}}{\tau_{{\rm tide},a}}\right|_{\rm 1AU} \left(\frac{j-1}{j}\right)^{13/6} {a_{\rm p}}^{11/4}, \tag{3.40}$$

where

$$\left|\frac{\tau_{\rm damp,0}}{\tau_{{\rm tide},a}}\right|_{\rm 1AU} = 4.2\times10^{-3} \left(\frac{R_{\rm pl}}{10^7\ {\rm cm}}\right) \left(\frac{\tau_{\rm tide,0}}{10^5\ {\rm yr}}\right)^{-1}. \tag{3.41}$$

Figure 3.5 shows the accretion rate of planetesimals in the reference model with the location of the sweet spot given by above equations. Equations (3.35), (3.37), (3.38) and (3.40) give the location of the sweet spot 5 AU $\lesssim a_{\rm p} \lesssim$ 10 AU for $j=2$ and 1 AU $\lesssim a_{\rm p} \lesssim$ 7 AU for $j=3$, which covers the area where the accretion rate takes high values as $\gtrsim 10^{-5}\ M_\oplus$/yr. We conclude that the above equations reproduce the numerical results in the reference model well.

3.3.4 Dependence on the initial semi-major axis

Figure 3.6 shows the fraction of captured planetesimals as a function of their source semi-major axis a_0. Note that the sweet spots are also plotted, same as Fig. 3.5, but as a function of a instead of $a_{\rm p}$. From a physical point of view, the histogram can be divided into three regions including (1) $a_0 <$ 5 AU, (2) 5 AU $< a_0 <$ 15 AU, (3) 15 AU $< a_0 <$ 20 AU. In the first region, where the sweet spots for $j=2$ and $j=3$ cover, the capture fraction is quite small. This is because planetesimals initially located in the first region are shepherded by the resonance to the region inner than the sweet spot before escaping the resonant trapping. Those from the second region are first trapped in the 2:1 mean motion resonance and, then, about 20-40 % of them are captured by the planet. The planetesimals from the third region are trapped in 3:2 mean motion resonance and, then, less than 10 % of them are captured by the migrating planet.

The difference in capture probability between the second and third regions arises from the difference of the mean motion resonances by which planetesimals are first trapped. As a result, the dynamical configuration of planetesimals inside the feeding zone is changed. The main difference is the planetesimals eccentricity when the resonant trapping is broken; the eccentricity of planetesimals from the third region $\tilde{e} \sim 7$ is higher than that of planetesimals from the second region $\tilde{e} \sim 3$ as shown in Fig. 3.3. Since the capture probability decreases with increasing eccentricity (Ida & Nakazawa 1989), the capture probability for the third region is smaller than that for the second one.

From the results shown in Fig. 3.5 and Fig. 3.6, we conclude that planetesimals initially located outer than the sweet spots are shepherded by the mean motion resonances into the sweet spots and up to $\sim$ 40% of shepherded planetesimals are captured by the planet.

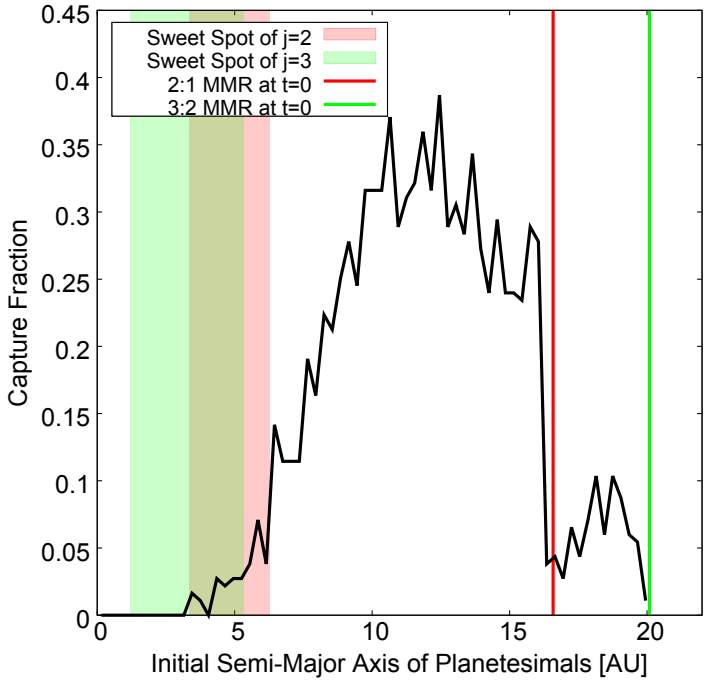

Figure 3.6: Fraction of planetesimals captured by the planet versus their source semi-major axis for the reference case. Red and green filled area show the sweet spots for $j = 2$ and $j = 3$. The red and green vertical solid lines are initial positions of $j = 2$ and $j = 3$ 1st-order mean motion resonances. The distribution of capture fraction is divided into the three regions, where inside the sweet spot, The bin width of the histogram is 0.3 AU.

3.4 Results of parameter studies

3.4.1 Parameter study of planetesimal accretion

As shown in the reference model, the accretion of planetesimals onto a migrating planet occurs in the sweet spot and the location of the sweet spot depends on the ratio of timescales $\tau_{\rm damp,0}$ to $\tau_{{\rm tide},a}$. In this section, we perform a parameter study where we change the planet's migration timescale $\tau_{\rm tide,0}$ (see eq. (3.5)), the radius of planetesimals $R_{\rm pl}$, the size of the planetesimal disk $a_{\rm pl,out}$ (or the initial position of the planet $a_{\rm p,0}$) and planet's mass $M_{\rm p}$, in order to investigate the effects of these parameters on the shepherding processes and the capture processes of planetesimals.

3.4.2 Dependence on planetesimal radius

First, we perform a parameter study for the size of planetesimals. The damping timescale $\tau_{\rm damp,0}$ increases with the size of planetesimals, so the location of the sweet spot is closer to the central star for larger planetesimals. We change the size of planetesimals from 10^5 cm to 10^8 cm (or $\sim 0.01 M_\oplus$). The assumption that mutual gravitational interaction of planetesimals is negligible is not correct for large planetesimals of $R_{\rm pl} \sim 10^8$ cm. This wide parameter range, nevertheless, is

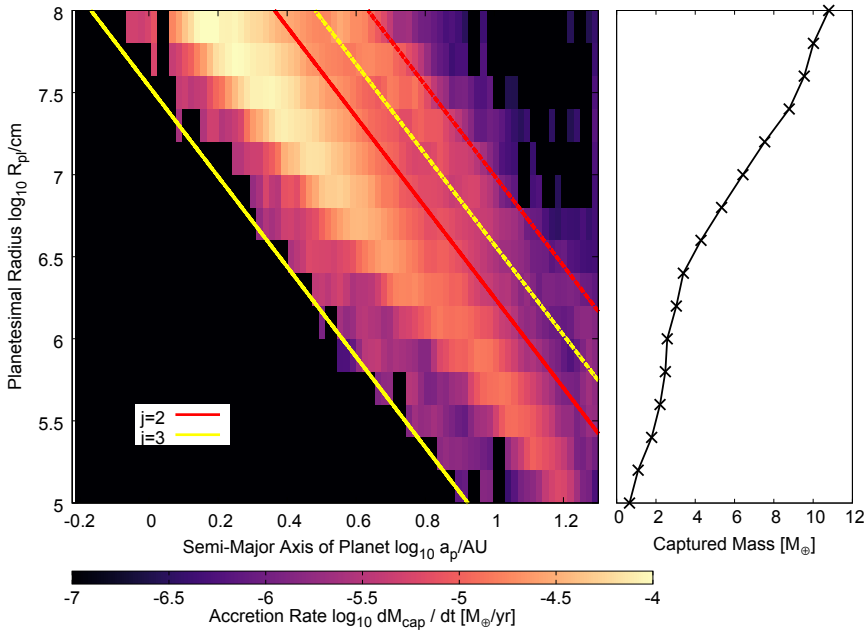

Figure 3.7: The results of the parameter study regarding the size of planetesimals $R_{\rm pl}$. In the left panel, the accretion rate of planetesimals are shown as a color contour on a plane of the semi-major axis of the migrating planet and the planetesimal radius. The inner and outer boundaries of the sweet spot are shown with solid and dashed lines. Red lines are for $j = 2$ and yellow lines are for $j = 3$. In the right panel, the total mass of captured planetesimals is plotted as a function of the planetesimal radius.

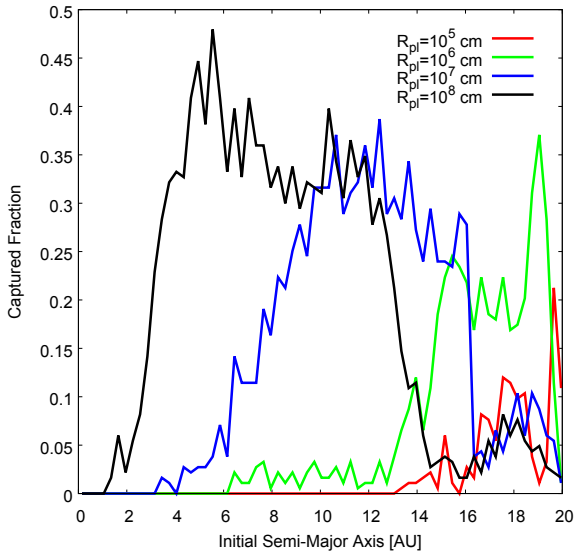

Figure 3.8: Same as fig. 3.6, but for the results of parameter study in the size of planetesimals $R_{\rm pl}$.

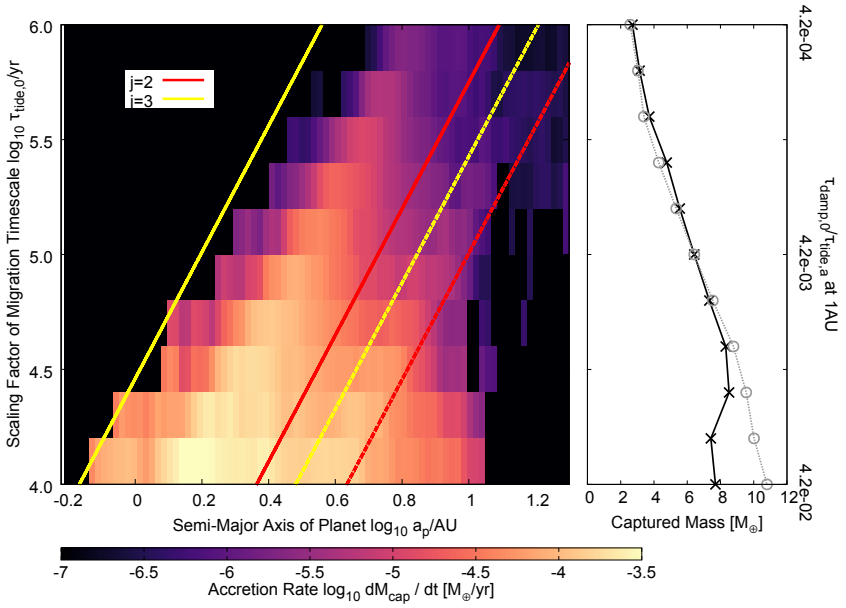

Figure 3.9: Same as Fig. 3.7, but for the results of the parameter study regarding the migration timescale $\tau_{\rm tide,0}$.

useful to deepen a physical understanding of the effect of the damping timescale on planetesimal accretion.

Figure 3.7 shows the results of the parameter study regarding the size of planetesimals $R_{\rm pl}$. In the left panel, the accretion rate of planetesimals is shown as a color contour on a plane of the semi-major axis of the migrating planet and the planetesimal radius. The inner and outer boundaries of the sweet spot derived in sec. 3.3.3 are shown with solid and dashed lines. Red lines are for $j = 2$ and yellow lines are for $j = 3$. In the right panel, the total mass of captured planetesimals are plotted as a function of the planetesimal radius.

The location of the sweet spot is found to be well reproduced by the analytical expressions derived in sec. 3.3.3. The maximum accretion rate and the total captured amount of planetesimals take higher values for larger planetesimals. This is because as the sweet spot moves inward, the amount of planetesimals shepherded into the sweet spot increases. More planetesimals are shepherded into the sweet spot in the case of larger planetesimals, where the sweet spot locates farther from the initial planet location (or closer to the central star). Figure 3.8 is the same as Fig. 3.6, but for the cases of $R_{\rm pl} = 10^5$ cm (red), $R_{\rm pl} = 10^6$ cm (green), $R_{\rm pl} = 10^7$ cm (blue) and $R_{\rm pl} = 10^8$ cm (black). The region where the capture fraction takes high values ~ 0.3 shifts with the sweet spot. From the above results, we conclude that the amount of captured planetesimals increases with the amount of planetesimals shepherded by the migrating planet before the planet reaches the sweet spot.

3.4.3 Dependence on migration timescale

Next, we perform a parameter study for the planetary migration timescale. The location of the sweet spot would be closer to the central star for faster planetary migration. We change the scaling factor of migration timescale $\tau_{\rm tide,0}$ from 10^4 yr

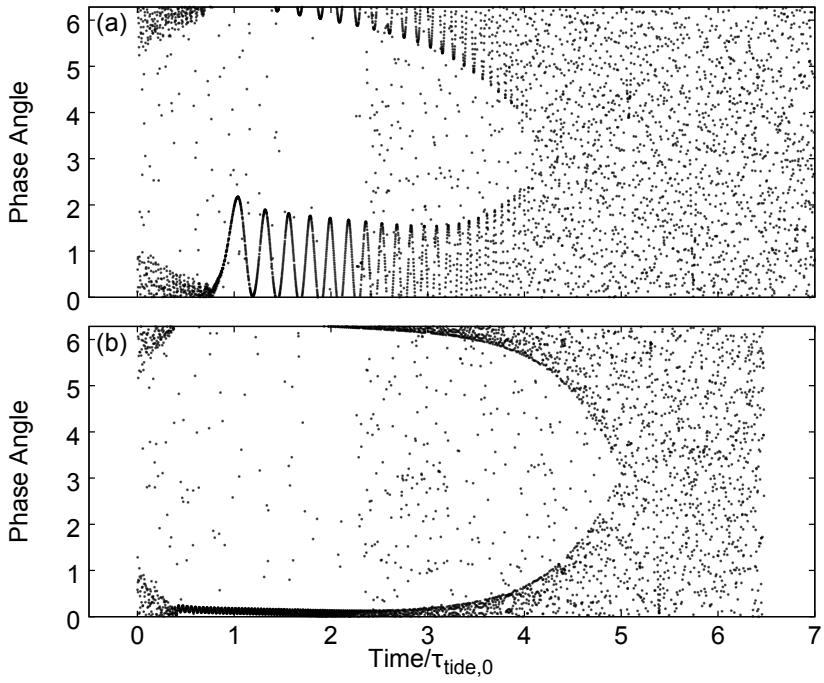

Figure 3.10: The change in the phase angle of a planetesimals initially located at $a_0 = 13.8$ AU. Panel (a) shows the case of $\tau_{\rm tide,0} = 10^4$ yr and panel (b) shows the case of $\tau_{\rm tide,0} = 10^5$ yr.

to 10^6 yr.

Figure 3.9 shows the results of the parameter study regarding $\tau_{\rm tide,0}$. The sweet spot is found to locate closer to the central star for faster planetary migration, or smaller $\tau_{\rm tide,0}$. The total amount of captured planetesimals also increases with decreasing $\tau_{\rm tide,0}$. In the right panel, the results of parameter study in $R_{\rm pl}$ are also plotted with grey circles. The right axis shows the ratio of the timescales at 1AU. Except for the cases of $\tau_{\rm tide,0} \lesssim 10^{4.6}$yr, the results of the parameter study in $\tau_{\rm tide,0}$ are almost same as the results of the parameter study in $R_{\rm pl}$, because the ratio of the timescales $\tau_{\rm damp,0}$ and $\tau_{\rm tide,a}$ takes the same value.

The results, however, differ in the cases of fast planetary migration $\tau_{\rm tide,0} \lesssim 10^{4.6}$ yr. This is because the planetary migration is too fast for mean motion resonances to stably trap the planetesimals. As discussed in sec. 2.2, the condition required for resonant trapping is that the timescale for planetesimals to across mean motion resonances is longer than the libration timescale. As shown in Fig. 2.2, stable resonant trapping is difficult for fast planetary migration as $\tau_{\rm tide,0} \sim 10^4$ yr.

In this case, the planetesimals are barely trapped into the resonances, but the resonant trapping is unstable due to the fast planetary migration. Figure 3.10 shows the changes in the phase angle of planetesimals initially located at $a_0 = 13.8$ AU in the cases of (a) $\tau_{\rm tide,0} = 10^4$ yr and (b) $\tau_{\rm tide,0} = 10^5$ yr. In panel (a), phase angle continues libration after trapped into the resonance. Fast planetary migration perturbs the orbits of trapped planetesimals and accelerates the overstable libration. The resonant trapping is broken earlier in the case of

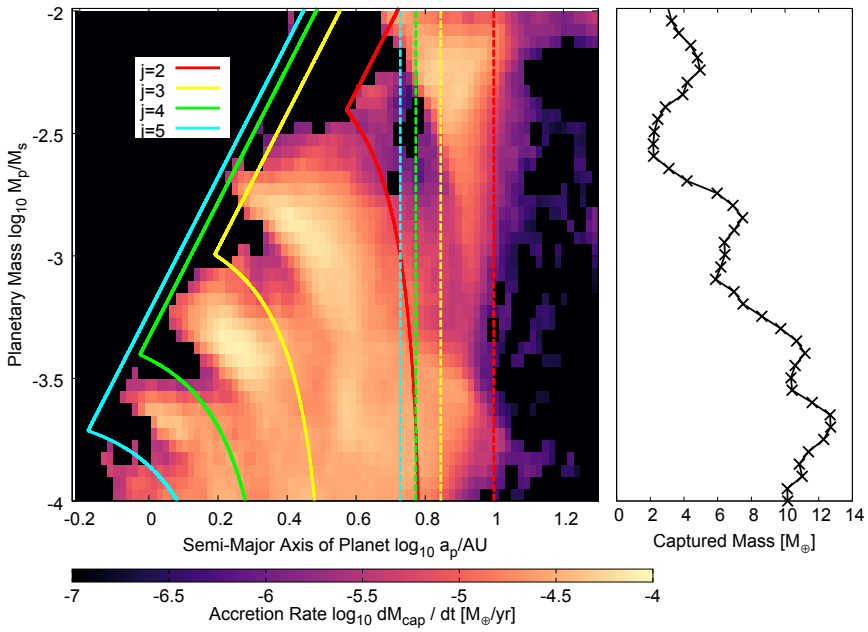

Figure 3.11: Same as Fig. 3.7, but for the results of the parameter study regarding planetary mass $M_{\rm p}$.

$\tau_{\rm tide,0} = 10^4$ yr than in the case of $\tau_{\rm tide,0} = 10^5$ yr, which results in the expansion of the sweet spot outward. The outer edge of the sweet spot expands, however, the total mass of captured planetesimals does not increase with decreasing $\tau_{\rm tide,0}$ for $\tau_{\rm tide,0} \lesssim 10^{4.6}$ yr. This is because fast planetary migration breaks the resonant trapping as soon as the trapped planetesimal reaches the equilibrium condition. The planetesimal in panel (a) escapes from the resonant trapping with $e \sim 0.7$ and that in panel (b) with $e \sim 0.4$. The difference in the eccentricities makes the difference of the capture probability, thus the total mass of captured planetesimals does not increase with the expansion of the sweet spot in the cases of $\tau_{\rm tide,0} \lesssim 10^{4.6}$ yr.

3.4.4 Dependence on planetary mass

Next, we perform a parameter study for the mass of migrating planet. The location of the sweet spot depends on the planetary mass. We change the planetary mass $M_{\rm p}/M_{\rm s}$ from 10^{-4} to 10^{-2}.

Figure 3.11 shows the results of the parameter study regarding $M_{\rm p}$. As shown in the right panel, the total mass of captured planetesimals changes with the planetary mass in a non-monotonic manner and takes local maxima at $M_{\rm p}/M_{\rm s} \sim 10^{-3.6}$, $10^{-3.3}$, $10^{-2.7}$ and $10^{-2.2}$ local and minima at $10^{-3.5}$, $10^{-3.0}$ and $10^{-2.5}$. The global decreasing trend with increasing planetary mass comes from that the inner boundary of the sweet spot moves outward. The periodical change reflects the change in the sweet spot width, as shown in the left panel.

The periodical change of the total mass of captured planetesimals comes from the shift of the effective accretion bands. The feeding zone boundary expands with the planetary mass. The cross points between the resonances and the feeding zone boundary change with the planetary mass, and some of the cross

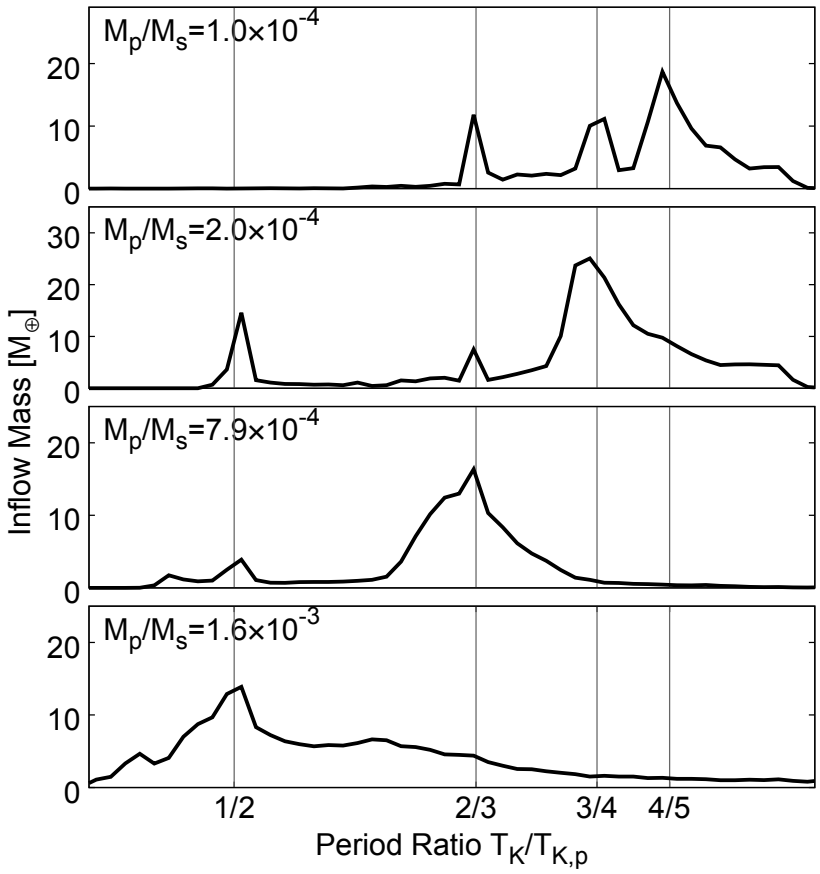

Figure 3.12: Total mass of planetesimals that enter the feeding zone as a function of their period ratio with the migrating planet at the time of entry. Each panels show the cases of $M_\mathrm{p}/M_\mathrm{s} = 1.0\times10^{-4}$, $M_\mathrm{p}/M_\mathrm{s} = 2.0\times10^{-4}$, $M_\mathrm{p}/M_\mathrm{s} = 7.9\times10^{-4}$ and $M_\mathrm{p}/M_\mathrm{s} = 1.6\times10^{-3}$, from top to bottom panels. The vertical solid lines show the resonance centre of $2:1$, $3:2$, $4:3$ and $5:4$ mean motion resonances, from left to right, respectively.

points disappear for larger planetary mass as shown in Fig. 3.4. Figure 3.12 shows the total mass of planetesimals that enter the feeding zone, or the total mass flow of planetesimals, as a function of their period ratio with the migrating planet at the time of entry. From top panel to bottom panel, planetary mass is $M_\mathrm{p}/M_\mathrm{s} = 1.0\times10^{-4}$, $M_\mathrm{p}/M_\mathrm{s} = 2.0\times10^{-4}$, $M_\mathrm{p}/M_\mathrm{s} = 7.9\times10^{-4}$ and $M_\mathrm{p}/M_\mathrm{s} = 1.6\times10^{-3}$, respectively. In the case of $M_\mathrm{p}/M_\mathrm{s} = 1.0\times10^{-4}$, effective accretion bands are $3:2$, $4:3$ and $5:4$ mean motion resonances. As the planetary mass increases, the effective accretion bands shift for those with smaller j. Accretion bands of $5:4$, $4:3$ and $3:2$ resonances are disappear in the case of $M_\mathrm{p}/M_\mathrm{s} = 1.6\times10^{-3}$.

3.4.5 Dependence on size of planetesimal disk

Finally, we perform a parameter study for the size of the planetesimal disk $a_\mathrm{pl,out}$. We change the size of planetesimal disk $a_\mathrm{pl,out}$ from 1 AU to 50 AU.

Figure 3.13 shows the total mass of captured planetesimals $M_\mathrm{cap,tot}$ as a function of $a_\mathrm{pl,out}$. When $a_\mathrm{pl,out} \lesssim 6$ AU, $M_\mathrm{cap,tot}$ decreases rapidly with the decreasing

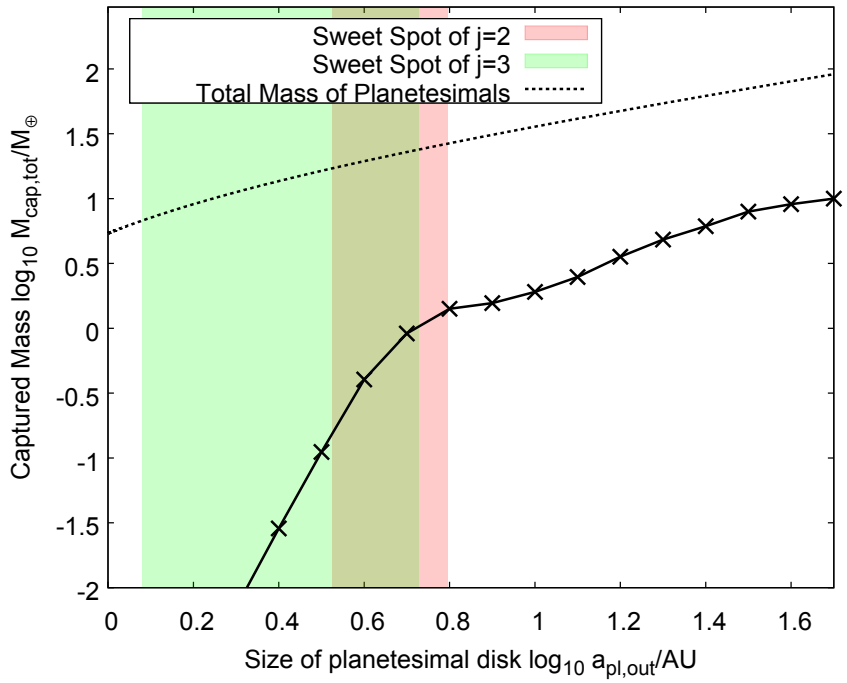

Figure 3.13: Total captured amount of planetesimals as a function of the planetesimals disk size $a_{\rm pl,out}$. The dashed line show the total disk mass. The red and green areas show the sweet spot of $j = 2$ and $j = 3$, respectively.

$a_{\rm pl,out}$. This is because there are no planetesimals which are shepherded into the sweet spot from the region outer than the sweet spot. On the other hand, when $a_{\rm pl,out} \gtrsim 6$ AU, $M_{\rm cap,tot}$ increases with the increasing $a_{\rm pl,out}$ almost linearly with the total mass of planetesimals used in the simulation. In this case, the mass of planetesimals shepherded into the sweet spot increases with $a_{\rm pl,out}$. The capture fraction of planetesimals initially located between the outer boundary of the sweet spot and $2:1$ mean motion resonance is almost constant as shown in Fig. 3.6, which results in the constant increase with the total mass of planetesimals.

3.5 Discussion

3.5.1 Location of sweet spot in evolving protoplanetary disk

The location of the sweet spot depends on the ratio of the two timescales, planetary migration and aerodynamic gas drag. Here we discuss the effect of disk structure on the timescale ratio.

In the classical picture of the Type II migration (e.g. Lin & Papaloizou 1993), the planet migrates with a deep gap opened by the planet itself. The radial gas flow is halted by the gap and the planet migrates with the accretion gas. Recent hydrodynamic simulations, however, revealed that the gap bottom is not so deep and the gas can cross the gap (Kanagawa et al. 2015, 2016, 2017). In this case, the planetary migration is not in the classical regime. Kanagawa et al. (2018) found that even if a gap is opened by the planet, the torque exerted onto the

planet is given by a similar expression to that for the Type I regime. The migration timescale in the new type II regime is written as

$$\tau_{\rm tide,a,II} \sim \frac{1}{2c}\left(\frac{M_{\rm p}}{M_{\rm s}}\right)^{-1}\left(\frac{{r_{\rm p}}^2\Sigma_{\rm gap}}{M_{\rm s}}\right)^{-1}\left(\frac{h_{\rm s}}{r_{\rm p}}\right)^2 {\Omega_{\rm K}}^{-1}, \tag{3.42}$$

where c is a constant estimated as $1-3$ and $\Sigma_{\rm gap}$ is the surface density of disk gas at the gap bottom. $\Sigma_{\rm gap}$ depends on the unperturbed surface density of disk gas $\Sigma_{\rm gas}$ and given from the hydrodynamic simulations of Kanagawa et al. (2017) as

$$\Sigma_{\rm gap} = \frac{\Sigma_{\rm gas}}{1+0.04K}, \tag{3.43}$$

with

$$K = \left(\frac{M_{\rm p}}{M_{\rm s}}\right)^2\left(\frac{h_{\rm s}}{r_{\rm p}}\right)^{-5}{\alpha_{\rm vis}}^{-1}, \tag{3.44}$$

where $\alpha_{\rm vis}$ is the alpha parameter for disk gas viscosity (Shakura & Sunyaev 1973). Assuming $0.04K \gg 1$, we obtain

$$\tau_{\rm tide,\mathit{a},II} \sim \frac{0.02}{c}{\alpha_{\rm vis}}^{-1}\left(\frac{{r_{\rm p}}^2\Sigma_{\rm gas}}{M_{\rm p}}\right)^{-1}\left(\frac{h_{\rm s}}{r_{\rm p}}\right)^{-3}{\Omega_{\rm K}}^{-1}, \tag{3.45}$$

$$\propto \Sigma_{\rm gas}(r_{\rm p})^{-1}\left(\frac{h_{\rm s}}{r_{\rm p}}\right)^{-3}. \tag{3.46}$$

The damping timescale of aerodynamic gas drag $\tau_{\rm damp,0}$ also depends on the disk structure (see eq. (3.25)) as

$$\tau_{\rm damp,0} = \frac{8\sqrt{2\pi}}{3C_{\rm d}}\frac{\rho_{\rm pl}R_{\rm pl}}{\Sigma_{\rm gas}}\frac{h_{\rm s}}{r_{\rm pl}}{\Omega_{\rm K}}^{-1}, \tag{3.47}$$

$$\propto \Sigma_{\rm gas}(r_{\rm pl})^{-1}\frac{h_{\rm s}}{r_{\rm pl}}. \tag{3.48}$$

Note that we assume that the planetesimals trapped in mean motion resonances are outside the gap. If the disk viscosity is small, however, the gap slope reaches the resonances and the damping timescale increases a few times. For simplicity, we neglect the effect.

From the above discussion, the ratio of the two timescales is given as

$$\frac{\tau_{\rm damp,0}}{\tau_{\rm tide,\mathit{a},II}} = 1.21\times10^{-6}C^{-1}\left(\frac{M_{\rm p}}{M_{\rm s}}\right)^{-1}\left(\frac{r_{\rm p}}{1{\rm AU}}\right)^{4-2\beta_{\rm disk}}\left(\frac{j}{j+1}\right)^{-2\gamma/3}, \tag{3.49}$$

with

$$C = \left(\frac{\alpha_{\rm vis}}{10^{-3}}\right)^{-1}\left(\frac{\rho_{\rm pl}}{2{\rm g/cm^3}}\right)^{-1}\left(\frac{R_{\rm pl}}{10^7\ {\rm cm}}\right)^{-1}\left(\frac{M_{\rm s}}{M_\odot}\right)\left(\frac{|h_{\rm s}/r|_{1{\rm AU}}}{0.03}\right)^4, \tag{3.50}$$

$$\gamma = -\alpha_{\rm disk} + \frac{\beta_{\rm disk}}{2} - \frac{1}{2}. \tag{3.51}$$

Equation (3.49) indicates that the surface gas density profile only weakly affects the ratio of timescales, which is found to depend not explicitly on $\Sigma_{\rm gas}$ and weakly on $\alpha_{\rm disk}$, namely, $(j/j+1)^{2\alpha_{\rm disk}/3}$. This means that while a circumstellar disk evolves during the planetary formation stages, the timescale ratio hardly changes, which also means the location of the sweet spot is fixed during the planetary formation stage.

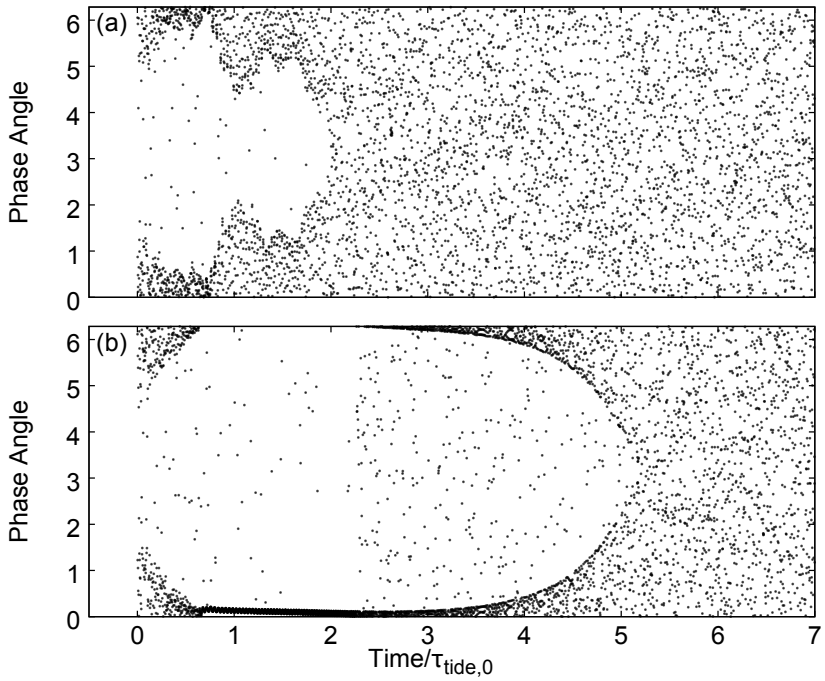

Figure 3.14: Same as Fig. 3.10, but (a) for the case with artificial perturbation given by eq. (3.52) and (b) without artificial perturbation.

3.5.2 Comparison with Tanaka & Ida (1999)

From our numerical calculation, we have found that mean motion resonances and resonant breaking play important roles in the accretion of planetesimals onto a migrating planet. Here, we compare our results with those in Tanaka & Ida (1999), where resonant traps are broken instantaneously by artificial perturbations. First, we add artificial perturbations in the same way as Tanaka & Ida (1999). We randomise the phase angle by adding displacements in orbital elements except a, e and i. The size of the displacement is set as

$$\Delta\theta = 2\pi f_{\rm p}, \tag{3.52}$$

where $f_{\rm p}$ is a scaling factor of perturbation strength and randomly given from -0.01 to 0.01. We add $\Delta\theta$ to Ω, ϖ and ψ every conjunction time. As shown in eq. (2.24), the resonant width is larger for Jupiter-mass planets than the Earth-mass planet considered in Tanaka & Ida (1999). Even under this strong perturbations (1 % displacement in phase angle every conjunction time), mean motion resonances with a Jupiter mass planet are effective in trapping planetesimals and resonance shepherding occurs. However, resonant trapping is weakened and overstable libration is accelerated. Figure 3.14 shows the temporal change in the phase angle in the case with artificial perturbation. Resonant trapping occurs in both cases but the time of resonant breaking is much earlier than that in the case without the perturbation.

Adding this artificial perturbation, we perform a parameter study regarding planetary mass $M_{\rm p}/M_{\rm s}$, same in sec. 3.4.4. Figure 3.15 shows the results of the parameter study with the strong artificial perturbations. In the right panel,

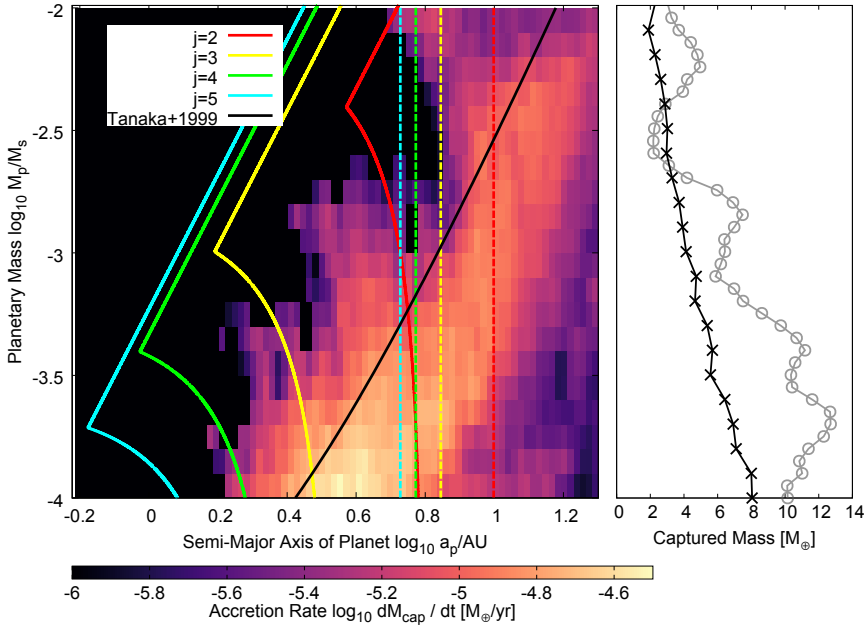

Figure 3.15: Same as Fig. 3.11, but for the results of a parameter study for planetary mass $M_{\rm p}$ with the artificial perturbations (see Eq. (3.52)).

the results with (cross) and without (open circle) artificial perturbations are plotted. Due to the artificial perturbations, the sweet spot shifts outward and the total mass of captured planetesimals is reduced. The black solid line shows the condition of shepherding obtained in Tanaka & Ida (1999) (see eq. (2.47)). This equation shows the inner boundary of the sweet spot in the case where resonant traps are perfectly broken. Comparing the results with and without artificial perturbations, although it might sound opposite to intuition, we conclude that resonant trapping leads to shifting the sweet spot inward and enhancing the accretion of planetesimals due to the effect of accretion bands.

3.5.3 Model limitation

Here, we discuss the assumptions used in our model. We assume that all solid materials are in the form of the planetesimals and the formation of embryos or other protoplanets are neglected. In addition, planetesimals are treated as test particles in our model. This manipulation neglects collision between planetesimals and gravitational force of planetesimals on a migrating planet. Here, we discuss these effects.

In our simulation, we considered the single planet migration, however, when a gas giant planet starts to migrate, many other planets may exist within the orbit of the gas giant in the same system. If the relative radial distance between the gas giant planet and other planets decreases due to their different migration timescales (converging process), the planets ahead of the gas giant planet could add the gravitational perturbation upon planetesimals trapped in mean motion resonances, which would amplify the libration of their orbits, thereby breaking the resonant shepherding process as same as the artificial perturbations added in sec. 3.5.2. Thus, in the converging processes, the existence of other planets

is expected to reduce the efficiency of capture of planetesimals by the migrating giant planet. On the other hand, if the relative radial distance increases (diverging process), planetesimals would be swept up by those planets, reducing the amount of planetesimals captured by the gas giant planet. These effects should be investigated in future research.

The collision between planetesimals is divided into two cases. First one is the collision between a planetesimal trapped in the resonance and a planetesimal located outside the resonances. The eccentricity of trapped planetesimals is so high as ~ 0.1 and collision velocity becomes so fast as $\sim e\, v_{\rm K}$. High velocity collision largely changes the energy and angular momentum of collided planetesimal, which results in the change in semi-major axis and, in some cases, the trapped planetesimal is pushed out the resonant width. Thus, collision between planetesimals might break resonant trapping and reduce the accretion rate of planetesimals as shown in sec. 3.5.2. This effect would be more important for inner disk, where sweet spot locates, because number density of planetesimals is higher in inner disk. We will investigate the effect of high velocity collision on resonant trapping and planetesimal accretion in chap. 4.

Second one is the collision between planetesimals trapped in a resonance. Inside the resonance, phase angle is aligned with $\varphi \sim 0$ and relative velocity between trapped planetesimals is too small to break resonant trapping. In this case, collisions result in the growth of planetesimals. During the planetary migration outer than sweet spot (or before overstable libration occurs), many planetesimals are shepherded by the inner most resonance, like $2:1$ mean motion resonances for Jupiter-mass planet. The surface density of planetesimals inside the resonance becomes ten-times or more higher than that outside the resonance. So the growth of planetesimals due to the mutual collision occurs and some embryos might be formed inside the resonance. The embryo inside the resonance scatters surrounding planetesimals, which breaks resonant trapping. The efficiency of the resonant breaking by the embryo scattering would depends on the mass of the embryo. Thus, the growth rate of the embryo inside the resonance is important. The growth of planetesimals inside the resonance should be investigated by the full N-body simulation because the effect of resonant trapping, which align the orbit of trapped planetesimals, must be correctly included. This problem is one of our future studies.

When many planetesimals are shepherded by the planet, the gravitational back reaction from the shepherded planetesimals slows down the migration speed of the planet. Given total mass of shepherded planetesimals as $M_{\rm tot,sh}$, the migration speed becomes $(M_{\rm p}+M_{\rm tot,sh})/M_{\rm p}$ times slower. For Jupiter mass planet, the back reaction can be negligible because $M_{\rm tot,sh} \sim 10 M_\oplus$ in the reference case, but for Neptune mass planet. The slowing down of the planetary migration results in the shift of the sweet spot and reduction in the total captured amount of planetesimals as shown in sec. 3.4.3. Thus, the back reaction of shepherded planetesimals would weaken the dependence of sweet spot on the planetary mass for Neptune mass planet.

3.6 Summary of Chapter3

Planetesimal accretion during the formation of gas giant planets is a source of the heavy elements in the interior of gas giant planets. In this chapter, we have investigated the planetesimal accretion onto a migrating proto-gas giant planet. We focused on the effect of mean motion resonances which was expected to play important roles in planetesimal accretion. We have performed the direct orbital integration of planetesimals around a migrating proto-gas giant planet, taking into account the effects of mean motion resonances, and investigated the fundamental physics for planetesimal accretion during planetary migration. From the numerical results, we found the basic physics of planetesimal accretion as follows:

- There are two shepherding processes, resonant shepherding and aerodynamic shepherding, that act as barriers for planetesimal accreting onto a migrating gas giant planet.
- Planetesimal accretion occurs where both shepherding processes are ineffective, which we call "sweet spot" in this thesis.
- We analytically derived the required conditions for the effective planetesimal accretion, which show that the location of the sweet spot is determined by the ratio of damping timescale $\tau_{\mathrm{damp},0}$ and migration timescale $\tau\mathrm{tide}, a$.
- The total amount of planetesimals captured by the planet increases with the amount of planetesimals shepherded into the sweet spot during the planetary migration.
- The captured heavy-element mass increases with the migration length almost linearly.

We conclude that mean motion resonances play important roles in planetesimal accretion onto a migrating proto-gas giant planet. Comparing the results of Tanaka & Ida (1999), although it might sound opposite to intuition, we conclude that resonant trapping leads to shifting the sweet spot inward and enhancing the accretion of planetesimals due to the effect of accretion bands.

Chapter 4

Break of Resonant Trapping via High-Velocity Collisions between Planetesimals

4.1 Introduction

Mean motion resonances play important roles in planetesimal accretion as shown in chap. 3. Resonant trapping and break of resonant trapping control the timing of planetesimal accretion, or location of sweet spot, which also determines the total amount of captured planetesimals. In chap. 3, resonant trapping is broken by the overstable libration triggered by the aerodynamic gas drag. If the other effects break the resonant trapping more effectively than the overstable libration, the planetesimal accretion can be changed from the results in chap. 3.

The break of resonant trapping is triggered by the perturbation on the resonant arguments. The break of resonant trapping is well discussed in the planet-planet resonances found in exoplanetary systems. The formation of compact multi-planetary systems easily results in a formation of planet pairs trapped in mean motion resonances (Hands et al. 2014; Hands & Alexander 2016). These results are inconsistent with the distribution of period ratios in observed multi-planetary systems (Fabrycky et al. 2014). To break such planet-planet resonances, several mechanisms are proposed (Goldreich & Schlichting 2014; Hands & Alexander 2016, 2018; Pichierri & Morbidelli 2020). On the other hand, planet-planetesimal resonances can be broken by the other mechanisms. Aerodynamic gas drag exerts strong perturbation on trapped planetesimals. If the radial drift timescale is much shorter than the libration timescale, the trapped planetesimals can escape from the resonant trapping (Malhotra 1993b; Kary et al. 1993; Kary & Lissauer 1995). Even for large planetesimals as $\sim 100\mathrm{km}$, eccentricities of trapped planetesimals are highly excited and strong aerodynamic damping in eccentricity triggers overstable libration (Goldreich & Schlichting 2014) as shown in the cases of planetary migration in chap. 3. Aerodynamic gas drag enhances the libration amplitude in the semi-major axis of trapped planetesimals. Once the amplified libration in the semi-major axis exceeds the width of the mean motion resonances, the resonant trapping is broken and the trapped planetesimals escape from the mean motion resonances. Even in the cases without aerodynamic gas drag, the break of resonant trapping occurs. Malhotra (1993b) investigated the break of resonant trapping by adding a velocity kick on the trapped planetesimals, which is mainly generated by the mutual collisions of

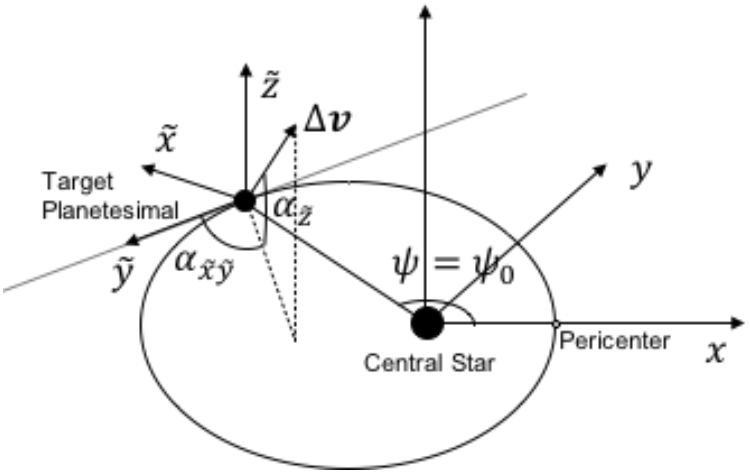

Figure 4.1: Geometrical picture of impact model.

planetesimals. They found that resonant trapping could be broken by the velocity kick when the displacement in the semi-major axis brought by the velocity kick exceeded the width of the mean motion resonances. The width of the mean motion resonances increases with the planetary mass (see eq. (2.24) and (2.25)) and the break of resonant trapping is more difficult for larger planets (Malhotra 1993b). Velocity kicks which are strong enough to break the resonant trapping, however, might be exerted on the trapped planetesimals in the planetary migration phase of proto-gas giant planets because the strength of the velocity kick depends on the relative velocity between planetesimals. The relative velocity between a planetesimal trapped in the resonance and a planetesimal outside the resonances is more than $\sim 10\%$ of Kepler velocity. Even for the massive planet as Jupiter, such a high-velocity collision has a possibility to break the resonant trapping and affect the planetesimal accretion in planetary migration phase.

In this chapter, we investigate the effect of resonant breaking on planetesimal accretion. In sec. 4.2, we derive the requirement for the break of resonant trapping, which is approximately obtained by Malhotra (1993b). We expand the parameter region and derive a new formula for the break of resonant trapping. Using the direct orbital integration, we investigate the break of resonant trapping via velocity kick and compare the derived formula with the numerical results in sec. 4.3. In sec. 4.4, we investigate the collision timescale of eccentric planetesimals. In sec. 4.5, to investigate the effect of breaking the resonant trapping on planetesimal accretion onto a migrating proto-gas giant planet, we include the effect of high-velocity collisions in the orbital evolution code used in chap. 3. In sec. 4.6, we discuss the validity of collision model and parameters used in our simulations. We summarise this chapter in sec. 4.7.

4.2 Condition for stable resonant trapping

Malhotra (1993a) derived an analytical formula for breaking the resonant trapping, however, their formula cannot reproduce the numerical results, especially when the velocity kick is perpendicular to the velocity vector of the trapped planetesimal. In this section, we derive a required condition for breaking the resonant trapping including the direction of velocity kick which is neglected in

Malhotra (1993a).

For the stable resonant trapping, perturbations exerting on the trapped planetesimals must be small enough that the libration in the resonant argument φ is small. The maximum libration amplitude $\sim 2\pi$ in resonant argument can be converted into the maximum libration in the semi-major axis, which is defined as resonant width and given by eqs. (2.24) and (2.25). The condition for stable resonant trapping can be written as

$$\left| \int_{t_0}^{t_0+T_{\rm lib}} \frac{\dot{a}_{\rm ptb}}{a} \mathrm{d}t \right| \lesssim \left| \frac{\Delta a_{\rm res}}{a} \right|, \tag{4.1}$$

where $\dot{a}_{\rm ptb}$ is a change in the semi-major axis due to the perturbation of the external forces. If the perturbation is discontinuous and the timescale of the perturbation is much shorter than the libration timescale, e.g. collision of planetesimals, the external force can be regarded as an impact force. In this case, the condition for stable resonant trapping is transformed into

$$\left| \frac{\Delta a_{\rm kick}}{a} \right| \lesssim \left| \frac{\Delta a_{\rm res}}{a} \right|, \tag{4.2}$$

where $\Delta a_{\rm kick}$ is a displacement of semi-major axis of the target planetesimal due to the impact.

We consider a high-velocity collision of an impact planetesimal on a target planetesimal trapped in the mean motion resonance. Due to the collision, the target planetesimal obtain kinetic energy and angular momentum from the impact planetesimal. The change in the velocity of the target planetesimal due to the planetesimal collision can be regarded as a velocity kick. In order to model the velocity kick, we parameterize the velocity kick using a scaling factor $f_{\rm imp}$ and angles of velocity kick $\alpha_{\tilde{x}\tilde{y}}$ and $\alpha_{\tilde{z}}$. The velocity kick $\Delta \mathbf{v}_{\rm kick}$ is given as

$$\Delta \mathbf{v}_{\rm kick} = f_{\rm imp} v_{\rm K} \mathbf{P}_{\tilde{z}}(\alpha_{\tilde{x}\tilde{y}}) \mathbf{P}_{\tilde{x}}(\alpha_{\tilde{z}}) \hat{\mathbf{v}}, \tag{4.3}$$

where $v_{\rm K}$ is the Kepler velocity of the target planetesimal and $\hat{\mathbf{v}}$ is the unit vector along the velocity vector of the target planetesimal. $\mathbf{P}_{\tilde{x}}(\alpha_{\tilde{z}})$ and $\mathbf{P}_{\tilde{z}}(\alpha_{\tilde{x}\tilde{y}})$ are rotation matrixes around $\tilde{x}$ and $\tilde{z}$ axis by the angle $\alpha_{\tilde{z}}$ and $\alpha_{\tilde{x}\tilde{y}}$, respectively. Here, $\tilde{x}, \tilde{y}, \tilde{z}$ are local coordinates where $\tilde{x}-\tilde{y}$ plane consistent with the orbital plane of the target planetesimal and the velocity vector of the target planetesimal consists with the $\tilde{y}$ axis. The geometrical picture of our model is shown in Fig. 4.1.

First, we consider the change in the kinetic energy and the semi-major axis of target planetesimal. Just before and after the impact, there are relations of

$$v_0{}^2 = GM_{\rm s} \left(\frac{2}{R_0} - \frac{1}{a_0} \right), \tag{4.4}$$

$$v_1{}^2 = GM_{\rm s} \left(\frac{2}{R_1} - \frac{1}{a_1} \right), \tag{4.5}$$

where R is the distance from the central star and subscripts of 0 and 1 indicate before and after giving velocity kick, respectively. On the time of the impact, $R_0 = R_1$ and the displacement in the semi-major axis $\Delta a_{\rm kick} = a_1 - a_0$ can be

written as

$$\frac{\Delta a_{\rm kick}}{a_0} = \frac{\mathscr{A}}{1-\mathscr{A}}, \tag{4.6}$$

$$\mathscr{A} = \left(\frac{v_0}{v_{\rm K}}\right)^2 \left\{ 2\left(\frac{\Delta v_{10}}{v_0}\right) + \left(\frac{\Delta v_{10}}{v_0}\right)^2 \right\}, \tag{4.7}$$

where $\Delta v_{10} = v_1 - v_0$. The relation between Δv_{10} and input parameters is

$$\frac{\Delta v_{10}}{v_0} = \left\{ 1 + 2 f_{\rm imp} \left(\frac{v_{\rm K}}{v_0}\right) \cos\alpha_{\tilde{x}\tilde{y}} \cos\alpha_{\tilde{z}} + {f_{\rm imp}}^2 \left(\frac{v_{\rm K}}{v_0}\right)^2 \right\}^{1/2} - 1. \tag{4.8}$$

From above equations, the change in the semi-major axis by the velocity kick can be written as a function of $f_{\rm imp}$, $\alpha_{\tilde{x}\tilde{y}}$ and $\alpha_{\tilde{z}}$.

Next, we consider the change in the angular momentum and the eccentricity of the target planetesimal. Just before and after the impact, the angular momentum of the target planetesimal is given as

$$h_0 = \sqrt{GM_{\rm s} a_0 (1-{e_0}^2)}, \tag{4.9}$$

$$h_1 = \sqrt{GM_{\rm s} a_1 (1-{e_1}^2)}, \tag{4.10}$$

where h is the reduced angular momentum and subscripts 0 and 1 indicate before and after giving velocity kick, respectively. The change in the angular momentum $\Delta h_{\rm kick} \equiv h_1 - h_0$ is given as

$$\frac{\Delta h_{\rm kick}}{h_0} = -1 + \left(\frac{a_1}{a_0}\right)^{1/2} \left(\frac{1-{e_1}^2}{1-{e_0}^2}\right)^{1/2}. \tag{4.11}$$

Transforming this equation, we obtain the displacement in the eccentricity $\Delta e \equiv e_1 - e_0$ as

$$\frac{\Delta e}{e_0} = -1 + \sqrt{1 + \frac{1-{e_0}^2}{{e_0}^2} \left\{ 1 - \left(1 + \frac{\Delta h_{\rm kick}}{h_0}\right)^2 \left(1 + \frac{\Delta a}{a_0}\right)^{-1} \right\}}. \tag{4.12}$$

A component of the velocity kick perpendicular to the orbital plane does not change the absolute value of the angular momentum, so the change in the angular momentum due to the velocity kick is

$$\frac{\Delta h_{\rm kick}}{h_0} = f_{\rm imp} \cos\alpha_{\tilde{z}} \frac{\cos\alpha_{\tilde{x}\tilde{y}} + e_0 \cos(\psi_0 - \alpha_{\tilde{x}\tilde{y}})}{1 + e_0 \cos\psi_0} \sqrt{\frac{1-{e_0}^2}{1 + 2e_0\cos\psi_0 + {e_0}^2}}, \tag{4.13}$$

where ψ_0 is the true anomaly of the target planetesimal just before the impact. From above equations, the change in the eccentricity by the velocity kick can be written as a function of $f_{\rm imp}$, $\alpha_{\tilde{x}\tilde{y}}$, $\alpha_{\tilde{z}}$ and ψ_0.

The width of the resonance depends on the eccentricity of the target planetesimal. As shown in below, however, the change in the eccentricity is less than $\sim 30\%$ and the change in the resonant width is negligibly small. For simplicity, we approximate that $e_1 \sim e_0$. Substitute eq. (4.6), (4.7) and (4.8) into eq. (4.2)

and taking terms of first order in $f_{\rm imp}$ and e_0, we obtain the condition for stable resonant trapping as

$$f_{\rm imp}\cos\alpha_{\tilde{x}\tilde{y}}\cos\alpha_{\tilde{z}} \lesssim \frac{1-e_0\cos\psi_0}{4}\left|\frac{\Delta a_{\rm res}}{a}(e_0)\right|. \tag{4.14}$$

Under the appropriate approximations, the condition for the stable resonant trapping can be written in a simple formula. The left hand side of this equation means the velocity of impact in the direction of the velocity of the target planetesimal. As shown in this equation, the angle of the velocity kick is an important factor for the resonant breaking.

4.3 Numerical investigation in stability of resonant trapping

Here, we numerically investigate the stability of resonant trapping. We perform orbital integration for the system composed with a central star of mass $M_{\rm s}$, a planet of mass $M_{\rm p}$ and a mass-less target planetesimal, namely, the target planetesimal is treated as a test particle.The orbit of the target planetesimal is damped by the aerodynamic gas drag and reaches the equilibrium condition. After reaching the equilibrium condition, we add a velocity kick on the target planetesimal. If the change in the phase angle during one libration time is smaller than 2π, we judge that the target planetesimal is kept in the resonant trapping; which condition is written as

$$\Delta\varphi(t) \equiv \int_{t-\tau_{\rm lib}}^{t}\frac{{\rm d}\varphi}{{\rm d}\tilde{t}}{\rm d}\tilde{t} < 2\pi, \tag{4.15}$$

We integrate above equation numerically and judge the condition of resonant trapping in every libration time.

First, we investigate the stability of the external $j:j+1$ mean motion resonances in sec. 4.3.1, which is investigated by Malhotra (1993b). In sec. 4.3.2, we investigate the stability of the internal $j:j-1$ mean motion resonances.

4.3.1 Case of external resonance

4.3.1.1 Numerical settings

First, we focus on the $j:j+1$ external resonances. In this case, we consider that the planet does not migrate in radial direction and the target planetesimal is radially drifted due to the aerodynamic gas drag. The model is basically same as that used in Chap. 3, except for the disk model. We use a flat disk model, namely $\alpha_{\rm disk}=0$ and $\beta_{\rm disk}=3$, which gives $h_{\rm s}=$ const.. Here, we set $\eta_{\rm disk}$ as an input parameter. Note that this model is unrealistic and not self-consistent, however, useful for investigating the stability of resonant trapping.

The phase angle is given as

$$\varphi = (j+1)\lambda - j\lambda_{\rm p} - \varpi. \tag{4.16}$$

The planetesimal is inwardly drifted by the aerodynamic gas drag and reaches $j:j+1$ resonance. Inside the resonance, the orbital elements of the target

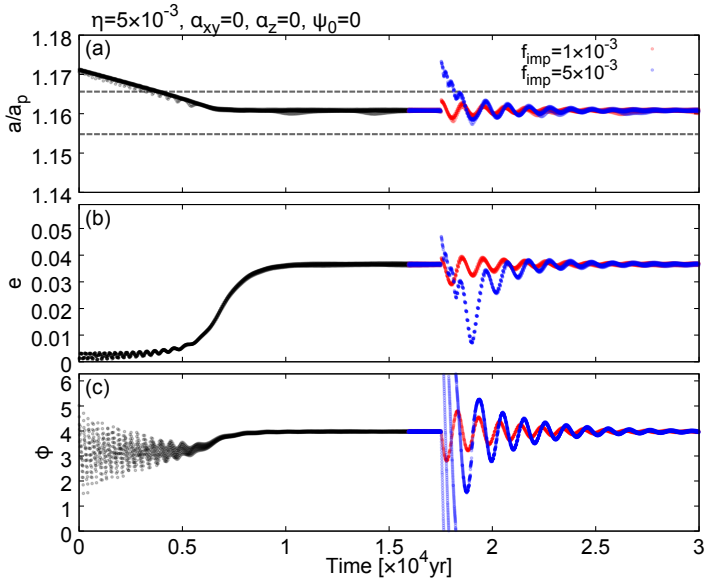

Figure 4.2: The change in (a) the semi-major axis, (b) the eccentricity and (c) the resonant argument of the target planetesimal. The target planetesimal is trapped into the $4:5$ external resonance of the planet of $M_{\rm p}/M_{\rm s} = 3\times10^{-5}$. Here, we show the case of $\alpha_{\tilde{z}} = 0$ and $\alpha_{\tilde{x}\tilde{y}} = 0$.At $t = 1.75\times10^4$yr, the velocity kick with $f_{\rm imp} = 1\times10^{-3}$ (red points) and 5×10^{-3} (blue points) are added on the target planetesimal. The dashed lines in panel (a) show the width of the resonance, which is written using $e = e_0$.

planetesimal reaches equilibrium eccentricity and resonant argument, which is given as

$$e_{\rm eq} \sim 1.12\sqrt{\frac{\eta_{\rm disk}}{j+1}}, \tag{4.17}$$

$$\sin\varphi_{\rm eq} \sim \frac{0.97\eta_{\rm disk}}{(j+1)C_{\rm r}'\tau_{\rm damp,0}}. \tag{4.18}$$

We consider the case which is similar to that in Malhotra (1993a). We set $M_{\rm p}/M_{\rm s} = 3\times10^{-5}$, $R_{\rm pl} = 8.4\times10^4$ cm, $a_{\rm p} = 5$ AU and $\eta_{\rm disk} = 5\times10^{-3}$. The gas density at the mid-plane of the circumstellar disk is $\rho_{\rm gas,0} = 5.3\times10^{-11}{\rm g/cm^3}$, which brings the damping timescale as $\tau_{\rm damp,0} \sim 1\times10^2$ yr. After reaching the equilibrium condition and passing the true anomaly $\psi = 0$, the target planetesimal is impacted by a velocity kick given by eq. (4.3). $f_{\rm imp}$, $\alpha_{\tilde{x}\tilde{y}}$ and $\alpha_{\tilde{z}}$ are input parameters which determine the strength, direction and timing of velocity kick.

4.3.1.2 Results

Figure 4.2 shows the change in (a) semi-major axis, (b) eccentricity and (c) resonant argument of the target planetesimal in our simulation. The target planetesimal is initially located at $a = 5.85$AU and radially drifted inward by the aerodynamic gas drag. After reaching the $4:5$ external resonance, the target planetesimal is trapped into the resonance and reaches the equilibrium condition with $e_{\rm eq} \sim 0.035$. A velocity kick is added at $t = 1.75\times10^4$yr with $\alpha_{\tilde{x}\tilde{y}} = 0$, $\alpha_{\tilde{x}\tilde{y}} = 0$

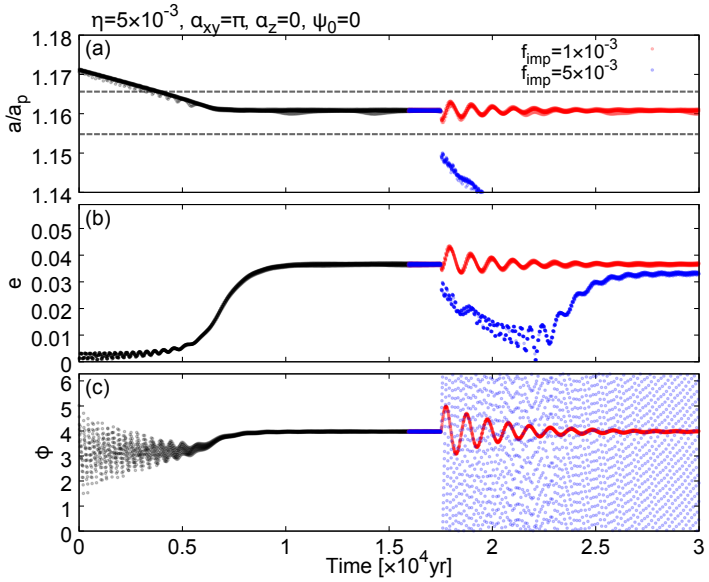

Figure 4.3: Same as fig. 4.2, but for $\alpha_{\tilde{x}\tilde{y}} = \pi$.

and $\psi_0 = 0$. The red points are the case of $f_{\rm imp} = 1 \times 10^{-3}$ and blue points are the case of $f_{\rm imp} = 5 \times 10^{-3}$. In the case of $f_{\rm imp} = 1 \times 10^{-3}$, the displacement in the semi-major axis $\Delta a_{\rm kick}$ is smaller than the resonant width. The resonant argument keeps libration around $\sin\phi_{\rm eq}$ and the planetesimal keeps trapped in the $4:5$ resonance. Due to the velocity kick, the semi-major axis and the eccentricity of the target planetesimal start libration, but converge into the equilibrium condition after a few libration time. Hereafter, we denote this result as "stable". In the case of $f_{\rm imp} = 5 \times 10^{-3}$, on the other hand, the displacement in the semi-major axis is larger than the resonant width. The resonant argument starts circulation and the planetesimal is eliminated from the resonant trapping. The planetesimal, however, is radially drifted inward and trapped into the resonance again. This is because $\Delta a_{\rm kick}$ is positive for $\cos\alpha_{\tilde{x}\tilde{y}} > 0$. After the planetesimal reaches the resonance, the resonant argument restarts libration. We denote this result as "recaptured". Figure 4.3 shows the cases of $\alpha_{\tilde{x}\tilde{y}} = \pi$. In this case, the displacement in the semi-major axis $\Delta a_{\rm kick}$ is negative. Unlike the case of $\alpha_{\tilde{x}\tilde{y}} = 0$, the planetesimal escaped from the resonant trapping cannot be trapped in the resonance again. The resonant argument once starts circulation never stop its circulation. We denote this result as "escaping".

We summarise the results of parameter study regarding $\alpha_{\tilde{x}\tilde{y}}$ and $f_{\rm imp}$ in Fig. 4.4. The green, orange and red symbols mean that the target planetesimal is resulted in the stable, recaptured and escaping conditions, respectively. The stability of the resonance strongly depends on the angle of the velocity kick. If the velocity kick is perpendicular to the velocity vector of the target planetesimal, the planetesimal can be kept in the resonance even if the velocity kick is strong as $f_{\rm imp} \sim 10^{-2}$. When $\alpha_{\tilde{x}\tilde{y}} \sim 0$, the resonance is broken for $f_{\rm imp} \gtrsim 2.3 \times 10^{-3}$, but recaptured by the same resonance because the target planetesimal is pushed into the exterior of the resonance and migrated back to the same resonance by the aerodynamic gas drag. On the other hand, when $\alpha_{\tilde{x}\tilde{y}} \sim \pi$, the resonance is broken for $f_{\rm imp} \gtrsim 2.6 \times 10^{-3}$ and the target planetesimal is never recaptured

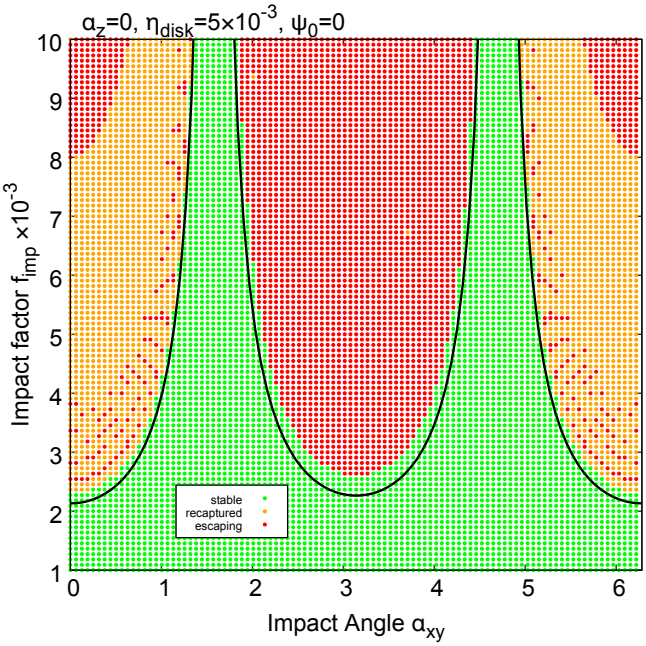

Figure 4.4: Results after giving a velocity kick on the target planetesimal trapped in the $4:5$ external resonance. Here we set $\eta = 5 \times 10^{-3}$ and $\psi_0 = 0$. The green, orange and red symbols mean that the target planetesimal is kept in the resonant trapping, eliminated from but recaptured by the same resonance, and eliminated from the resonance, respectively. Solid lines show the estimated boundary between stable and unstable velocity kick given by using eq.(4.14).

by the same resonance because it is pushed into the interior of the resonance. The black solid line shows the boundary for stable resonant trapping given by eq. (4.14). This analytical expression consists well with the numerical results.

In Fig. 4.5, we summarise the results of parameter study regarding $\alpha_{\tilde{z}}$ and $f_{\rm imp}$. As shown in eq. (4.14), the dependence on $\alpha_{\tilde{z}}$ is same as that on $\alpha_{\tilde{x}\tilde{y}}$. This is because the most important factor for resonant breaking is the displacement in the semi-major axis $\Delta a_{\rm kick}$ and which depends on both $\cos\alpha_{\tilde{x}\tilde{y}}$ and $\cos\alpha_{\tilde{z}}$. Further more, we performed parameter studies in other cases where $\eta_{\rm disk} = 1 \times 10^{-3}$ and $\psi_0 = \pi$. In any cases, the analytical expression of stable resonant trapping consists well with the numerical results.

4.3.2 Case of internal resonance

4.3.2.1 Numerical settings

Next, we focus on the $j:j-1$ internal resonance. The phase angle is given as

$$\varphi = j\lambda_{\rm p} - (j-1)\lambda - \varpi. \tag{4.19}$$

Here, we consider that a protoplanet migrates inward and traps a target planetesimal in the internal resonance. We use a flat disk model same as that used in sec. 4.3.1. For simplicity, we set $\eta_{\rm disk} = 0$. The migration timescale is same as that in chap. 3, which is given by eq. (3.5).The equilibrium eccentricity and

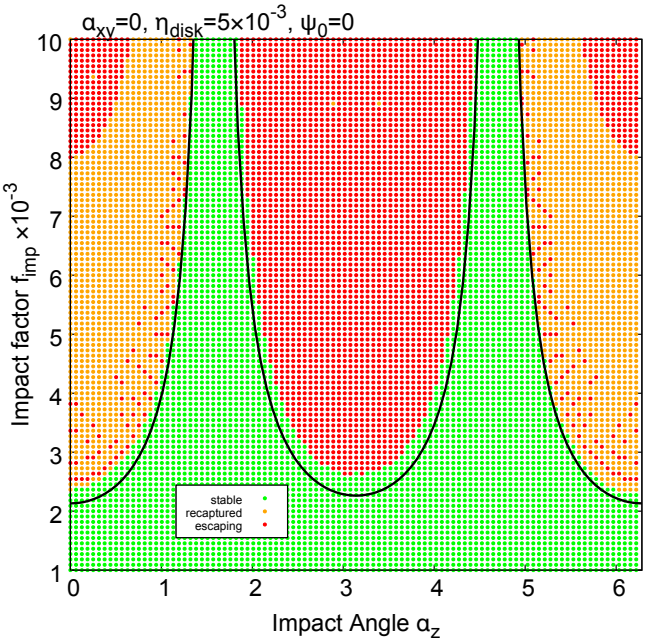

Figure 4.5: Same as Fig. 4.4, but horizontal axis shows $\alpha_{\tilde{z}}$.

resonant argument are given by eq. (3.32) and eq. (3.33) as

$$e_{\rm eq} \sim \left\{ \frac{1}{1.54(j-1)} \frac{\tau_{\rm damp,0}}{\tau_{\rm tide,a}} \right\}^{1/3},$$
$$\sin\varphi_{\rm eq} \sim -\frac{0.77 {e_{\rm eq}}^2}{C_{\rm r}\tau_{\rm damp,0}}.$$

We consider the similar conditions as previous subsection, but $R_{\rm pl} = 4 \times 10^4$ cm, which brings the damping timescale as $\tau_{\rm damp,0} \sim 4 \times 10$ yr. Here, we set $\eta_{\rm disk} = 0$, for simplicity. The planet migrates inwardly from 10AU and the target planetesimal initially locates at 8.3AU with $i = 0$. The target planetesimal will be trapped by the 5:4 internal resonance. The migration timescale is set as $\tau_{\rm tide,0} = 10^6$yr. In this case, the equilibrium eccentricity is ~ 0.019 and constant during the whole migration process.

After reaching the equilibrium condition and passing the true anomaly $\psi = 0$, the target planetesimal is impacted by a velocity kick given by eq. (4.3). $f_{\rm imp}$ and $\alpha_{\tilde{x}\tilde{y}}$ are input parameters which determine the strength and direction of the velocity kick.

4.3.2.2 Results

As the planet migrates inward, the orbits of target planetesimal initially located at $a = 8.3$AU and the planet converges, namely $a/a_{\rm p}$ approaches 1. At $5:4$ mean motion resonance, or $a/a_{\rm p} \sim 0.86$, the target planetesimal is trapped in the resonance and the eccentricity reaches the equilibrium value $e_{\rm eq} \sim 0.019$. After reaching the equilibrium condition, the velocity kick is added on the target planetesimal. Figure 4.6 shows the change in (a) semi-major axis, (b) eccentricity and (c) resonant argument of the target planetesimal when $\alpha_{\tilde{x}\tilde{y}} = 0$. The

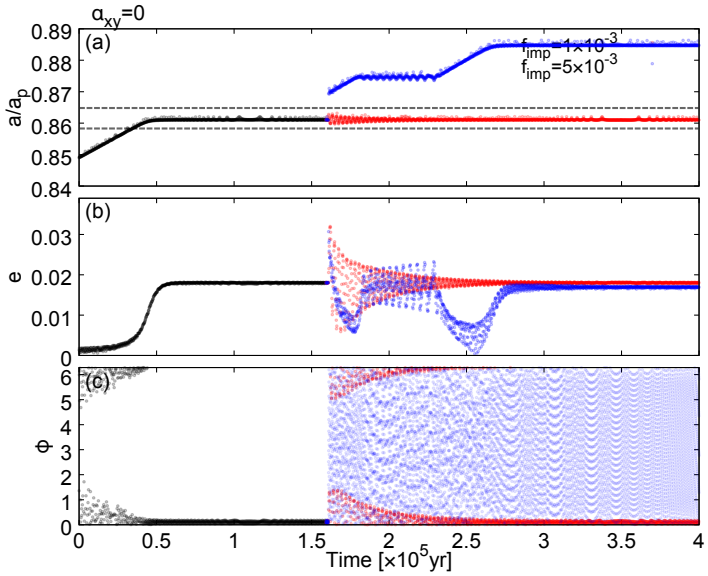

Figure 4.6: The change in (a) the semi-major axis, (b) the eccentricity and (c) the resonant argument of the target planetesimal. The target planetesimal is trapped into the $5:4$ internal resonance of the planet of $M_{\rm p}/M_{\rm s} = 3\times10^{-5}$. Here, we show the case of $\alpha_{\tilde{x}\tilde{y}} = 0$. At $t = 1.6\times10^5$yr, the velocity kick with $f_{\rm imp} = 1\times10^{-3}$ (red points) and 5×10^{-3} (blue points) are added on the target planetesimal. In panel (a), the width of the resonance is drawn with the dashed lines, which is written using $e = e_0$.

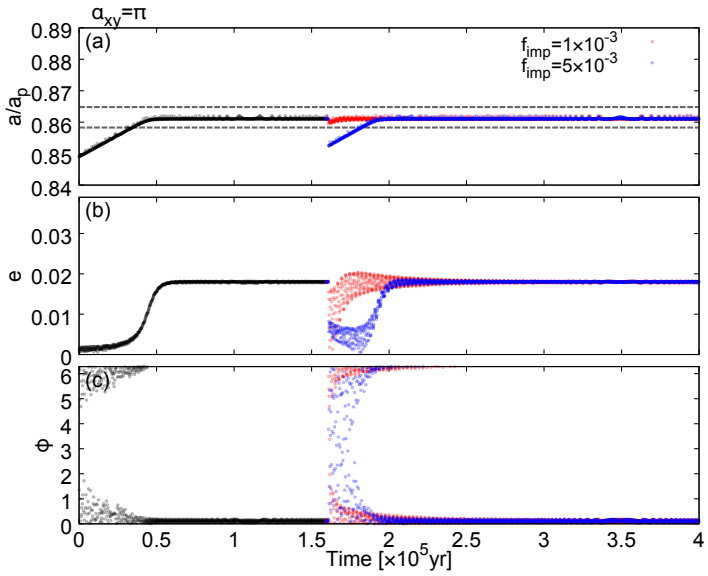

Figure 4.7: Same as fig. 4.6, but for $\alpha_{\tilde{x}\tilde{y}} = \pi$.

velocity kick is added at $t = 1.6 \times 10^5$yr. As same as the case of the external resonance shown in sec. 4.3.1, the displacement in the semi-major axis $\Delta a_{\rm kick}$ is positive. When $f_{\rm imp} = 1 \times 10^{-3}$, $\Delta a_{\rm kick}$ is smaller than the resonant width, which is shown with the dashed lines in panel (a), and the target planetesimal is kept in the resonant trapping. The resonant argument keeps libration and the result is "stable". This result is same as that in the case of external resonance. When $f_{\rm imp} = 5 \times 10^{-3}$, however, $\Delta a_{\rm kick}$ is larger than the resonant width and the target planetesimal is kicked out outer direction. Outside the resonances, $a/a_{\rm p}$ increases due to the planetary migration, so the target planetesimal cannot be recaptured by the same resonance. After escaping from the $5:4$ resonance, the target planetesimal reaches $11:9$ second-order resonance and, then, $6:5$ first-order resonance. Finally, the target planetesimal is stably trapped in the $6:5$ resonance. Figure 4.7 shows the case when $\alpha_{\tilde{x}\tilde{y}} = \pi$. In this case, the displacement in semi-major axis is $\Delta a_{\rm kick}$ negative. When $f_{\rm imp} = 5 \times 10^{-3}$, $\Delta a_{\rm kick}$ is larger than the resonant width and the target planetesimal is kicked out inner direction. The target planetesimal is recaptured by the same resonance again.

In Fig. 4.8, we summarise the results of parameter study regarding $\alpha_{\tilde{x}\tilde{y}}$ and $f_{\rm imp}$. As same as the external resonance, the stability of internal resonance also depends on the impact angle strongly. The main difference from the external resonance is that target planetesimal can be recaptured by the resonance for $\alpha \sim \pi$. This is because $\Delta a_{\rm kick}$ is negative for $\pi/2 < \alpha < 3\pi/2$ and the planet migrates inwardly. The analytical expression for the boundary reproduces the numerical results well.

From above results, we conclude that the stability of resonant trapping can be evaluated by eq. (4.14). We performed the numerical simulations in the cases of $M_{\rm p}/M_{\rm s} = 3 \times 10^{-5}$ and the $4:5$ external resonance or $5:4$ internal resonance only. However, these parameters only changes the width of the resonances, thus the derived expression can be used for other parameter cases.

4.4 Collision timescale of highly eccentric planetesimal

As shown in the previous section, resonant trapping can be broken by a velocity kick which gives the target planetesimal a sufficient semi-major axis displacement. The displacement in semi-major axis depends on the direction of velocity kick strongly. If the velocity kick vector is perpendicular to the velocity vector of the target planetesimal, breaking the resonant trapping is difficult. To evaluate the break of resonant trapping, we need to know the collision timescale and the relationship between the parameters of the velocity kick, such as $f_{\rm imp}$, $\alpha_{\tilde{x}\tilde{y}}$ and $\alpha_{\tilde{z}}$, and collision properties, such as relative velocity, collision probability and impact parameter. The final object of this section is deriving a timescale for breaking a resonant trapping by the collisions of planetesimals.

First, we show the basic picture of collisions of planetesimals which we consider here in sec. 4.4.1. We derive a collision frequency and collision probability in sec. 4.4.2, then a collision timescale in sec. 4.4.3.

4.4.1 Basic picture

Around a massive migrating planet, planetesimals are divided into two characteristic swarms: cold, damped planetesimal swarm out of the mean motion

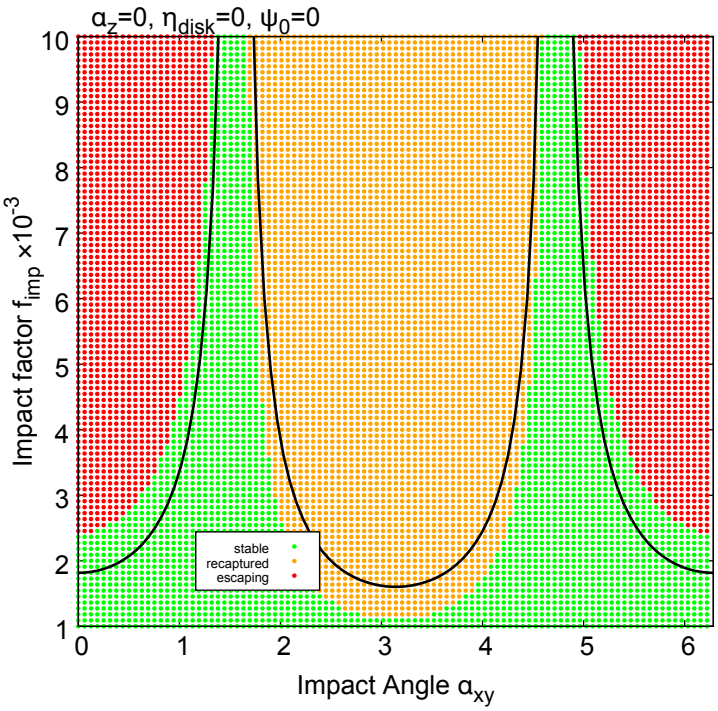

Figure 4.8: Results after giving a velocity kick on the target planetesimal trapped in the 5 : 4 internal resonance. The green, orange and red symbols mean that the target planetesimal is kept in the resonant trapping, eliminated from but recaptured by the same resonance, and eliminated from the resonance, respectively. Solid lines show the estimated boundary between stable and unstable velocity kick given by using eq.(4.14). The main difference from the cases of external resonance is that the results are recaptured for $\pi/2 < \alpha < 3\pi/2$. This difference comes from the difference of converging processes.

resonances and hot, excited planetesimal swarm in the mean motion resonances. Outside the mean motion resonances, the dominant excitation force is gravitational scattering of planetesimals, which is so weak that eccentricities of planetesimals are on the order of $\lesssim 10^{-2}$ (e.g. Ohtsuki et al. 2002). On the other hand, inside mean motion resonances, the dominant excitation force is the accumulated gravitational force from the planet. Mean motion resonances are strong enough to excite the eccentricities of trapped planetesimals up to the order of ~ 0.1 during the planetary migration. This bimodal distribution is remarkable around a migrating proto-gas giant planet.

To investigate the break of resonant trapping, we need to consider the two type of collisions between planetesimals: (i) collisions between planetesimals in the same swarm, and (ii) collisions between planetesimals in the different swarms. Inside the mean motion resonances, the resonant argument converges to ~ 0 and the conjunction point is aligned with the perihelion of the planet. The orbits of trapped planetesimals take similar shapes. The relative velocity between trapped planetesimals would be sufficiently small. On the other hand, the relative velocity between the trapped planetesimal and the planetesimal outside the resonance, which is in almost circular orbit, becomes $\sim ev_K$. As shown in sec. 4.2, the former

type collision is difficult to break the resonant trapping, however, the latter type collision is strong enough to break the resonant trapping. In this chapter, we consider the latter type of collisions, namely collisions between planetesimals in the resonances (hereafter, target planetesimals) and planetesimals outside the resonances (hereafter, impact planetesimals).

4.4.2 Collision probability of eccentric planetesimal

Collision frequency of a target planetesimal with the surrounding impact planetesimals is given as a time derivative of mean collision number $N_{\rm col}$, which is written as

$$\frac{{\rm d}N_{\rm col}}{{\rm d}t} = n_{\rm imp}\Gamma_{\rm col}u, \tag{4.20}$$

$$= \frac{3}{4}\frac{\rho_{\rm solid}}{\rho_{\rm pl}}\frac{{R_{\rm col}}^2 u}{{R_{\rm imp}}^3}, \tag{4.21}$$

$$\frac{{\rm d}N_{\rm col}}{{\rm d}\psi} = \frac{3}{8\pi}\frac{\left(1-e^2\right)^{3/2}}{(1+e\cos\psi)^2}\frac{\rho_{\rm solid}}{\rho_{\rm pl}}\frac{{R_{\rm col}}^2 u T_{\rm K}}{{R_{\rm imp}}^3}, \tag{4.22}$$

where $n_{\rm imp}$, $\Gamma_{\rm col}$ and u are number density of impact planetesimals in the circumstellar disk, effective collision cross section, and relative velocity, respectively. $\rho_{\rm solid}$ is a density of impact planetesimals in the circumstellar disk. $R_{\rm col}$ is a radius of the collision cross section given as $R_{\rm col} = R_{\rm tg} + R_{\rm imp}$, where $R_{\rm tg}$ and $R_{\rm imp}$ are radii of the target planetesimal and the impact planetesimal. In this paper, we use a geometrical cross section for $\Gamma_{\rm col} = \pi {R_{\rm col}}^2$, which means we neglect the gravitational focusing effect of the target planetesimal. This manipulation is appropriate for our purpose because the gravitational focusing effect of planetesimal-size object, e.g. $R_{\rm tg} = 100{\rm km}$, can be ignored for high-relative-velocity case as $u \sim e\, v_{\rm K}$ with $e \gtrsim 0.1$. To calculate the relative velocity u, we adapt a method used in Adachi et al. (1976), the details of which are written in Appendix B.

The structure of the planetesimal swarm is given by

$$\rho_{\rm solid}(l,z) = \frac{\Sigma_{\rm solid}(l)}{\sqrt{2\pi}h_{\rm pl}}\exp\left(-\frac{z^2}{2h_{\rm pl}^2}\right), \tag{4.23}$$

$$h_{\rm pl}(l) = l\tan\left\langle {i_{\rm imp}}^2\right\rangle^{1/2}, \tag{4.24}$$

where $h_{\rm pl}$ and $i_{\rm imp}$ are a scale height of the planetesimal disk and the inclination of the impact planetesimals. $\Sigma_{\rm solid}$ is same as chap. 3 and set by eq. (3.14). l is the radial distance of the target planetesimal from the central star.

The planetesimals in the circumstellar disk has a uniform size $R_{\rm tg} = R_{\rm imp} = R_{\rm pl} = 10^7{\rm cm}$ and a uniform density $\rho_{\rm pl} = 2{\rm g/cm}^3$. The eccentricity and inclination of the impact planetesimals is set as $\left\langle {e_{\rm imp}}^2\right\rangle^{1/2} = 2\left\langle {i_{\rm imp}}^2\right\rangle^{1/2} = 10^{-3}$. The mean velocity of the impact planetesimals in the vicinity of the target planetesimal is given as $\mathbf{v}_{\rm imp} \simeq (0, v_{\rm K}(l), 0)_{\text{polar coordinate}}$. Using this disk model and above equations, we can calculate the collision probability, which is defined as normalised collision frequency

$$P_{\rm col}(\psi) = \frac{{\rm d}N_{\rm col}/{\rm d}\psi}{\int_0^{2\pi}{\rm d}N_{\rm col}/{\rm d}\psi'{\rm d}\psi'}. \tag{4.25}$$

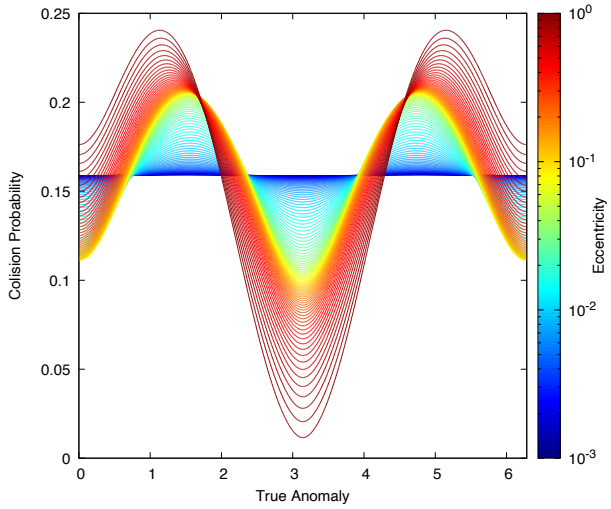

Figure 4.9: The collision probability of target planetesimal with the true anomaly. The color of solid lines show the eccentricity of target planetesimal.

Figure 4.9 shows the collision probability as a function of true anomaly ψ. The collisional probability becomes higher for $\psi \sim \pi/2, 3\pi/2$, which comes from the higher relative velocity u. When $e \lesssim 0.1$, $P_{\rm col}$ is almost same at perihelion and aphelion ($\psi = 0$ and π), but $P_{\rm col}$ becomes larger at perihelion for $e \gtrsim 0.1$. This is because the number density of the impact planetesimals at perihelion is larger than that at aphelion, and the difference is larger for larger e.

Next we consider the angle α between the relative velocity vector $\mathbf{u}$ and the velocity vector of the target planetesimal $\mathbf{v_0}$. α is given as

$$\cos\alpha = \frac{\mathbf{u}\cdot\mathbf{v_0}}{|\mathbf{u}||\mathbf{v_0}|}. \tag{4.26}$$

Fig. 4.10 shows α as a function of ψ when $i = 0$. At $\psi \sim \pi/2, 3\pi/2$, where $P_{\rm col}$ takes maximum values, the relative velocity is almost perpendicular to the velocity of the target planetesimal. As shown in sec. 4.2, resonant trapping is strong for such a perpendicular impact.

4.4.3 Collision timescale of eccentric planetesimal

The collision timescale $\tau_{\rm col}$ is defined as a time when the mean collision number $N_{\rm col}$ becomes 1, which is given as

$$1 = \int_0^{\tau_{\rm col}} \frac{{\rm d}N_{\rm col}}{{\rm d}t}{\rm d}t, \tag{4.27}$$

$$\tau_{\rm col} = \frac{2\pi}{3}\left\{\int_0^{2\pi} \frac{\left(1-e^2\right)^{3/2}}{\left(1+e\cos\psi\right)^2}\frac{\rho_{\rm solid}}{\rho_{\rm pl}}\frac{u}{R_{\rm pl}}{\rm d}\psi\right\}^{-1}. \tag{4.28}$$

$\rho_{\rm solid}$ and u are function of a, e, i, ϖ, ψ. Giving i and ϖ, we can calculate $\tau_{\rm col}$ as a function of a and e.

Figure 4.11 shows the collision timescale map in the $a-e$ plane in the case of $i = 5\times10^{-4}, \omega = 0$. $\tau_{\rm col}$ increases with a because $\rho_{\rm solid}$ and u decrease with

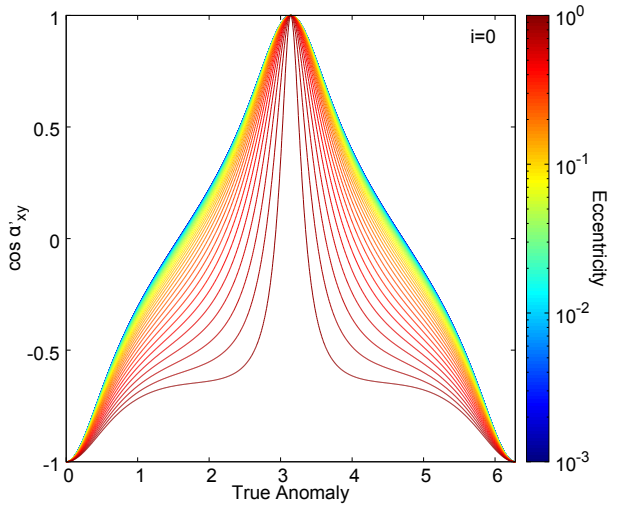

Figure 4.10: The angle between relative velocity $\mathbf{u}$ and the velocity of target planetesimal $\mathbf{v_0}$ as a function of true anomaly of target planetesimal ψ. Here we show the case where $i = 0$ or $\alpha_{\tilde{z}} = 0$. The color of solid lines show the eccentricity of target planetesimal.

a. In our model, $\tau_{\rm col}$ increases with $\sim a^3$. On the other hand, $\tau_{\rm col}$ decreases with e because u increases with e: $u \sim e\, v_{\rm K}$. $\rho_{\rm solid}$ at perihelion also increases with e: at $a = 10$ AU, for example, the perihelion is around ~ 10AU for $e = 0.05$ but $= 5$AU for $e = 0.5$, which results in about 10 times higher $\rho_{\rm solid}$ for $e = 0.5$ than that for $e = 0.05$. $\tau_{\rm col}$ is about 100 times smaller for $e = 0.5$ than that for $e = 0.05$. When the planetesimals are shepherded by the resonant trapping, $\tau_{\rm col}$ increases during the shepherding process and planetesimal collisions start when $\tau_{\rm col} \lesssim \tau_{{\rm tide},a}$ is achieved.

4.5 Effects of resonant breaking on planetesimals accretion

Above results suggest the possibility that planetesimal collisions break the resonant trapping earlier than the overstable libration, which controls the boundary of the sweet spot as shown in chap. 3. In this section, we model the mutual collision of planetesimals using the collision probability derived above. We include the collision model in the orbital evolution code used in chap. 3. Performing the numerical calculations, we investigate the effect of resonant breaking due to the planetesimal collisions on the accretion of planetesimals and the location of the sweet spot.

4.5.1 Relation between impact parameter and velocity kick

As shown in sec. 4.2, the size of velocity kick $f_{\rm imp}$ and the angle of velocity kick $\alpha_{\tilde{x}\tilde{y}}$ and $\alpha_{\tilde{z}}$ is important for breaking the resonant trapping. These parameters must relates with the relative velocity between the target planetesimal and the impact planetesimal $\mathbf{u}$, which depends on the collision point $\psi = \psi_0$. Not only where the impact planetesimal collides on the target planetesimal but also how

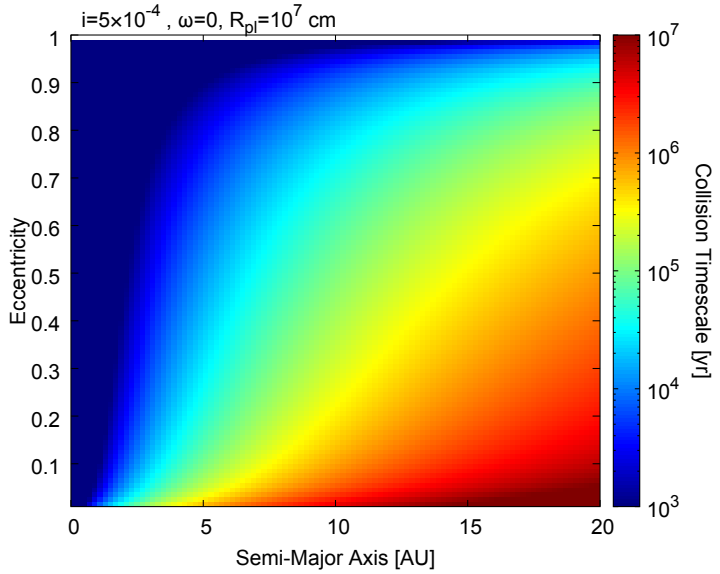

Figure 4.11: The collision timescale of the target planetesimal with the impact planetesimals in the circumstellar disk in the $a-e$ plane. Here we consider the case of $i = 5 \times 10^{-4}$ and uniform size planetesimal disk with $R_{\rm tg} = R_{\rm imp} = 10^7 {\rm cm}$. The distribution of impact planetesimals is same as the distribution of solid materials in minimum mass solar nebulae.

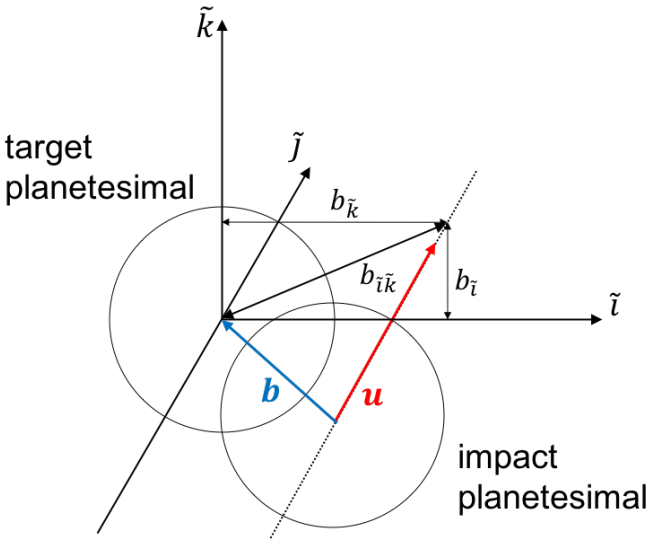

Figure 4.12: Geometrical picture for the relationship between the relative velocity $\mathbf{u}$ and impact parameter $\mathbf{b}$. $\tilde{x}$, $\tilde{y}$, $\tilde{z}$ coordinate is a Cartesian coordinate where $\tilde{y}$ axis has a same direction as the relative velocity vector $\mathbf{u}$.

the impact planetesimal collides on the target planetesimal affects the velocity kick. Here, we consider the impact parameter and the damping of velocity kick due to the break of planetesimals.High-velocity collision like $\sim 0.1\ v_{\rm K}$ results in the partial break of planetesimals(e.g. Sugiura et al. 2018), which reduces the size of velocity kick. We include these effects in our model using a simple geometrical model.

We consider that the impact planetesimal collides with the target planetesimal with impact parameter $\mathbf{b}$ and relative velocity $\mathbf{u}$. The impact parameter $\mathbf{b}$ is defined as a position vector measured from the centre of the impact planetesimal to the centre of the target planetesimal. The geometrical image of $\mathbf{b}$ and $\mathbf{u}$ is shown in Fig. 4.12. Assuming that planetesimals have spherical shapes, we obtain the velocity kick impacted on the target planetesimal as

$$\Delta\mathbf{v}_{\rm kick} = \varepsilon_{\rm p}\frac{\mathbf{u}\cdot\mathbf{b}}{|\mathbf{u}||\mathbf{b}|}, \tag{4.29}$$

where $\varepsilon_{\rm p}$ is a parameter defining the momentum transfer efficiency, which is 1 for perfectly elastic collision and 0.5 for complete merging. If the collision results in a break of the target planetesimal, fragments scattered from the target planetesimal remove momentum from the impact planetesimal and $\varepsilon_{\rm p}$ is smaller than unity. Now, we can obtain the velocity kick $\Delta\mathbf{v}_{\rm kick}$ from collision properties ψ_0, $\varepsilon_{\rm p}$ and $\mathbf{b}$.

4.5.2 Model and settings

We investigate the effect of resonant breaking on the planetesimal accretion rate and the location of the sweet spot found in chap. 3. We use the same model as chap. 3, but add a velocity kick simulating planetesimal collisions.

In the every timestep Δt, we calculate a collision probability given as

$$P_{\rm col}(\Delta t) = \frac{{\rm d}N_{\rm col}}{{\rm d}t}\Delta t. \tag{4.30}$$

To calculate the collision frequency ${\rm d}N_{\rm col}/{\rm d}t$, we use eqs. (4.21), (4.23) and (4.24). We assume that the distribution of planetesimals outside the mean motion resonances are fixed during the planetary migration and given by the same model used in chap. 3 (see eq. 3.14). This assumption is not self-consistent because planetesimal distribution is largely changed by the resonant shepherding during the planetary migration as shown in chap. 3. The surface density of planetesimal inside the resonance increases with the planetary migration. However, we focus on the collisions between the trapped planetesimals and the planetesimals outside the resonances. Our purpose is investigating the effect of breaking the resonant trapping triggered by the high-velocity collision of planetesimals. So we neglect the change in the surface density profile of planetesimals for simplicity. The validity of this assumption is discussed in sec. 4.6.1.

We also generate a random number $p_{\rm ran}$ in the range of $0 \leq\ p_{\rm ran}\ \leq 1$ in every timestep. If $P_{\rm col}(\Delta t) > p_{\rm ran}$, we add a velocity kick $\Delta\mathbf{v}$ generated by eq. (4.29). In this thesis, $\varepsilon_{\rm p}$ is set as an input parameter. For obtaining $\mathbf{b}$, we consider a Cartesian coordinate $(\tilde{i},\tilde{j},\tilde{k})$, where $\tilde{j}$ axis consists with the relative velocity vector $\mathbf{u}$, as shown in fig. 4.12. The components of $\mathbf{b} = \left(b_{\tilde{i}}, b_{\tilde{j}}, b_{\tilde{k}}\right)$ in this coordinate

are given in the range of

$$-1 \leq \frac{b_{\tilde{i}}}{R_{\rm col}} \leq 1, \tag{4.31}$$

$$-1 \leq \frac{b_{\tilde{k}}}{R_{\rm col}} \leq 1, \tag{4.32}$$

$$b_{\tilde{i}\tilde{k}} \equiv \sqrt{b_{\tilde{i}}^2 + b_{\tilde{k}}^2} \leq 1, \tag{4.33}$$

and

$$\frac{b_{\tilde{j}}}{R_{\rm col}} = \sqrt{1 - \left(\frac{b_{\tilde{i}\tilde{k}}}{R_{\rm col}}\right)^2}. \tag{4.34}$$

When the gravitational focusing effect is negligibly small, probability distributions for $b_{\tilde{i}}$ and $b_{\tilde{k}}$ take uniform function. We generate $b_{\tilde{i}}$ and $b_{\tilde{k}}$ randomly in the above ranges. We perform a parameter study in $\varepsilon_{\rm p}$ taking from 0.01 to 1. The other parameters are same as those of the reference model in chap. 3 (see table. 3.1).

4.5.3 Results

Figure 4.13 shows the change in the cumulative captured mass of planetesimals. The red, green and blue solid lines show the cases of $\varepsilon_{\rm p} = 10^{-2}$, 10^{-1}, and 10^{0}, respectively. For comparison, the result in the reference case of chap. 3, namely the case without planetesimal collisions, is plotted with the black dashed line. When $\varepsilon_{\rm p} = 10^{-2}$ and 10^{-1}, the planetesimal accretion occurs efficiently in $10{\rm AU} \lesssim a_{\rm p} \lesssim 3{\rm AU}$, which is the same results in no collision case. On the other hand, when $\varepsilon_{\rm p} = 10^{0}$, the planetesimal accretion continues even the planet migrates inner than 3AU where aerodynamic shepherding prevents planetesimals to enter the feeding zone in no collision case. In this case, the displacement in the semi-major axis due to the planetesimal collisions becomes large enough to push planetesimals into the feeding zone. The expansion of the accretion region is only found in the case of $\varepsilon_{\rm p} \sim 10^{0}$. When $\varepsilon_{\rm p} \lesssim 10^{-0.2} = 0.63$, the location where planetesimal accretion occurs efficiently is barely changed by the collision of planetesimals.

Figure 4.14 shows the change in the total mass of captured planetesimals as a function of $\varepsilon_{\rm p}$. When $\varepsilon_{\rm p} \lesssim 0.1$, the total captured mass is larger than that in the no collision case. When $\varepsilon_{\rm p} \gtrsim 0.1$, however, the total captured mass is smaller than that in the no collision case. This is because the collision of planetesimals have two effects on planetesimal accretion. First one is the acceleration of breaking the resonant trapping of $2:1$ resonance which is triggered by the overstable libration in the no collision case. Fig. 4.15 shows the fraction of planetesimals captured by the planet as a function of their source semi-major axis. In the no collision case, planetesimals initially located around the sweet spot cannot be captured by the planet because they are shepherded in the region inner than the sweet spot before escaping the resonant trapping. As shown in this figure, those planetesimals can be captured by the planet because the collisions of planetesimals break the resonant trapping earlier than the overstable libration and prevent the planetesimals shepherded inner than the sweet spot. This effect is

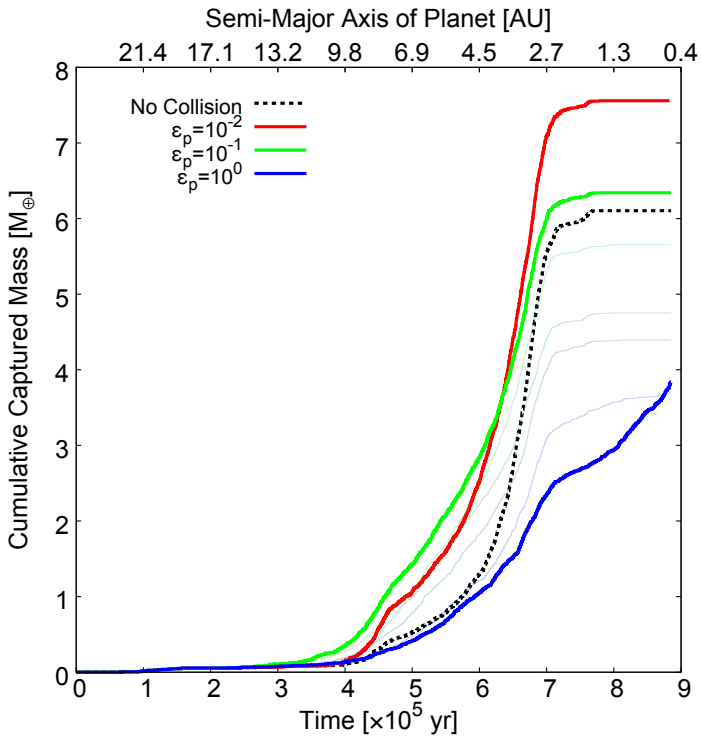

Figure 4.13: The change in cumulative captured mass of planetesimals. The semi-major axis of migrating planet at each calculation time t is written in the upper x axis. The red, green and blue solid lines show the cases of $\varepsilon_p = 10^{-2}$, 10^{-1} and 10^{0}, respectively. The thin lines show the cases of $10^{-1} < \varepsilon_p < 10^{0}$, in which line colors change from green to blue with increasing ε_p. The black dashed line show the result of the reference case in chap. 3, namely there are no planetesimal collisions.

more remarkable for larger ε_p. Second effect is the weakening of accretion band of $3:2$ resonance. Accretion bands help planetesimals to enter the feeding zone deeply. By the collisions of planetesimals, this effect is hindered and capture fraction is reduced as shown in Fig. 4.15. The fraction of captured planetesimals in the sweet spot is ~ 0.3 for $\varepsilon_p = 10^{-2}$, ~ 0.2 for $\varepsilon_p = 10^{-1}$ and ~ 0.1 for $\varepsilon_p = 10^{0}$. Thus, we conclude that the effect of accretion band is weakened by the planetesimal collisions and the fraction of captured planetesimals decreases with ε_p. The gradual decrease in the total amount of planetesimals captured with ε_p is a result of these effects. Even under the effect of the collisions of planetesimals, the planetesimals captured by the planet are limited those planetesimals initially located in the regions inside or exterior to the sweet spot even for the case of $\varepsilon_p = 1$ as shown in Fig. 4.15. We conclude that the location of the sweet spot is barely changed by the collisions of planetesimals, but the capture fraction of planetesimals reduces with the increasing ε_p.

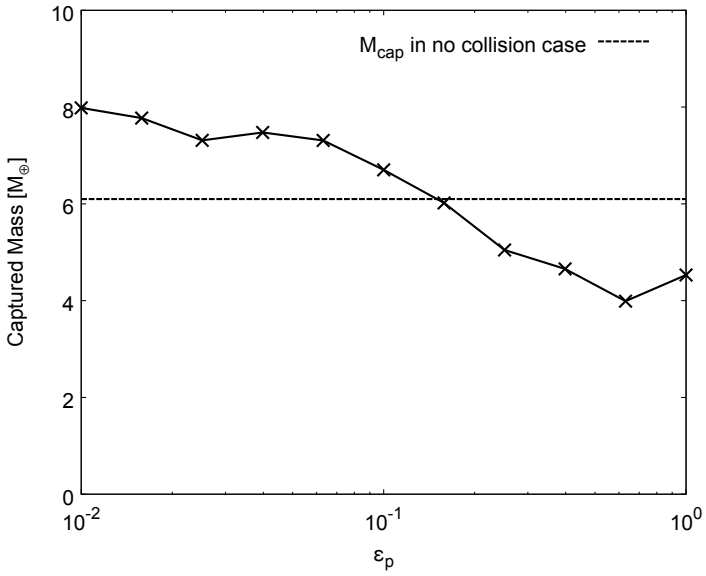

Figure 4.14: Total mass of captured planetesimals as a function of ε_p. The dashed black line show the total captured mass of planetesimals in the no collision case. The total mass of captured planetesimals gradually decreases with increasing ε_p.

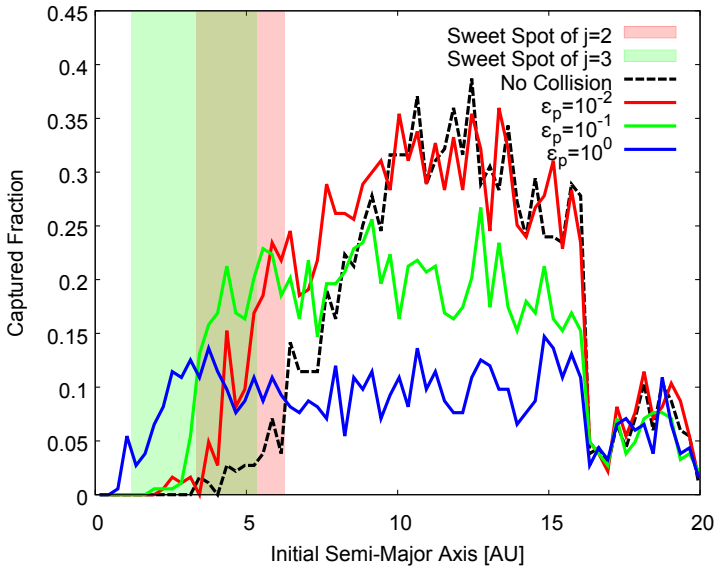

Figure 4.15: Fraction of planetesimals captured by the planet versus their source semi-major axis. The red, green and blue solid lines show the cases of $\varepsilon_p = 10^{-2}$, 10^{-1} and 10^0, respectively. The black dashed line show the result of the reference case in chap. 3, namely there are no planetesimal collisions. The red and green area show the sweet spot of $j = 2$ and $j = 3$, respectively. The bin width of the histogram is 0.3AU.

4.6 Discussion

4.6.1 Validity of collision model

In this chapter, we make many assumption to include the collisions of planetesimals in our model in a simple manner. Here we discuss the validity and limitation of our model.

In our collision model, we neglect the effect of the gravitational interactions between the target planetesimal and the impact planetesimal. The gravitational focusing effect increases the collision cross section $\Gamma_{\rm col}$. The fraction between the collision cross section and geometrical cross section is defined as a gravitational focusing factor $F_{\rm grav}$ and given as

$$F_{\rm grav} \equiv \frac{\Gamma_{\rm col}}{\pi R_{\rm col}^2} = 1 + \left(\frac{v_{\rm esc}}{u}\right)^2, \tag{4.35}$$

where $v_{\rm esc}$ is the escape velocity from the point of contact. The relative velocity between the target planetesimal and the impact planetesimals u becomes $\sim e\, v_{\rm K}$ and $F_{\rm grav}$ is almost unity when $e \gtrsim 0.01$ and $R_{\rm tg} = R_{\rm imp} = 10^7$ cm. Thus, the assumption where we set $F_{\rm grav} = 1$ never affects above results in our model.

In our simulation, we neglect the change in the planetesimal disk due to the gravitational scattering by the migrating planet. As discussed in sec. 4.5.2, the resonant arguments of shepherded planetesimals are aligned with $\varphi \sim 0$. In this case, it is expected that the relative velocity between trapped planetesimals is too small to break the resonant trapping. Thus the distribution of planetesimals inside the resonances is not important for the resonant breaking due to planetesimal collisions. The distribution of planetesimals outside the resonance, however, changes the collision frequency and the accretion rate of planetesimals. To investigate the effect of the different planetesimal distribution, we performed additional calculations where the solid-to-gas ration $Z_{\rm s}$ is changed from $0.1\, Z_\odot \le Z_{\rm s} \le 10\, Z_\odot$. Figure 4.16 shows the results of a parameter study regarding $Z_{\rm s}$ where we set $\varepsilon_{\rm p} = 0.1$ The total mass of captured planetesimals $M_{\rm cap,tot}$ normalised by the total mass of planetesimals initially distributed in our model $M_{\rm disk,tot}$ barely depends on $Z_{\rm s}$. This is because the collision frequency strongly changes with the semi-major axis $\sim a^{-3}$ and relatively weekly depends on $\sim Z_{\rm s}$. Thus, we conclude that the change in the planetesimal distribution during the planetary migration is week relative to the effect of $\varepsilon_{\rm p}$ and changes less than $\sim 20\%$ in the total captured mass of planetesimals.

4.6.2 Value of momentum transfer efficiency $\varepsilon_{\rm p}$

As shown in sec. 4.5, we find that break of resonant trapping by high-velocity collisions of planetesimals have two effects which help and hinder the planetesimal accretion. Both effects depends on $\varepsilon_{\rm p}$ and the value of $\varepsilon_{\rm p}$ is an important factor for the accretion of planetesimals.

The outcomes of planetesimal collision can be grouped in three categories; cratering, shattering and dispersing. In the first category, all or most of the mass of the impact planetesimal becomes a part of the mass of the target planetesimal. In the second category, the impact breaks up the target body into a number of pieces, but the pieces are gravitationally re-accumulated into a single body. In

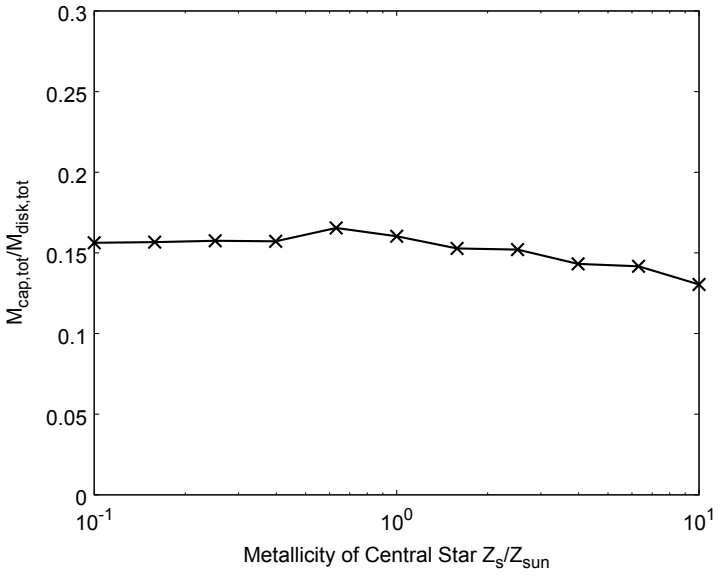

Figure 4.16: The results of a parameter study regarding the metallicity of the central star Z_s, which changes the number density of planetesimals n_{imp} and collision frequency in our model. The vertical axis shows the total mass of captured planetesimals $M_{cap,tot}$ normalised by the total mass of planetesimals initially distributed in our model $M_{disk,tot}$. Here we set $\varepsilon_p = 0.1$. The normalised captured mass barely depends on Z_s.

the cratering and shattering, the fraction of the ejected material is negligibly small. In the third category, dispersing, however, the target planetesimal is fragmented into two or more pieces and the pieces are never re-accumulated. To delineate the boundaries between these categories, the specific energy Q is used in the literature and defined as

$$Q \equiv \frac{m_{imp} u^2}{2 m_{tg}}, \tag{4.36}$$

$$\sim 4.4 \times 10^{10} \mathrm{erg/g} \left(\frac{e}{0.1}\right)^2 \left(\frac{m_{imp}}{m_{tg}}\right) \left(\frac{M_s}{M_\odot}\right) \left(\frac{a}{1\mathrm{AU}}\right)^{-1}, \tag{4.37}$$

where m_{imp} and m_{tg} are mass of the impact planetesimal and mass of the target planetesimal, respectively. Conventionally, the minimum specific energies needed for the shattering and dispersing are defined as Q^*_D and Q^*_S, respectively, and $Q^*_D > Q^*_S$. There are two distinct regimes, strength dominated regime and gravity dominated regime, determining the values of Q^*_D and Q^*_S. The bodies in the former regime are gathered by the material strength. The value of Q^*_D decreases with the size of the bodies. On the other hand, the bodies in the later regime are held together by gravitational forces. Q^*_D increases with the size of the bodies because the gravitational binding energy increases.

The outcome of planetesimal collisions are investigated by experiments for small targets in the strength dominated regime (e.g. Fujiwara et al. 1989; Davis & Ryan 1990; Arakawa et al. 2002). Using a smooth particle hydrodynamic method and a N-body code, the values of Q^*_D in the gravity dominated regime

are also investigated. The transition of the regimes occurs around $R_{\rm tg} \sim 10^4$cm-10^5cm and planetesimals with $R_{\rm tg} \sim 10^7$cm are in the gravity dominated regime. According to results of the numerical simulations (Benz & Erik 1999; Leinhardt & Stewart 2009), $Q_{\rm D}^*$ is estimated to be $\sim 10^9$erg/g at most for planetesimals with $R_{\rm tg} \sim 10^7$cm. As shown in eq. (4.37), the collisions of planetesimals considered in our simulation would result in the dispersing. Sugiura et al. (2018) also shows that the high-velocity collisions of planetesimals result in the dispersing and the large parts of the target planetesimals are removed by the collisions. The fraction of the mass loss due to the collision increases with the collision velocity.

The high-velocity collisions considered in our model would result in the dispersing and a large fraction of the mass of the target planetesimal would be removed by the collisions. Such destructive collisions would make the value of $\varepsilon_{\rm p}$ smaller than 1 because the moment brought by the impact planetesimal is partially removed by the escaping fragments from the largest remnant of the target planetesimal. The value of $\varepsilon_{\rm p}$, however, is not clear because the change in the orbit of the impacted planetesimal is not the main purpose of above studies. In addition, the velocity range of their numerical simulations is not enough for collisions of planetesimals with $e \gtrsim 0.1$, which gives the impact velocity of $\gtrsim 10^3$ m/sec around ~ 10AU. The value of $\varepsilon_{\rm p}$ should be investigated in the future.

The value of $\varepsilon_{\rm p}$ is not clear, however, the effect of $\varepsilon_{\rm p}$ on the accretion of planetesimals is limited, especially for the location of the sweet spot as shown in sec. 4.5. The location of the sweet spot is barely changed by the collisions of planetesimals except the case of $\varepsilon = 1$. $\varepsilon_{\rm p} = 1$ means the perfectly elastic collision, which is unrealistic condition for the high-velocity collisions considered in our model. The difference in the total mass of captured planetesimals shown in fig. 4.14 mainly comes from the difference in the capture fraction of planetesimals. The capture fraction decreases with the increasing $\varepsilon_{\rm p}$ as shown in fig. 4.15. Our numerical simulations show that the uncertainty in the value of $\varepsilon_{\rm p}$ is not important for the location of the sweet spot and changes the total mass of captured planetesimals by a factor of 2 at most.

4.6.3 Effects neglected in our model

In our model, we consider the high-velocity collisions of planetesimals for breaking the resonant trapping. The gravitational interactions between planetesimals, which are neglected in our model, also have a possibility to break the resonant trapping. The gravitational interactions between the trapped planetesimals generate the effects of dynamical friction and gravitational scattering of planetesimals. If the planetesimals have a size distribution, the orbits of larger planetesimals are damped by the dynamical friction from smaller planetesimals. If the eccentricity damping of dynamical friction is faster than that of aerodynamic gas drag, the overstable libration can be triggered by the dynamical friction. On the other hand, planetesimal swarms are diffused by the gravitational scattering. The diffusion in the semi-major axis of the planetesimals can push those planetesimals out from the resonant trapping. If the diffusion timescale needed for crossing the resonant width becomes shorter than the libration timescale, the diffused planetesimals would be eliminated from the resonant trapping. These effects depend on the distribution of orbital elements of planetesimals trapped

in the mean motion resonances. To investigate these effects quantitatively, we need to consider the orbital evolution of planetesimals inside the mean motion resonances.

As shown in sec. 4.6.2, the high-velocity collisions considered in our model can destruct planetesimals. The destructive collisions result in the change of size distribution of planetesimals. The change in the planetesimal size (or aerodynamic damping timescale $\tau_{\mathrm{damp},0}$) shifts the location of the sweet spot as shown in sec. 3. If the planetesimal radius gets smaller in a several orders of magnitude, the location of the sweet spot shifts outward largely. Thus, planetesimal collisions might hinder the planetesimal accretion via reduction of planetesimal radius.

Above effects should be investigated using a statistical method of planet formation or a direct orbital integration of planetesimal swarms including the interactions between planetesimals inside the mean motion resonances. We need to investigate them in future works.

4.7 Summary of Chapter4

The break of the resonant trapping regulates the planetesimal accretion onto a migrating proto-gas giant planet. In this chapter, we have investigated the break of resonant trapping due to the high-velocity mutual collisions of planetesimals. Such collisions occur in the planetary migration phase of proto-gas giant planets because planetesimals trapped in the resonances are highly excited in their eccentricities. The relative velocity between the eccentric planetesimals and circularised planetesimals is high enough to generate a strong velocity kick. First, we have derived the required condition for breaking the resonant trapping analytically. We found that the stability of resonant trapping depends not only on the strength of the velocity kick, but also the direction of the velocity kick. When the direction of the velocity kick is align to the velocity vector of the trapped planetesimal, the resonant trapping is most easily broken. On the other hand, if the direction of the velocity kick is perpendicular to the velocity vector of the trapped planetesimal, the break of resonant trapping becomes so difficult. We checked the derived condition comparing with results of the numerical simulations and found that the derived analytical expression reproduces the numerical results well. Then, we have derived the collision timescale of highly eccentric planetesimals. The collision timescale decreases with the eccentricities of the trapped planetesimals because the relative velocity and number density of the surrounding planetesimals at pericentre is higher for higher eccentricity. Finally, we have constructed a high-velocity collision model and included the model in the orbital evolution code used in chap. 3. In the collision model, the momentum transfer efficiency ε_{p} is set as an input parameter. From the numerical results, we found the effects of breaking the resonant trapping on planetesimal accretion as follows:

- The collisions of planetesimals break the resonant trapping of the inner most resonance earlier than the overstable libration.
- The effect of accretion band is weakened by the resonant breaking and the capture fraction is reduced.

- The total mass of captured planetesimals gradually decreases with $\varepsilon_{\rm p}$.
- The location of the sweet spot is not changed by the collisions of planetesimals.

We conclude that high-velocity collisions of planetesimals affect the total mass of captured planetesimals, but the location of sweet spot is barely affected by the collisions. The value of $\varepsilon_{\rm p}$ changes the total mass of captured planetesimals by a factor of 2 at most. Therefore, investigating the value of $\varepsilon_{\rm p}$ for high-velocity collisions is important for estimating the metallicity enrichment via planetesimal accretion in high accuracy.

Chapter 5

Application to planet formation

In chap. 3 and chap. 4, we investigated the accretion of planetesimals onto the migrating planet. The planetesimal accretion is considered as one of the main sources of heavy elements in gas giant planets. In this chapter, we discuss the composition evolution of gas giant planets standing on the planetesimal accretion model.

5.1 Planetesimal accretion of gas giant planets

5.1.1 Location of sweet spot

Recent observations have revealed many characteristics of exoplanets. Combining the observed parameters with the internal models of gas giant planets,

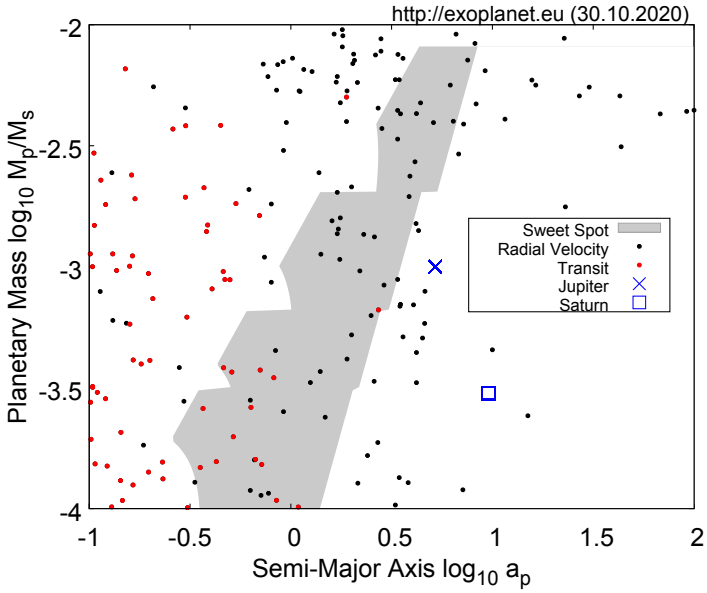

Figure 5.1: Distribution of confirmed exoplanets in the semi-major axis vs. planetary mass plane. The black points are exoplanets observed by the radial-velocity method. The red points are exoplanets observed by the radial-velocity + transit methods. As for masses of exoplanets indicated with the black points, the observe values of $M_{\rm p} \sin i$ are simply used. The gray area shows the theoretical sweet spot for planetesimal capture given by eqs. (5.1) and (5.2) with $C = 1$.

Thorngren et al. (2016) estimated the amounts of heavy elements contained in close-in gas giant planets. In this section, we estimate the amounts of metal in gas giant planets from the perspective of planet formation accompanied by planetesimal accretion. First, we construct a simple model of planetesimal accretion based on the results in chap. 3 and 4.

As shown in chap. 3, planetesimal accretion onto the migrating planet occurs in the sweet spot. The location of the sweet spot depends on the ratio of the two timescales of gas drag and tidal damping (see eq. (3.49)) and barely depends on the structure and evolution of a circumstellar disk. The planetesimals that can be captured by the migrating planet are those initially located in regions exterior to the sweet spot. In chap. 4, we consider the resonant breaking due to the high-velocity collisions of planetesimals. Using numerical calculations, we found that the location of the sweet spot is barely changed by the planetesimal collisions. The total mass of captured planetesimals is changed by the momentum transfer efficiency $\varepsilon_{\rm p}$, but, by a factor of 2 at most. For simplicity, we neglect the effect of planetesimal collisions on the planetesimal accretion. We discuss the effects of planetesimal collisions on the planetesimal accretion later.

We consider that the planet migrates in the type II regime, the migration rate for which is give by Kanagawa et al. (2018) and that the surface density profile in the circumstellar disk is given by the so-called self-similar solution (Lynden-Bell & Pringle 1974), where $\alpha_{\rm disk} \sim 1$ except around the outer edge of the circumstellar disk. Assuming the optically thin disk $\beta_{\rm disk} = 1/2$ and substituting eq. (3.49) into the analytical expressions of the sweet spots, eqs. (3.35), (3.37) and (3.38), we obtain

$$1.4C^{1/3}\left(\frac{M_{\rm p}/M_{\rm s}}{10^{-3}}\right)^{2/3}\left(\frac{j}{j-1}\right)^{7/9} < \frac{r_{\rm p}}{1{\rm AU}} < 7.6C^{1/3}\left(\frac{M_{\rm p}/M_{\rm s}}{10^{-3}}\right)^{1/3}\left\{\frac{j^5}{(j-1)^8}\right\}^{1/18}, \tag{5.1}$$

$$1.1C^{1/3}\left(\frac{M_{\rm p}/M_{\rm s}}{10^{-3}}\right)^{1/3}\left(\frac{j}{j-1}\right)^{5/18}\frac{e_{\rm cross}}{0.1} < \frac{r_{\rm p}}{1{\rm AU}}. \tag{5.2}$$

Hereafter, we consider the case of $C = 1$ (see eq. (3.50)).

Figure 5.1 shows observed exoplanets and the location of the sweet spot in the $a_{\rm p}$-$M_{\rm p}$ plane. The sweet spot locates from ~ 0.3AU to 10AU and shifts outward with the increase of planetary mass. The red and black dots show exoplanets observed by the transit method and the radial velocity method, respectively. After the onset of runaway gas accretion, $M_{\rm p}$ increases. Also, $a_{\rm p}$ decreases due to type II planetary migration. The evolution paths of gas giant planets plane can be drawn from right-bottom to left-top direction in the $a_{\rm p}$-$M_{\rm p}$. If the runaway gas accretion started in the region exterior to the water snow line, which is considered to locate at $\sim$ 1-3AU, the exoplanets currently observed in the region interior to the sweet spot crossed the sweet spot during their migration stages. On the other hand, the exoplanets currently observed in the region exterior to the sweet spot did not crossed the sweet spot. The amounts of planetesimals accreted onto the planets would differ between those two populations of planets. If we observe the difference in the amount of heavy elements between gas giant planets

inside and outside the predicted sweet spot, it would be a piece of the evidence of planetesimal accretion during planetary migration. Hereafter, we estimate the amounts of heavy elements contained in gas giant planets by constructing a simple model for planetesimal accretion.

5.1.2 A simple model of planetesimal accretion along formation paths of gas giant planets

We consider that a solid protoplanet of critical core mass $M_{\rm p} = M_{\rm p,0}$ starts runaway gas accretion at $a_{\rm p} = a_{\rm p,0}$. The planet grows in mass to $M_{\rm p} = M_{\rm p,f}$ thorough a rapid gas accretion, then the planet starts inward migration in the Type II regime and stops at $a_{\rm p} = a_{\rm p,f}$ with $M_{\rm p} = M_{\rm p,f}$ due to disk dissipation. The formation phase can be divided into two phases, mass growth phase ($M_{\rm p} : M_{\rm p,0} \rightarrow M_{\rm p,f}$) and planetary migration phase ($r_{\rm p} : r_{\rm p,0} \rightarrow r_{\rm p,f}$), and planetesimal accretion occurs in both phases. In the real formation process, the protoplanet starts migration before the gas accretion stops, but we assume that migration and gas accretion occur separately for simplicity. In this case, the total amount of heavy elements accreting onto the gas giant planets $M_{\rm Z,tot}$ can be written as

$$M_{\rm Z,tot} = M_{\rm Z,core} + M_{\rm Z,grow} + M_{\rm Z,mig}, \tag{5.3}$$

where $M_{\rm Z,core}$, $M_{\rm Z,grow}$ and $M_{\rm Z,mig}$ are the solid core mass, the amount of planetesimals accreting onto the planet in the mass growth phase, and that in the planetary migration phase, respectively.

The solid core mass is set as the critical core mass $M_{\rm crit}$, at which the protoplanet starts runaway gas accretion. Planetesimal accretion after the onset of the runaway gas accretion and core erosion have possibilities to change the core mass from the critical core mass. However, we neglect those effects in our model. Some parts of planetesimals accreting onto the planet during the gas accretion phase might reach the surface of the core before perfectly eroded into the envelope (Mordasini et al. 2006). The convection of envelope gases can erode the solid core and reduce the core mass from $M_{\rm crit}$ (Guillot et al. 2004). Both effects change the distribution of heavy elements inside the gas giant planet, but the total amount of heavy element $M_{\rm Z,tot}$ is conserved. Thus, we consider that the core mass does not change after the onset of the rapid gas accretion. Recent studies suggest $M_{\rm crit} \lesssim 10 M_\oplus$ (Hori & Ikoma 2011; Venturini et al. 2015; Brouwers et al. 2018). Here we set $M_{\rm Z,core} = 10 M_\oplus$.

In the mass growth phase, the amount of planetesimals accreting onto the planet depends on the amount of planetesimals inside the feeding zone. The accretion rate and capture probability of planetesimals depends on the timescales of planetary mass growth and gas damping of planetesimal orbits (Shiraishi & Ida 2008; Shibata & Ikoma 2019). We define the fraction of planetesimals captured by the planet in the mass growth phase $f_{\rm growth}$ as

$$f_{\rm growth} \equiv \frac{M_{\rm Z,grow}}{M_{\rm Z,fz}(a_{\rm p,0}, M_{\rm p,f})}. \tag{5.4}$$

where $M_{\rm Z,fz}$ is the amount of planetesimals inside the feeding zone given as

$$M_{\rm Z,fz}(a_{\rm p}, M_{\rm p}) = \int_{a_{\rm fz,in}(a_{\rm p}, M_{\rm p})}^{a_{\rm fz,out}(a_{\rm p}, M_{\rm p})} 2\pi r \Sigma_{\rm solid} {\rm d}r, \tag{5.5}$$

with

$$a_{\rm fz,in} = a_{\rm p}\left\{1 - 2\sqrt{3}\left(\frac{M_{\rm p}}{3M_{\rm s}}\right)^{1/3}\right\}, \tag{5.6}$$

$$a_{\rm fz,out} = a_{\rm p}\left\{1 + 2\sqrt{3}\left(\frac{M_{\rm p}}{3M_{\rm s}}\right)^{1/3}\right\}. \tag{5.7}$$

According to the results of numerical simulations by Shibata & Ikoma (2019), $f_{\rm growth}$ takes $\lesssim 0.3$.

On the other hand, in the planetary migration phase, the migrating planet can capture planetesimals which are shepherded into the sweet spot $M_{\rm Z,shep}$. During the planetary migration, planetesimals initially located from the inner edge of the sweet spot $a_{\rm SS,in}$ to the inner edge of the feeding zone when the planet starts migration $a_{\rm fz,in}(a_{\rm p,0}, M_{\rm p,f})$ have a possibility to be shepherded into the sweet spot. $M_{\rm Z,shep}$ is given by

$$M_{\rm Z,shep} = \int_{a_{\rm SS,in}}^{a_{\rm fz,in}} 2\pi r \Sigma_{\rm solid} {\rm d}r. \tag{5.8}$$

$a_{\rm SS,in}$ is given by eqs. (5.1) and (5.2). We define the fraction of planetesimals captured by the planet in the planetary migration phase as

$$f_{\rm mig} \equiv \frac{M_{\rm Z,mig}}{M_{\rm Z,shep}}. \tag{5.9}$$

According to the results in out study, $f_{\rm mig}$ takes $\lesssim 0.3$.

The both amounts $M_{\rm Z,growth}$ and $M_{\rm Z,mig}$ depend on the radial distribution of planetesimals in the circumstellar disk. Planetesimal formation has been discussed in the two formation paths: continuous coagulation of fluffy dust particles (Okuzumi et al. 2012) and gravitational contraction of particle clumps formed by the streaming instability (Youdin & Goodman 2005). In recent studies, the planetesimal formation through the streaming instability is actively discussed because it can directly form km-size planetesimals from pebble size particles skipping problems concerning the continuous growth of small particles, such as the bouncing problem of collision growth (Windmark et al. 2012). In addition, observed features in solar system Kuiper belt objects support the formation of planetesimals through the streaming instability. The Kuiper belt binaries are typically made of the similar size and the same color objects (Noll et al. 2008), which is consistent with the result that the formation of a binary is the natural result of the gravitational collapse of the pebble clump (Nesvorný et al. 2010). The streaming instability requires sedimentation of particles in disks with more than $\sim 1\%$ metallicity (Youdin & Shu 2002; Johansen et al. 2009; Simon et al. 2016). Certain locations like the vicinity of snowline (Armitage et al. 2016) or the vicinity of disk inner edge (Drążkowska et al. 2016) enhance the local disk metallicity due to the pile up of radially drifted pebbles. Even in other locations, non-laminar flow, or zonal flow originating from various instabilities, traps radially drifted solid particles and enhances local solid-to-gas ratio (see references in Klahr et al. 2018; Lenz et al. 2019). These studies suggest that planetesimal formation through the streaming instability can be triggered everywhere in the

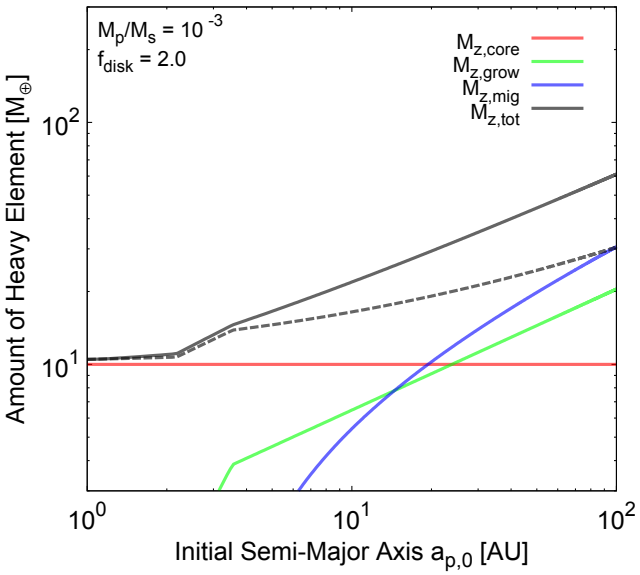

Figure 5.2: The estimated amount of heavy elements contained in the gas giant planet as a function of the initial semi-major axis of the planet $a_{\mathrm{p},0}$. We consider the case of $f_{\mathrm{disk}} = 2$ and $M_{\mathrm{p,f}}/M_{\mathrm{s}} = 10^{-3}$. The red, green and blue lines show $M_{\mathrm{Z,core}}$, $M_{\mathrm{Z,grow}}$ and $M_{\mathrm{Z,mig}}$, respectively. The black solid line shows $M_{\mathrm{Z,tot}}$ for planets which crossed the sweet spot in the planetary migration phase. The black dashed line shows $M_{\mathrm{Z,tot}}$ for planets which did not reach the sweet spot, namely $M_{\mathrm{Z,tot}} = M_{\mathrm{Z,core}} + M_{\mathrm{Z,mig}}$.

circumstellar disk. Assuming the planetesimal formation rate depends on the instantaneous radial pebble flux, Lenz et al. (2019) found that the surface density profile of planetesimals tends to be steeper than that of gas. Their model helps explain the discrepancy between the minimum-mass solar nebula, which is modeled from the distribution of solid materials in our solar system, and viscous accretion disks. Here, we consider the limiting case where planetesimal formation occurs everywhere in the disk and all solid materials are in the form of planetesimals. We set $\alpha'_{\mathrm{disk}} = 3/2$ and parameterize Σ_{solid} using a scaling factor f_{disk} as

$$\Sigma_{\mathrm{solid}} = f_{\mathrm{disk}} \times \begin{cases} 7.1 \times \left(\frac{r}{1\mathrm{AU}}\right)^{-3/2} & \text{for } r < r_{\mathrm{ice}} \\ 30. \times \left(\frac{r}{1\mathrm{AU}}\right)^{-3/2} & \text{for } r_{\mathrm{ice}} < r, \end{cases} \tag{5.10}$$

where r_{ice} is the radial distance of the water ice line and given as $r_{\mathrm{ice}} \sim 2.7\mathrm{AU}$ in our disk model. The values of Σ_{solid} for $f_{\mathrm{disk}} = 1$ is the same as that in the minimum-mass solar nebula. Given the initial formation location $a_{\mathrm{p},0}$ and observed parameters $a_{\mathrm{p,f}}$ and $M_{\mathrm{p,f}}$, we can calculate the amounts of heavy elements in gas giant planets from the above equations.

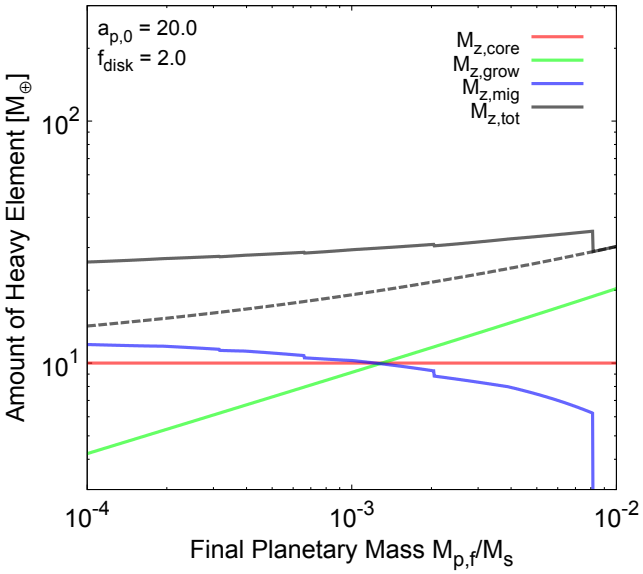

Figure 5.3: Same as Fig. 5.2, but as a function of the final planet mass $M_{\rm p,f}$. We consider the case of $f_{\rm disk} = 2$ and $a_{\rm p,0} = 20$ AU.

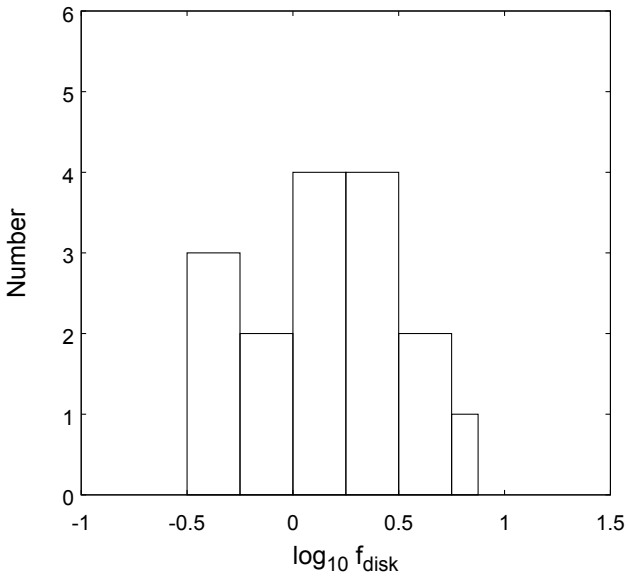

Figure 5.4: The distribution of $f_{\rm disk}$ of circumstellar disks in star formation regions. $f_{\rm disk}$ is calculated from the disk total mass $M_{\rm disk}$ and disk characteristic radius $R_{\rm disk}$ obtained in Andrews et al. (2010). Here, we assume that the disk inner edge locates at 0.1 AU and $Z_{\rm s} = Z_{\odot}$ for simplicity.

5.2 Heavy element contents in inner gas giant planets

5.2.1 Model estimation

Here we consider the amounts of heavy elements contained in gas giant planets in regions interior to the sweet spot. These planets crossed the sweet spot during their formation stages if the planets started runaway gas accretion in the outer disk as $1\mathrm{AU} \lesssim a_{\mathrm{p},0}$. We set $f_{\mathrm{growth}} = 0.3$ and $f_{\mathrm{mig}} = 0.15$, which was obtained from our numerical calculations in chap. 3. The mass of the planetesimal disk is set as $f_{\mathrm{disk}} = 2$.

Figure 5.2 shows the estimated amounts of heavy elements contained in gas giant planets $M_{\mathrm{Z,tot}}$ with the initial semi-major axis of the planet $a_{\mathrm{p},0}$. Both of the amounts of planetesimals accreting onto the planet during the mass growth phase $M_{\mathrm{Z,grow}}$ and planetary migration phase $M_{\mathrm{Z,mig}}$ increase with $a_{\mathrm{p},0}$. In the mass growth phase, the amount of planetesimals inside the feeding zone $M_{\mathrm{Z,fz}}$ increases with $a_{\mathrm{p},0}$ because the area of the feeding zone increases approximately with ${a_{\mathrm{p},0}}^2$. In the planetary migration phase, the amount of planetesimals shepherded into the sweet spot $M_{\mathrm{Z,shep}}$ increases with $a_{\mathrm{p},0}$. $M_{\mathrm{Z,mig}}$ more rapidly increases with $a_{\mathrm{p},0}$ than $M_{\mathrm{Z,grow}}$ and $M_{\mathrm{Z,mig}}$ becomes larger than $M_{\mathrm{Z,grow}}$ around $\sim 10\mathrm{AU}$. The total amount of heavy elements $M_{\mathrm{Z,tot}}$ also increases with $a_{\mathrm{p},0}$ and several tens Earth-masses of planetesimals are captured by the planet if the planet starts the runaway gas accretion $a_{\mathrm{p},0} \gtrsim 10\mathrm{AU}$.

Figure 5.3 shows $M_{\mathrm{Z,tot}}$ with the final planetary mass $M_{\mathrm{p,f}}$. Here, we set $a_{\mathrm{p},0} = 20\mathrm{AU}$. As the planetary mass increases, $M_{\mathrm{Z,grow}}$ increases because the feeding zone expands with $M_{\mathrm{p,f}}$. On the other hand, $M_{\mathrm{Z,mig}}$ decreases with $M_{\mathrm{p,f}}$ because the inner edge of the sweet spot $a_{\mathrm{SS,in}}$ moves outward. As a result, the total amount of heavy elements $M_{\mathrm{Z,tot}}$ increases slightly with $M_{\mathrm{p,f}}$.

In the above results, we considered the case where the mass of the planetesimal disk f_{disk} is set as 2. However, f_{disk} must be different from circumstellar disk to disk and $M_{\mathrm{Z,tot}}$ linearly increases with f_{disk}. f_{disk} relates with the disk total mass M_{disk}, the characteristic disk radius R_{disk} and the metallicity of central star Z_{s}. According to observations of circumstellar disks in star formation regions (Andrews et al. 2010), the most frequent disk total mass and characteristic disk radius are $\sim 0.03 M_{\odot}$ and $\sim 50\mathrm{AU}$, respectively. The disk mass and radius also have large scatterings: from $0.004 M_{\odot}$ to $0.136 M_{\odot}$ in disk total mass and from 14AU to 198AU in characteristic disk radius. Given M_{disk} and R_{disk}, we can obtain the value of f_{disk} solving

$$Z_{\mathrm{s}} M_{\mathrm{disk}} = \int_{R_{\mathrm{disk,in}}}^{R_{\mathrm{disk}}} 2\pi \Sigma_{\mathrm{solid}} \mathrm{d}r, \tag{5.11}$$

where $R_{\mathrm{disk,in}}$ is the radial distance of the disk inner edge. Assuming the disk inner edge locates at 0.1AU and $Z_{\mathrm{s}} = Z_{\odot}$, we can obtain f_{disk} from observed M_{disk} and R_{disk}. Figure. 5.4 shows the distribution of f_{disk} of circumstellar disk used in Andrews et al. (2010). Around stars with the solar metallicity, f_{disk} is most frequent around ~ 2 and scattered in a wide range. Considering the scattering in the metallicity of central stars, we argue that f_{disk} changes from ~ 0.2 to ~ 10. Thus, the distributions of $M_{\mathrm{Z,tot}}$ also has large scattering. The scattering in $M_{\mathrm{Z,tot}}$ also comes from the scattering of other parameters. $M_{\mathrm{Z,tot}}$ depends on $M_{\mathrm{Z,shep}}$, which decreases with the location of the inner edge of the

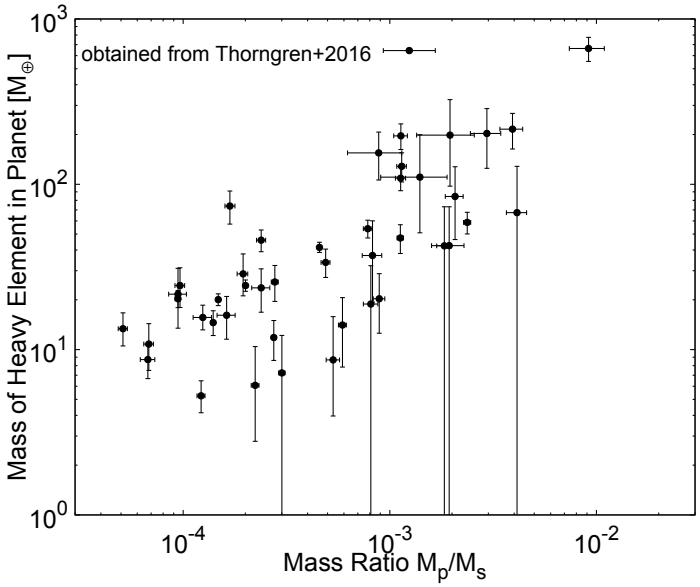

Figure 5.5: The amounts of heavy elements of gas giant planets estimated in Thorngren et al. (2016) with the mass fraction $M_\mathrm{p}/M_\mathrm{s}$.

sweet spot $a_\mathrm{SS,in}$. The location of the sweet spot depends on many parameters, such as disk viscosity α_vis, planetesimal density ρ_pl, planetesimal size R_pl, mass of central star M_s and disk temperature at 1AU $T_\mathrm{disk,0}$ as shown in eqs. (3.50) and (5.2). From eqs. (3.50), (5.2) and (5.8), we find that $M_\mathrm{Z,tot}$ depends on the $-1/6$ power of α_vis, ρ_pl, R_pl and M_s, and the $1/3$ power of $T_\mathrm{disk,0}$. Here, we use the relation of $|h_\mathrm{s}/r|_\mathrm{1AU} \propto {M_\mathrm{s}}^{-1/2}{T_\mathrm{disk,0}}^{1/2}$. The effects of the scatterings in these parameters are smaller than the effect of the scattering in f_disk, with which $M_\mathrm{Z,tot}$ increases linearly. We conclude that the scattering in $M_\mathrm{Z,tot}$ mainly comes from the scattering in the disk mass f_disk.

5.2.2 Comparison with Thorngren et al. (2016)

Some of the gas giant planets that locates in the inner disk interior to the sweet spot are observed by both the radial velocity and transit methods and, thereby, their mass and radius are both measured. Thorngren et al. (2016) estimated the amounts of heavy elements in close-in gas giant planets and found some important features in the distribution of $M_\mathrm{Z,tot}$. Figure 5.5 shows the $M_\mathrm{Z,tot}$ estimated in Thorngren et al. (2016) with $M_\mathrm{p}/M_\mathrm{s}$. Here, we focus on the features found in the distribution of $M_\mathrm{Z,tot}$; (i) $M_\mathrm{Z,tot}$ increases with $M_\mathrm{p}/M_\mathrm{s}$, (ii) $M_\mathrm{Z,tot}$ have large diversity between similar mass planets, (iii) there are some extremely enriched planets as $M_\mathrm{Z,tot} \gtrsim 100 M_\oplus$. Note that Müller et al. (2020) showed that the uncertainties originating from the model assumptions used in Thorngren et al. (2016) are comparable or even larger than those from observation. Hereafter we focus on the qualitative features obtained by Thorngren et al. (2016) and discuss the formation of close-in gas giant planets using our model.

Thorngren et al. (2016) derived a relation $M_\mathrm{Z,tot} \propto {M_\mathrm{p}}^{2/3}$ by fitting their estimated values. In Fig. 5.5, we take $M_\mathrm{p}/M_\mathrm{s}$ as the horizontal axis instead of M_p and find that $M_\mathrm{Z,tot}$ also increases with $M_\mathrm{p}/M_\mathrm{s}$. In our model, $M_\mathrm{Z,tot}$

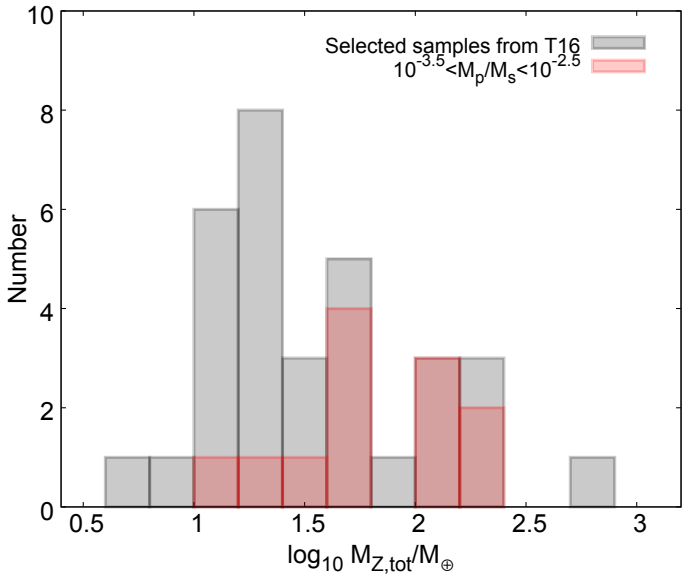

Figure 5.6: The histogram of the amount of heavy elements $M_{\rm Z,tot}$ estimated in Thorngren et al. (2016). We select only the data the errors of which are less than 50% from the samples in Thorngren et al. (2016) and the number of selected samples is 32. The black bars show the histogram of all the samples and the red bars are Jupiter-size planets which have $10^{-3.5} < M_{\rm p}/M_{\rm s} < 10^{-2.5}$. The width of the bin is set as 0.2 in logarithmic scale.

depends on $M_{\rm p}/M_{\rm s}$ but the dependence is too weak to explain the observed relation between $M_{\rm Z,tot}$ and $M_{\rm p}/M_{\rm s}$ (see Fig. 5.3). On the other hand, $M_{\rm Z,tot}$ increases with $a_{\rm p,0}$ (see Fig. 5.2). To explain the relation between $M_{\rm Z,tot}$ and $M_{\rm p}/M_{\rm s}$, we suggest that heavier close-in gas giant planets had formed cores of critical mass farther away from the central stars and then migrated over longer radial distances. Such a relation between the initial formation location and the final planet mass of gas giant planet is also suggested from the formation theories of gas giant planets. The model combining the gas accretion rate and planetary migration rate (Tanigawa & Ikoma 2007; Tanigawa & Tanaka 2016) showed that planets which start runaway gas accretion in the outer disk grow to be heavier planets. The evolution paths shown in population synthesis models (e.g. Bitsch et al. 2015; Mordasini 2014; Ida et al. 2018) also imply that heavier gas giant planets migrate longer radial distances and the possibility for Jupiter-mass planets to migrate several tens AU in planetary migration phase. On the other hand, Tanaka et al. (2020) showed that close-in gas giant planets with $M_{\rm p}/M_{\rm s} \lesssim 10^{-2}$ had started runaway gas accretion interior to the water snow line and migrated only a few AU in their formation stages. Along their formation paths, close-in gas giant planets barely capture planetesimals and the outcome is inconsistent with the result in Thorngren et al. (2016).

In the above formation models, the radial migration distance of gas giant planets is determined by the competitions between the timescales of gas accretion and planetary migration. Both timescales depend on the gap structure opened by the planet and the studies of these timescales are still under discussion, especially for the gas accretion timescale. Tanigawa & Watanabe (2002)

investigated the gas accretion rate of giant planets using a two-dimensional hydrodynamic simulations. They found that gas accretion occurs through a narrow band and derived an analytical formula for the width of the accretion band. Three-dimensional hydrodynamic simulations, however, showed the possibilities that gas accretion rate is smaller than that obtained in two-dimensional hydrodynamic simulations (Lissauer et al. 2009; Machida et al. 2010). The timescale of type II migration is regulated by the viscous timescale of the circumstellar disk in the classical regime (e.g. Lin & Papaloizou 1993). However, Kanagawa et al. (2018) investigated the migration timescale using two-dimensional hydrodynamic simulations and found that the migration timescale for gap opening planets is longer than the classical one. In the model of Tanaka et al. (2020), the migration timescale is long relative to the gas accretion timescale, which results in the short migration distance. If the migration rate is faster than that used in their model, the migration distance becomes longer. Thus, our model suggests the possibility that gas accretion timescale is longer than that obtained in two-dimensional hydrodynamic simulations.

The large scattering in $M_{\rm Z,tot}$ between similar mass planets is also important characteristic of close-in gas giant planets. Figure 5.6 shows the histogram of $M_{\rm Z,tot}$ estimated in Thorngren et al. (2016). To draw this figure, we select only the data, the errors of which are less than 50% from the samples in Thorngren et al. (2016) and the number of selected samples is 32. The black bars show the histogram of all the samples and the red bars are Jupiter-size planets which have $10^{-3.5} < M_{\rm p}/M_{\rm s} < 10^{-2.5}$. The distribution of $M_{\rm Z,tot}$ of Jupiter-size planets spreads from $10M_\oplus$ to $200M_\oplus$ and the peak of the distribution is around $50M_\oplus$. As discussed in sec. 5.1.2, the scattering in $M_{\rm Z,tot}$ mainly comes from the scattering of $0.2 \lesssim f_{\rm disk} \lesssim 10$, which covers the scattering found in $M_{\rm Z,tot}$ estimated by Thorngren et al. (2016). The effects of other parameters, such as the disk viscosity or planetesimal radius, are not enough to generate such a large scattering. We suggests that the large scattering shown in the distribution of $M_{\rm Z,tot}$ comes from the scattering of $f_{\rm disk}$. This suggestion should be discussed in future when the number of observations in $M_{\rm Z,tot}$ and circumstellar disk increases.

Finally, we focus on some close-in gas giant planets that contain more than $100M_\oplus$ heavy elements as shown in Fig. 5.5. To capture such massive heavy elements via planetesimal accretion, those planets need to be formed in a massive circumstellar disk as $f_{\rm disk} \sim 10$ and migrate more than $\gtrsim 50$AU. Disk instability model is preferred for such formation paths of gas giant planets than core accretion model. Our model suggests that close-in gas giant planets containing more than $100M_\oplus$ heavy elements formed via disk instability.

5.3 Heavy element contents in outer gas giant planets

Gas giant planets which locate in the region exterior to the sweet spot are observed by radial velocity method and, thereby, their masses are measured as shown in fig. 5.1. Jupiter and Saturn also locate in this region. Here we consider the amounts of heavy elements contained in gas giant planets which locate in the region exterior to the sweet spot.

5.3.1 In exoplanets

We consider the heavy elements contents in exoplanets observed in the region exterior to the sweet spot. Here, we consider the single gas giant planet and do not consider the outward migration as considered in Grand-Tuck model (Walsh et al. 2011), which occurs in multi-planetary systems. During the formation phase, the circumstellar disk dissipated before the planets reached the sweet spot. In this case, the accretion of planetesimals did not occur in the planetary migration phase. A clear difference in $M_{\rm Z,tot}$ would exist between the populations of planets which locate in the regions interior and exterior to the sweet spot. If we can observe the clear difference in $M_{\rm Z,tot}$ between these populations, it suggests that the heavy elements in gas giant planets are mainly brought by planetesimal accretion.

The transition frequency decreases with the orbital period of planets. The transition probability also decrease with the orbital period of planets. So the transit observation of planets in the region exterior to the sweet spot is lack now. Considering the scattering of $M_{\rm Z,tot}$, we need large number of observations to compare the populations.We need long term and wide field observations.In addition, we need high accuracy in measuring the radius of those gas giant planets. If the formation of core starts around $a_{\rm p,0} \sim 20$AU in the disk of $f_{\rm disk} = 2$, the planets which crossed the sweet spot contain more $\sim 10 M_\oplus$ heavy elements than the planets which did not reached the sweet spot during the planetary migration phase. The $10 M_\oplus$ difference in the amount of heavy elements in Jupiter-mass planet makes a few percent difference in the radius of the planets $\sim 0.01\ R_{\rm Jup}$ (Thorngren et al. 2016). $\sim 1\%$ accuracy in the observation of planet radius is limited for some planetary systems (e.g. Kostov et al. 2016). In conclusion, long term and wide field observations with high accuracy are required for comparing the populations of planets in the regions interior and exterior to the sweet spot. Such observation should be done in future.

5.3.2 In Jupiter and Saturn

For the gas giant planets in our solar system, not only the mass and radius but also the gravitational moments J_n are observed by spacecrafts exploration. As already described in chap. 1, the bulk amounts of heavy elements contained in Jupiter and Saturn are estimated $\sim$ 24-46$M_\oplus$ and $\sim$ 16-30$M_\oplus$, respectively. Jupiter and Saturn locate in the region exterior to the sweet spot. The accretion of planetesimals did not occur in planetary migration phase. The heavy elements in Jupiter comes from the initial core and accretion of planetesimals in mass growth phase. In this case, the amount of heavy elements increases with $f_{\rm disk}$, $a_{\rm p,0}$ and $M_{\rm p,f}$. Several tens Earth-masses of heavy elements estimated in Jupiter suggests that Jupiter formed in more than five times heavier circumstellar disk than the minimum-mass solar nebula (Shibata & Ikoma 2019), or Jupiter's core formed in outer disk. Jupiter and Saturn formed in the same circumsolar disk, so the difference in the amount of heavy elements comes from the different values of $a_{\rm p,0}$ and $M_{\rm p,f}$. Considering that Saturn contains comparable or smaller amount of heavy elements relative to Jupiter, we suggests that the core formation region of Saturn was outer than that of Jupiter, but at most two times outer than that of Jupiter.

Asteroid belt also gives important constraints on the formation of Jupiter and Saturn. If Jupiter core formed in outer disk as several tens AU, much amount of planetesimals were shepherded by the mean motion resonances. More than several $M_\oplus$ planetesimals were shepherded into the asteroid belt even in the disk of $f_{\rm disk} = 1$, which is inconsistent with the estimated total amount of solid materials currently distributes in asteroid belt $4 \times 10^{-4} M_\oplus$ (Pitjeva & Pitjev 2018). Formation mechanisms of Kirkwood gaps could reduce the amount of planetesimals around the mean motion resonances of Jupiter, however, removing several Earth-masses planetesimals was difficult because removed planetesimals had been brought into the inner rocky planets. So the migration distance of Jupiter need to be small.

Grand-Tuck model (Walsh et al. 2011) proposed the solution for the small total mass of asteroid belt considering the orbital evolution where Jupiter and Saturn had interacted each other. In their model, Jupiter and Saturn changes migration direction at 1.5AU from inward to outward, which makes possible for gas giant planets observed outer than the sweet spot to accrete planetesimals during their planetary migration phase. Planetesimals initially located around 1-3AU are shepherded into the inner planetesimals disk and terrestrial planets formed in the concentrated planetesimal disk. After the passage of Jupiter migrating outward, a small amount of planetesimals are scattered from other regions and left in the asteroid belt. In this case, Jupiter crossed the sweet spot and some parts of shepherded planetesimals accreted onto the planet. In their original model, however, only a few Earth-masses of planetesimals is captured by Jupiter because the radial distance of inward migration is small $a_{\rm p,0} = 3$AU and the initial distribution of solid material is similar to minimum-mass solar nebula $f_{\rm disk} \sim 1$. To accrete several tens Earth-masses of planetesimals, we need to consider the case where $a_{\rm p,0}$ and $f_{\rm disk}$ are larger than those in their original model. For Saturn, $M_{\rm Z,mig}$ might be much smaller than that of Jupiter because planetesimals had been shepherded by Jupiter when Saturn migrates inward. Thus, Grand-Tuck model has a possibility that the structure of asteroid belt and the amount of heavy elements in Jupiter and Saturn are explained in one model. However, large amount of planetesimals are shepherded into the inner disk and final structure of terrestrial planets might be changed from that of the original model. Numerical simulations must be done for further discussions.

5.4 Model limitation and comparison with other models

In this chapter, we discussed the origin of heavy elements in gas giant planets considering that the planetesimal accretion is a main source of those heavy elements. Our model stands on several important assumptions and neglects other mechanisms proposed as a source of heavy elements. Here, we discuss the model assumptions and compare our model with other composition evolution models.

The key assumption of our model is that all solid materials are in the form of planetesimals. In our model, we neglect the continuous growth of planetesimals via mutual collision of planetesimals. As already discussed in the sec. 3.5.3, many other planets would form before a gas giant planet starts migration. The existence of other planets would reduce the accretion of planetesimals because the gravitational scattering of other planets breaks the resonant trapping. So

the amount of heavy elements obtained by the planetesimal accretion would be reduced by the existence of other planets. In addition, we neglect the effect of planetesimal collisions on the capture of planetesimals. As shown in chap. 4, the planetesimal collisions change the amount of captured planetesimals by a factor of 2 at most. These effects change the value of $f_{\rm mig}$ used in our model. In this thesis, we set $f_{\rm mig} = 0.15$ based on the results of numerical simulations in chap. 3. In future work, the value of $f_{\rm mig}$ should be investigated in the model including above effects neglected in our model. Some important features obtained in our model would be valid even in the case where $f_{\rm mig}$ is altered by the above effects. The first one is that the amount of heavy elements increases with the semi-major axis of core formation region. The second one is that the scattering in $M_{\rm Z,tot}$ mainly comes from the diversity of the planetesimal disk mass. There features could explain the distribution of $M_{\rm Z,tot}$ obtained in close-in gas giant planets in Thorngren et al. (2016).

Other than the planetesimal accretion, the giant impacts of gas giant planets and the accretion of enriched disk gas are proposed as sources of the heavy elements in gas giant planets. Ginzburg & Chiang (2020) considered the giant impacts of growing gas giant planets. In their model, the decreasing trend in the metallicity of close-in gas giant planets with the planetary mass found in Thorngren et al. (2016) is well reproduced. The scattering in $M_{\rm Z,tot}$ can be explained by the difference of the number of giant impacts and initial core mass. In their model, however, the highly enriched planets which contain more than $\sim 100 M_\oplus$ heavy elements need several times impacts of planets containing massive solid core $\sim 30 M_\oplus$. As described in chap. 1, recent studies suggest that critical core mass is $\lesssim 10 M_\oplus$ and the formation of massive solid core is difficult (Hori & Ikoma 2011; Venturini et al. 2015, 2016).In addition, the region where the giant impacts of growing gas giant planets occur is limited around ~ 10AU in their model. If the core formation region is fixed around ~ 10AU, forming the diversity of gas giant planets observed in exoplanetary systems might be difficult.

The accretion of enriched disk gas is also proposed as a source of heavy elements (Guillot et al. 2006; Madhusudhan et al. 2014; Booth et al. 2017; Notsu et al. 2020). The metallicity of disk gas is enhanced by the photo-evaporation (Guillot et al. 2006) and reduced by the condensation of disk gas (Madhusudhan et al. 2014). Pebbles drifting in radial direction transport condensed materials from outer to inner disk and increase the elemental abundances of gas around snow lines due to the sublimation of volatile ices (Booth et al. 2017; Booth & Ilee 2019). The disk gas metallicity can be increased by these effects and the enhancement values differ in each region divided by snow lines. The accretion of these enriched disk gas brings large amount of heavy elements in gas giant planets. However, the enrichment of gas giant planets metallicity in this process is estimated as ten times larger than that of central star at most Madhusudhan (2019), which cannot explain the highly enriched close-in gas giant planets estimated in Thorngren et al. (2016).

Relative to other composition evolution models, we conclude that planetesimal accretion is good at three points: (i) The large scattering found in $M_{\rm Z,tot}$ of close-in gas giant planets can be explained by the diversity of circumstellar disk. (ii) The relationship between $M_{\rm Z,tot}$ and $M_{\rm p}/M_{\rm s}$ found in the close-in gas giant planets can be explained if the cores of heavier planets form in the region farther from the central star. (iii) The planetesimal accretion has a potential

to bring $\sim 100 M_{\oplus}$ heavy elements into gas giant planets. In addition, due to the existence of the sweet spot, planetesimal accretion model makes a gap in the mean value of $M_{\mathrm{Z,tot}}$ between the populations of planets locate in the region interior and exterior to the sweet spot. This feature cannot be seen in other models. Thus, the observation of this gap will be a smoking gun of planetesimal accretion as a main source of heavy elements in gas giant planets.

Chapter 6

Future perspectives and summary

6.1 Future perspectives

6.1.1 Unresolved problems

The numerical simulations performed in this thesis have revealed the physical mechanisms underlying in the planetesimal accretion. The numerical results in this thesis, however, also shed light on the importance of physical processes neglected in our models.

The existence of other planets should be considered in future works. As pointed in sec. 3.5.3, the gravitational scattering from the other planets changes the effects of mean motion resonances and the distribution of planetesimals in the circumstellar disk. The effects of other planets can be investigated by the numerical simulations of multi-planetary systems, but the conditions of the formation of multi-planetary systems depends on many parameters, such as masses and initial semi-major axes of each planet. The interactions between planets are also expected to play important roles in the cases. Thus, we need to investigate the formation of multi-planetary systems at the same time. The multi-planetary systems are already observed and there are three multi-gas-giant-systems in the samples of Thorngren et al. (2016), that are K2-24, Kepler-9 and Kepler-30. The number of multi-planetary systems where the compositions of each planet are estimated will increase with the progress of transit observations. We should improve our knowledge about the composition evolution of planets in multi-planetary systems from the theoretical approach.

The effect of the collisions between planetesimals on planetesimal accretion is investigated in chap. 4, but the effects of collisional growth and destructive collision are neglected in our study. To investigate these effects, we need to consider the size distribution of planetesimals. The N-body integration would not be applicable to this simulation because we need to use large number of particles for each size of planetesimals. Thus, we should combine the statistical model with our model. In addition, the gravitational interactions between planetesimals might affect the roles of resonant trapping, especially for smaller planets because mean motion resonances are weaker for smaller planets. In our study, we focused on the gas giant planets, but the formation of smaller planets, such as the formation of cores of critical mass, is still actively discussed problem. It is worth reconsidering the growth of rocky planets under the type I planetary migration, which is considered in Tanaka & Ida (1999). Before we consider the cases of the formation of such small planets, we should investigate the above

interactions between planetesimals.

6.1.2 Future application to observations

In the next decades, the observations of transmission spectra of gas giant planets' atmospheres will proceed rapidly with space missions such as James Webb Space Telescope (Gardner et al. 2006) or Ariel (Tinetti et al. 2018). Those observations make constraints on detailed atmospheric compositions, such as C/O ratio in the atmosphere, possible. In this thesis, we focused on the bulk metallicity of gas giant planets; however, it would be important to consider the detailed composition of gas giant planets and the distribution of each element in gas giant planets. To link the formation theory and such observations, we need to consider the two physical mechanisms; the composition evolution of gas and planetesimals in the circumstellar disk and the distribution of heavy elements in gas giant planets. The C/O ratio of planetesimals changes with the radial distance from the central star. The distribution of heavy elements should be investigated using the internal structure model of gas giant planets. The interaction between the envelope and atmosphere is important to estimate the atmospheric composition of gas giant planets. Where the accreted materials are deposited in gas giant planets depends on the timing of planetesimal accretion and the evolution of internal structure of gas giant planets. Thus, we should combine the model of planetesimal accretion with the model of internal structure of gas giant planets and solve them at the same time.

The distribution of planetesimals in circumstellar disks directly affects the composition of gas giant planets. We assumed that all solid materials are turned into planetesimals and the radial drift of solid materials before turning into planetesimals are neglected. If the total amount of planetesimals is smaller than that of pebbles or embryos, other proposed mechanisms of heavy elements accretion, such as the giant impacts of embryos or the accretion of enriched disk gas, dominate the composition evolution of gas giant planets. We can constrain the dominant mechanism by comparing the final results of each mechanism with observations, but it is also important to investigate the formation of planetesimals because we can narrow the parameter regions concerning to the initial conditions of solid materials. The evolution of the solid to gas ratio in a circumstellar disk and the formation rate of planetesimals regulate the state of solid materials when the gas giant planets start their formation. The important physical process is the growth of solid materials from the size of pebble to that of planetesimal. Studies in planetesimal formation would help linking the planetary composition with the formation of gas giant planets.

The observed compositions of gas giant planets tell us the history of their formation. It would be still difficult to observe the formation of planets directly even in the next decades. Thus, the theories linking the current conditions of planets with their formation processes are important. As in the previous 20 years, observations will keep improving our knowledge about exoplanets drastically and make statistical discussions of exoplanets distribution possible. The theoretical models linking observations with planetary formation theories should be improved with the progresses in observations. Studies about the above problems would make great progresses in this field of science.

6.2 Conclusion and Summary

The formation of gas giant planets involves many physical processes such as circumstellar disk evolution, core formation, gas accretion and planetary migration. Thanks to active progresses in respective theoretical studies, we can construct unified planetary formation models from planetesimals to gas giant planets. Along with the development of observation and characterisation of exoplanets, we can constrain the theoretically proposed formation models and the initial parameters shaping the formation fields of gas giant planets, which are not observable in current exoplanetary systems. The bulk composition of gas giant planets is used for retrieving the initial condition of gas giant planet formation because the composition evolution of gas giant planets is strongly related with the evolution paths of gas giant planets. Planetesimal accretion is one of the main sources of heavy elements (or metals) of gas giant planets. Planetesimal accretion during the migration of proto-gas giant planets is, however, not well understood because the role of mean motion resonances in this process is unclear. Thus, in this thesis, we have investigated the effects of mean motion resonances on planetesimal accretion onto a migrating proto-gas giant planet in a circumstellar gaseous disk.

In chap. 3, we have considered the limiting case where the mean motion resonances work most strongly with the aim to reveal the fundamental physics of planetesimal accretion. Using direct orbital integration of planetesimals, we have found that mean motion resonances play important roles in planetesimal accretion. The main results of our numerical simulations are as follows:

- Planetesimal accretion is controlled by mean motion resonances with the migrating planet and aerodynamic gas drag. There is a sweet spot in the circumstellar disk where planetesimal accretion occurs efficiently.
- The total amount of planetesimals captured by the planet increases with the amount of planetesimals shepherded into the sweet spot during the planetary migration.
- The location of the sweet spot barely depends on the structure and evolution of the circumstellar disk.
- Resonant trapping leads to shifting the sweet spot inward and enhancing the accretion of planetesimals due to the effect of accretion bands.

The results of chap. 3 sheds light on another process in planetesimal accretion. Resonant trapping by gas giant planets enhances the eccentricities of trapped planetesimals, which brings high-velocity collisions of planetesimals. Such strong collisions can break the resonant trapping, which regulates the location of the sweet spot and the accretion of planetesimals. In chap. 4, we have derived the condition for breaking the resonant trapping analytically and found that the high-velocity collisions of planetesimals are strong enough to break the resonant trapping. Including the effect of planetesimal collisions in the orbital integration code, we have investigated the effect of planetesimal collisions on planetesimal accretion. The main results of numerical simulations are as follows:

- Collisions of planetesimals break the resonant trapping of the inner most resonance earlier than the overstable libration.

- The total amount of captured planetesimals is changed by a factor ~ 2 at most.
- The location of the sweet spot is not changed significantly by the collisions of planetesimals.

Finally in chap. 5, we have discussed the effect of planetesimal accretion on the composition evolution of gas giant planets and tried to constrain their formation processes. Using the results obtained above, we have constructed a simple model for estimating the amount of heavy elements brought by the planetesimal accretion. Our model shows

- a Jupiter-mass planet can accrete several tens Earth-mass planetesimals if the core forms in the outer disk at $\gtrsim$ 10AU in MMSN,
- the amount of heavy elements in gas giant planets increases with the semi-major axis of core formation location,
- the amount of heavy elements strongly depends on the planetesimal disk mass,
- gas giant planets observed in the region interior to the sweet spot have more heavy elements than those exterior to the sweet spot.

Comparing the estimated amount of heavy elements in gas giant planets by Thorngren et al. (2016), we suggests

- close-in gas giant planets migrated over tens AU in their formation stages and the migration distance was longer for heavier planets,
- the large scattering in the amount of heavy elements comes from the planetesimal disk diversity,
- extremely enriched close-in gas giant planets which contain more than $\sim$ 100 $M_\oplus$ formed via gravitational instability.

Our model can explain the various characteristics of heavy elements distribution in close-in gas giant planets. This results suggest that planetesimal accretion is a main source of heavy elements in gas giant planets. If we can observe the amounts of heavy elements in gas giant planets orbiting far from their central star, we can constrain the source of heavy elements more strongly.

Our models used in this thesis contain many assumptions and simplifications, on which we need further investigations. However, we showed that the various features found in the distribution of heavy element contents in close-in gas giant planets can be explained by the effect of planetesimal accretion. The findings in this thesis are expected to make a great contribution in linking the current composition of gas giant planets with their formation history. Along with the future development of observation and characterisation of exoplanets, the formation paths of gas giant planets will be constrained by the models including the effects of planetesimal accretion in planetary migration phase.

Acknowledgements

First, I would like to show my deepest gratitude to my PhD supervisor, Dr. Masahiro Ikoma. He has supported and encouraged me so patiently at any time. Without his advice and instructive comments, I would not be able to complete my thesis and PhD program. He is a respectable scientist for physics and I want to be a researcher like him.

I am also deeply grateful to examiners of my PhD thesis, Dr. Seiji Sugita, Dr. Keiji Ohtsuki, Dr. Eiichiro Kokubo, Dr. Aki Takigawa and Dr. Tomokatsu Morota. They reviewed my PhD thesis and gave me the useful discussions. My PhD thesis is completed with their great advises.

I would like to express special thanks to Dr. Ravit Helled. She managed my stay in Zurich and gave me fruitful advises and discussions about works in Zurich. She has motivated and encouraged me to work on this study.

I would like to express my gratitude to the following people. Dr. Hiroshi Kobayashi gave fruitful discussions regarding modelling collision of planetesimals. I am grateful to Dr. Shigeru Ida for kindly providing me the advises about the treatment of mean motion resonances.

I would like to thank Dr. S. Tachibana, Dr. S. Kasahara, Dr. H. Kawahara, and Dr. A. Fukui for fruitful comments and suggestions to this thesis. I am grateful to the members of the research group, Dr. T. Kodama, Dr. M. Kunitomo, Dr. K. Kurosaki, Dr. S. Kadoya, Dr. Y. Ito, Dr. Y. Kawashima, Dr. A. Nakayama, Dr. K. Kawauchi, Dr. Y. Aoyama, Mr. M. Mitsumoto, Mr. N. Hasegawa, Ms. M. Ozawa, Mr. T. Kimura, Mr. T. Tajiri, Mr. K. Kikuchi, S. Inaba and S. Kurita. Without their encouragement, this thesis would not completed. I also thank Mr. Y. Shirai, who studied the planetesimal accretion onto gas giant planets before I joined Ikoma laboratory. He and Dr. T. Kodama gave me a chance to study the field of planetesimal accretion.

I also express my appreciation to Dr. Y. Abe, Dr. H. Nagahara, Dr. R. Tada, Dr. E. Tajika, Dr. M. Ogawa, Dr. Y. Sekine, Dr. S. Takahashi, Dr. N. Moteki, and Dr. K. Kawai for educations and encouragements.

I further would like to thank other L-seminer members and members in my student rooms 720 and 721. Finally, I would like to show my heartfelt appreciation to my family for supporting and encouraging me over the years.

My PhD program was supported by Leading Graduate Course for Frontiers of Mathematical Sciences and Physics, JSPS Core-to-Core Program “International Network of Planetary Sciences (Planet2)” and JSPS KAKENHI Grant Numbers 17H01153 and 18H05439. Some of this work has been carried out within the framework of the National Centre for Competence in Research PlanetS, supported by the Swiss National Foundation. Numerical computations were carried out on the Cray XC50 at the Center for Computational Astrophysics, National Astronomical Observatory of Japan. I also express my gratitude to

these programs and people managing these programs.

Sho Shibata

Appendix A

Benchmark test of our orbital integration code

We summarise the result of benchmark test of our orbital integration code shown in Shibata & Ikoma (2019). We integrate the equation of motion using the forth-order-Hermite integration scheme (Makino & Aarseth 1992). For timestep Δt, we adopt the method of Aarseth (1985), namely

$$\Delta t = \eta_{\rm ts} \sqrt{\frac{|\mathbf{a}||\mathbf{a}^{(2)}| + |\dot{\mathbf{a}}|^2}{|\dot{\mathbf{a}}||\mathbf{a}^{(3)}| + |\mathbf{a}^{(2)}|^2}}, \tag{A.1}$$

where $\mathbf{a}$ is the acceleration of the planetesimal ($= \ddot{r}_{\rm pl}$), $\mathbf{a}^{(k)}$ is the kth derivative of $\mathbf{a}$, and $\eta_{\rm ts}$ is an accuracy controlling parameter.

To determine the appropriate value of $\eta_{\rm ts}$, we perform a benchmark test, where we consider a Jupiter-mass planet in a circular Keplerian orbit and integrate the motion of test particles that orbit a central star of solar mass. We distribute the planetesimals inside the feeding zone and check energy errors during numerical integration; the energy error is defined as

$$\Delta E_{\rm err} \equiv \frac{|E_{\rm jacobi} - E_{\rm jacobi,0}|}{E_{\rm jacobi,0}}, \tag{A.2}$$

where $E_{\rm jacobi,0}$ is the initial Jacobi energy of the particle. The energy error comes from two components, the gravitational force of the central star and that of the protoplanet. The relative distance from the central star is almost constant and the energy error accumulates linearly with time. On the other hand, the relative distance from the protoplanet changes largely and the energy error depends on the distance of the closest encounter. We check the each component considering the cases of with and without close encounters with the protoplanet. Figure A.1 shows the some of the results of numerical integration. The upper panels show the change in the energy error during numerical integration. The lower panels show the change in the relative distance between the particle and the planet. The left column shows the results for the case where the particle experiences no close encounter with the planet, whereas the right column shows the results for the case where the particle does so. In the case with no close encounter, the energy error accumulates linearly with time and it is expected that the energy error would be suppressed smaller than $\sim 10^{-7}$ after the 10^5yrs integration. On a close encounter with the planet, the energy error increases sharply and its magnitude depends on the distance. It turns out that increase in energy error due to close

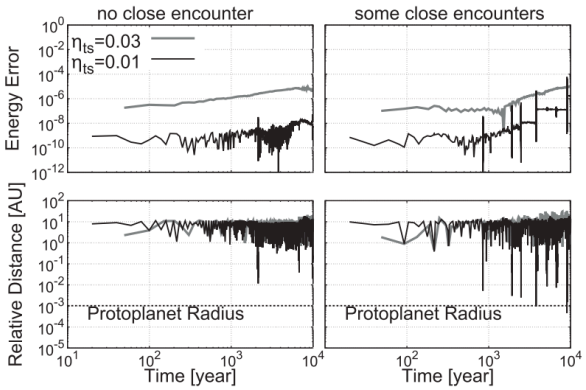

Figure A.1: A benchmark test of our orbital integration code from Shibata & Ikoma (2019). The upper two panels show the change in energy error defined by A.2. The lower two panels show the change in the relative distance between the particle and planet. The planet never experiences any close encounter with the planet in the case shown by the left panels, whereas the planet does so several times in the case shown by the right panels. The black and grey lines show the results for $\eta_{\rm ts} = 0.01$ and 0.03, respectively.

encounters is suppressed to as small as $\sim 10^{-7}$ for $\eta_{\rm ts} = 0.01$, if $r_{\rm pl,p} > 10^{-3}$AU. In our numerical study, all particles getting inside the radius of the planet are removed from the calculation. Thus, setting the accuracy-controlling parameter as $\eta_{\rm ts} = 0.01$ and considering the expanding envelope which has a mean density of $0.125{\rm g/cm^3}$, the maximum energy error in the end of our simulation is as small as $\sim 10^{-7}$.

Appendix B

Geometrical picture used in Adachi et al. (1976)

To calculate the relative velocity $\mathbf{u}$, we consider an orbital system of cylindrical coordinates (R, ψ, ζ), in which ζ-axis is perpendicular to the target planetesimal's orbit. The position of target planetesimal is given as

$$r_{\mathrm{tg,R}} = \frac{a(1-e^2)}{1+e\cos\psi}\cos\psi, \tag{B.1}$$

$$r_{\mathrm{tg},\psi} = \frac{a(1-e^2)}{1+e\cos\psi}\sin\psi, \tag{B.2}$$

$$r_{\mathrm{tg},\zeta} = 0. \tag{B.3}$$

The velocity of target planetesimal is given as

$$v_{\mathrm{tg,R}} = v_{\mathrm{K}}(a)\frac{e\sin\psi}{(1-e^2)^{1/2}}, \tag{B.4}$$

$$v_{\mathrm{tg},\psi} = v_{\mathrm{K}}(a)\frac{1+e\cos\psi}{(1-e^2)^{1/2}}, \tag{B.5}$$

$$v_{\mathrm{tg},\zeta} = 0. \tag{B.6}$$

The velocity of planetesimal swarm is given as

$$v_{\mathrm{imp,R}} = 0, \tag{B.7}$$

$$v_{\mathrm{imp},\psi} = v_{\mathrm{K}}(l)\sin\varepsilon, \tag{B.8}$$

$$v_{\mathrm{imp},\zeta} = -v_{\mathrm{K}}(l)\cos\varepsilon, \tag{B.9}$$

where l is the radial distance from the central star in the circumstellar disk. ε is an angle defined by both orbital plains given by

$$\sin\varepsilon = \frac{\cos i}{\cos\delta}, \tag{B.10}$$

$$\cos\varepsilon = \sin i\frac{\cos(\psi+\varpi)}{\cos\delta}, \tag{B.11}$$

$$\cos\delta = \frac{l}{r} = \frac{l}{a}\frac{1+e\cos\psi}{1-e^2}, \tag{B.12}$$

where r is the distance of target planetesimal from the central star. From above equations, we get $\mathbf{u}$ in (R, ψ, ζ) coordinate

$$u_{\mathrm{R}} = v_{\mathrm{tg,R}} - v_{\mathrm{imp,R}}, \tag{B.13}$$

$$u_{\psi} = v_{\mathrm{tg},\psi} - v_{\mathrm{imp},\psi}, \tag{B.14}$$

$$u_{\zeta} = v_{\mathrm{tg},\zeta} - v_{\mathrm{imp},\zeta}. \tag{B.15}$$

$$\tag{B.16}$$

References

Aarseth, S. J. 1985, in IAU Symposium, Vol. 113, Dynamics of Star Clusters, ed. J. Goodman & P. Hut, 251–258

Adachi, I., Hayashi, C., & Nakazawa, K. 1976, Progress of Theoretical Physics, 56, 1756

Alibert, Y., Mordasini, C., Benz, W., & Winisdoerffer, C. 2005, Astronomy and Astrophysics, 434, 343

Andrews, S. M., Wilner, D. J., Hughes, A. M., Qi, C., & Dullemond, C. P. 2010, Astrophysical Journal, 723, 1241

Arakawa, M., Leliwa-Kopystynski, J., & Maeno, N. 2002, Icarus, 158, 516

Armitage, P. J., Eisner, J. A., & Simon, J. B. 2016, The Astrophysical Journal Letters, 828

Batygin, K. 2015, Monthly Notices of the Royal Astronomical Society, 451, 2589

Batygin, K. & Laughlin, G. 2015, Proceedings of the National Academy of Sciences of the United States of America, 112, 4214

Benz, W. & Erik, A. 1999, Icarus, 142, 5

Bitsch, B., Izidoro, A., Johansen, A., et al. 2019, Astronomy & Astrophysics, 623, A88

Bitsch, B., Lambrechts, M., & Johansen, A. 2015, Astronomy & Astrophysics, 582, A112

Bitsch, B., Morbidelli, A., Johansen, A., et al. 2018, Astronomy & Astrophysics, 612, 30

Bolton, S. J., Adriani, A., Adumitroaie, V., et al. 2017, Science, 356, 821

Booth, R. A., Clarke, C. J., Madhusudhan, N., & Ilee, J. D. 2017, Monthly Notices of the Royal Astronomical Society, 469, 3994

Booth, R. A. & Ilee, J. D. 2019, Monthly Notices of the Royal Astronomical Society, 487, 3998

Boss, A. P. 1997, Science, 276, 1836

Boss, A. P. 2019, The Astrophysical Journal, 884, 56

Briceño, C., Vivas, A. K., Calvet, N., et al. 2001, Science, 291, 93

Brouwers, M. G., Vazan, A., & Ormel, C. W. 2018, Astronomy & Astrophysics, 611, A65

Cameron, A. G. W. 1978, The Moon and the Planets, 18, 5

Davis, D. R. & Ryan, E. V. 1990, Icarus, 83, 156

Dermott, S. F., Malhotra, R., & Murray, C. D. 1988, icarus, 76, 295

Drążkowska, J., Alibert, Y., & Moore, B. 2016, Astronomy and Astrophysics, 594, 105

Duffell, P. C., Haiman, Z., Macfadyen, A. I., D'orazio, D. J., & Farris, B. D. 2014, The Astrophysical Journal Letters, 792, 10

Duffell, P. C. & Macfadyen, A. I. 2013, The Astrophysical Journal, 769, 41

Dürmann, C. & Kley, W. 2015, Astronomy & Astrophysics, 574, A52

Fabrycky, D. C., Lissauer, J. J., Ragozzine, D., et al. 2014, Astrophysical Journal, 790, 146

Fujiwara, A., Cerroni, P., Davis, D. R., et al. 1989, in Asteroids II, ed. R. P. Binzel, T. Gehrels, & M. S. Matthews, 240–265

Fung, J., Shi, J.-M., & Chiang, E. 2014, The Astrophysical Journal, 782, 88

Gardner, J. P., Mather, J. C., Clampin, M., et al. 2006, Space Science Reviews, 123, 485

Ginzburg, S. & Chiang, E. 2020, Monthly Notices of the Royal Astronomical Society, 498, 680

Goldreich, P. 1965, Monthly Notices of the Royal Astronomical Society, 130, 159

Goldreich, P. & Schlichting, H. E. 2014, The Astronomical Journal, 147, 32

Goldreich, P. & Tremaine, S. 1980, ApJ, 241, 425

Greenberg, R., Wacker, J. F., Hartmann, W. K., & Chapman, C. R. 1978, Icarus, 35, 1

Greenzweig, Y. & Lissauer, J. J. 1992, Icarus, 100, 440

Guillot, T. 1999, Planetary and Space Science, 47, 1183

Guillot, T., Miguel, Y., Militzer, B., et al. 2018, Nature, 555, 227

Guillot, T., Santos, N. C., Pont, F., et al. 2006, Astronomy & Astrophysics, 453, L21

Guillot, T., Stevenson, D. J., Hubbard, W. B., & Saumon, D. 2004, Jupiter. The planet, satellites and magnetosphere., 35

Haisch, Jr., K. E., Lada, E. A., & Lada, C. J. 2001, The Astrophysical Journal, 553, L153

Hands, T. O. & Alexander, R. D. 2016, Monthly Notices of the Royal Astronomical Society, 456, 4121

Hands, T. O. & Alexander, R. D. 2018, Monthly Notices of the Royal Astronomical Society, 474, 3998

Hands, T. O., Alexander, R. D., & Dehnen, W. 2014, Monthly Notices of the Royal Astronomical Society, 445, 749

Hasegawa, Y., Bryden, G., Ikoma, M., Vasisht, G., & Swain, M. 2018, The Astrophysical Journal, 865, 32

Hasegawa, Y., Hansen, B. M. S., & Vasisht, G. 2019, The Astrophysical Journal, 876, L32

Hayashi, C. 1981, Progress of Theoretical Physics Supplement, 70, 35

Hayashi, C., Nakazawa, K., & Adachi, I. 1977, Publication of Astronomical Society of Japan, 29, 163

Helled, R. 2019, in Oxford Research Encyclopedia of Planetary Science (Oxford University Press)

Hillenbrand, L. A., Carpenter, J. M., Kim, J. S., et al. 2008, The Astrophysical Journal, 677, 630

Hori, Y. & Ikoma, M. 2011, Monthly Notices of the Royal Astronomical Society, 416, 1419

Ida, S. & Lin, D. N. C. 2004a, The Astrophysical Journal, 604, 388

Ida, S. & Lin, D. N. C. 2004b, The Astrophysical Journal, 616, 567

Ida, S. & Lin, D. N. C. 2005, The Astrophysical Journal, 626, 1045

Ida, S. & Lin, D. N. C. 2008, The Astrophysical Journal, 685, 584

Ida, S. & Lin, D. N. C. 2010, The Astrophysical Journal, 719, 810

Ida, S. & Nakazawa, K. 1989, Astronomy & Astrophysics, 220, 293

Ida, S., Tanaka, H., Johansen, A., Kanagawa, K. D., & Tanigawa, T. 2018, The Astrophysical Journal, 864, 77

Ikoma, M., Guillot, T., Genda, H., Tanigawa, T., & Ida, S. 2006, The Astrophysical Journal, 650, 1150

Ikoma, M., Nakazawa, K., & Emori, H. 2000, The Astrophysical Journal, 537, 1013

Inaba, S. & Ikoma, M. 2003, Astronomy & Astrophysics, 410, 711

Johansen, A. & Lambrechts, M. 2017, Annual Review of Earth and Planetary Sciences, 45, 359

Johansen, A., Youdin, A. N., & Mac Low, M. M. 2009, Astrophysical Journal, 704, 75

Kanagawa, K. D., Muto, T., Tanaka, H., et al. 2016, Publications of the Astronomical Society of Japan, 68, 43

Kanagawa, K. D., Tanaka, H., Muto, T., & Tanigawa, T. 2017, Publications of the Astronomical Society of Japan, 69

Kanagawa, K. D., Tanaka, H., Muto, T., Tanigawa, T., & Takeuchi, T. 2015, Monthly Notices of the Royal Astronomical Society, 448, 994

Kanagawa, K. D., Tanaka, H., & Szuszkiewicz, E. 2018, The Astrophysical Journal, 861, 140

Kary, D. M. & Lissauer, J. J. 1995, Icarus, 117, 1

Kary, D. M., Lissauer, J. J., & Greenzweig, Y. 1993, Icarus, 106, 288

Klahr, H., Pfeil, T., & Schreiber, A. 2018, in Handbook of Exoplanets, 2251–2286

Kobayashi, H. & Tanaka, H. 2010, Icarus, 206, 735

Kobayashi, H. & Tanaka, H. 2018, The Astrophysical Journal, 862, 127

Kobayashi, H., Tanaka, H., & Krivov, A. V. 2011, Astrophysical Journal, 738, 35

Kobayashi, H., Tanaka, H., Krivov, A. V., & Inaba, S. 2010, Icarus, 209, 836

Kobayashi, H., Tanaka, H., & Okuzumi, S. 2016, The Astrophysical Journal, 817, 105

Kokubo, E. & Ida, S. 1996, Icarus, 123, 180

Kokubo, E. & Ida, S. 1998, Icarus, 131, 171

Kokubo, E. & Ida, S. 2000, Icarus, 143, 15

Kokubo, E. & Ida, S. 2002, The Astrophysical Journal, 581, 666

Kostov, V. B., Orosz, J. A., Welsh, W. F., et al. 2016, The Astrophysical Journal, 827, 86

Kuiper, G. P. 1951, Proceedings of the National Academy of Sciences, 37, 1

Kurokawa, H. & Tanigawa, T. 2018, Monthly Notices of the Royal Astronomical Society, 479, 635

Lambrechts, M. & Johansen, A. 2012, Astronomy & Astrophysics, 544, A32

Lambrechts, M., Lega, E., Nelson, R. P., Crida, A., & Morbidelli, A. 2019, Astronomy & Astrophysics, 630, A82

Leinhardt, Z. M. & Stewart, S. T. 2009, Icarus, 199, 542

Lenz, C. T., Klahr, H., & Birnstiel, T. 2019, The Astrophysical Journal, 874, 36

Levison, H. F., Thommes, E., & Duncan, M. J. 2010, Astronomical Journal, 139, 1297

Lin, D. N. C. & Ida, S. 1997, The Astrophysical Journal, 477, 781

Lin, D. N. C. & Papaloizou, J. 1979, Monthly Notices of the Royal Astronomical Society, 186, 799

Lin, D. N. C. & Papaloizou, J. C. B. 1993, in Protostars and Planets III, ed. E. H. Levy & J. I. Lunine, 749–835

Lissauer, J. J., Hubickyj, O., D'Angelo, G., & Bodenheimer, P. H. 2009, Icarus, 199, 338

Liu, S. F., Agnor, C. B., Lin, D. N., & Li, S. L. 2015, Monthly Notices of the Royal Astronomical Society, 446, 1685

Liu, S.-F., Hori, Y., Müller, S., et al. 2019, Nature, 572, 355

Lynden-Bell, D. & Pringle, J. E. 1974, Monthly Notices of the Royal Astronomical Society, 168, 603

Machida, M. N., Kokubo, E., Inutsuka, S.-I., & Matsumoto, T. 2010, Monthly Notices of the Royal Astronomical Society, 405, 1227

Madhusudhan, N. 2019, Annual Review of Astronomy and Astrophysics, 57, 617

Madhusudhan, N., Amin, M. A., & Kennedy, G. M. 2014, The Astrophysical Journal Letters, 794, 12

Madhusudhan, N., Bitsch, B., Johansen, A., & Eriksson, L. 2017, Monthly Notices of the Royal Astronomical Society, 469, 4102

Makino, J. & Aarseth, S. J. 1992, Publications of the Astronomical Society of Japan, 44, 141

Malhotra, R. 1993a, Icarus, 106, 264

Malhotra, R. 1993b, Nature, 365, 819

Miller, N. & Fortney, J. J. 2011, The Astrophysical Journal, 736, L29

Mizuno, H. 1980, Progress of Theoretical Physics, 64, 544

Morbidelli, A. & Nesvorny, D. 2012, Astronomy & Astrophysics, 546, A18

Mordasini, C. 2014, Astronomy & Astrophysics, 572, A118

Mordasini, C. 2018, in Handbook of Exoplanets, 2425–2474

Mordasini, C., Alibert, Y., & Benz, W. 2006, in Tenth Anniversary of 51 Peg-b: Status of and prospects for hot Jupiter studies, ed. L. Arnold, F. Bouchy, & C. Moutou, 84–86

Mordasini, C., Alibert, Y., & Benz, W. 2009a, Astronomy & Astrophysics, 501, 1139

Mordasini, C., Alibert, Y., Benz, W., & Naef, D. 2009b, Astronomy & Astrophysics, 501, 1161

Mordasini, C., Van Boekel, R., Mollière, P., Henning, T., & Benneke, B. 2016, The Astrophysical Journal, 832

Müller, S., Ben-Yami, M., & Helled, R. 2020, The Astrophysical Journal, 903, 147

Murray, C. D. & Dermott, S. F. 1999, Solar system dynamics

Ndugu, N., Bitsch, B., & Jurua, E. 2018, Monthly Notices of the Royal Astronomical Society, 474, 886

Nesvorný, D., Youdin, A. N., & Richardson, D. C. 2010, The Astronomical Journal, 140, 785

Nettelmann, N. 2017, Astronomy & Astrophysics, 606, A139

Noll, K. S., Grundy, W. M., Chiang, E. I., Margot, J. L., & Kern, S. D. 2008, Binaries in the Kuiper Belt, ed. M. A. Barucci, H. Boehnhardt, D. P. Cruikshank, A. Morbidelli, & R. Dotson, 345

Notsu, S., Eistrup, C., Walsh, C., & Nomura, H. 2020, Monthly Notices of the Royal Astronomical Society, 499, 2229

Ohtsuki, K., Stewart, G. R., & Ida, S. 2002, Icarus, 155, 436

Okuzumi, S., Tanaka, H., Kobayashi, H., & Wada, K. 2012, Astrophysical Journal, 752, 106

Ormel, C. W. & Klahr, H. H. 2010, Astronomy & Astrophysics, 520, 43

Paardekooper, S.-J., Baruteau, C., Crida, A., & Kley, W. 2010, Monthly Notices of the Royal Astronomical Society, 401, 1950

Perri, F. & Cameron, A. G. W. 1974, Icarus, 22, 416

Pichierri, G. & Morbidelli, A. 2020, Monthly Notices of the Royal Astronomical Society, 494, 4950

Pitjeva, E. V. & Pitjev, N. P. 2018, Astronomy Letters, 44, 554

Pollack, J. B., Hubickyj, O., Bodenheimer, P., et al. 1996, Icarus, 124, 62

Rafikov, R. R. 2005, The Astrophysical Journal, 621, L69

Saumon, D. & Guillot, T. 2004, The Astrophysical Journal, 609, 1170

Shakura, N. I. & Sunyaev, R. A. 1973, Astronomy & Astrophysics, 24, 337

Shibata, S., Helled, R., & Ikoma, M. 2020, A&A, 633, 13

Shibata, S. & Ikoma, M. 2019, Monthly Notices of the Royal Astronomical Society, 487, 4510

Shiraishi, M. & Ida, S. 2008, The Astrophysical Journal, 684, 1416

Simon, J. B., Armitage, P. J., Li, R., & Youdin, A. N. 2016, The Astrophysical Journal, 822, 55

Sugiura, K., Kobayashi, H., & Inutsuka, S. 2018, Astronomy & Astrophysics, 620, A167

Tajima, N. & Nakagawa, Y. 1997, Icarus, 126, 282

Tanaka, H. & Ida, S. 1997, Icarus, 125, 302

Tanaka, H. & Ida, S. 1999, Icarus, 139, 350

Tanaka, H., Inaba, S., & Nakazawa, K. 1996, Icarus, 123, 450

Tanaka, H., Murase, K., & Tanigawa, T. 2020, The Astrophysical Journal, 891, 143

Tanaka, H., Takeuchi, T., & Ward, W. R. 2002, The Astrophysical Journal, 565, 1257

Tanigawa, T. & Ikoma, M. 2007, The Astrophysical Journal, 667, 557

Tanigawa, T., Maruta, A., & Machida, M. N. 2014, The Astrophysical Journal, 784, 109

Tanigawa, T. & Tanaka, H. 2016, The Astrophysical Journal, 823, 48

Tanigawa, T. & Watanabe, S.-I. 2002, The Astrophysical Journal, 580, 506

Thorngren, D. P., Fortney, J. J., Murray-Clay, R. A., & Lopez, E. D. 2016, The Astrophysical Journal, 831, 64

Tinetti, G., Drossart, P., Eccleston, P., et al. 2018, Experimental Astronomy, 46, 135

Venturini, J., Alibert, Y., & Benz, W. 2016, Astronomy & Astrophysics, 596, A90

Venturini, J., Alibert, Y., Benz, W., & Ikoma, M. 2015, Astronomy & Astrophysics, 576, 114

Wahl, S. M., Hubbard, W. B., Militzer, B., et al. 2017, Geophysical Research Letters, 44, 4649

Walsh, K. J., Morbidelli, A., Raymond, S. N., O'Brien, D. P., & Mandell, A. M. 2011, Nature, 475, 206

Ward, W. R. 1986, Icarus, 67, 164

Ward, W. R. 1989, The Astrophysical Journal, 345, L99

Ward, W. R. 1997, Icarus, 126, 261

Ward, W. R. & Hahn, J. M. 1995, The Astrophysical Journal, 440, L25

Wetherill, G. & Stewart, G. 1993, Icarus, 106, 190

Wetherill, G. W. & Stewart, G. R. 1989, Icarus, 77, 330

Windmark, F., Birnstiel, T., Güttler, C., et al. 2012, Astronomy & Astrophysics, 540, A73

Youdin, A. N. & Goodman, J. 2005, The Astrophysical Journal, 620, 459

Youdin, A. N. & Shu, F. H. 2002, The Astrophysical Journal, 580, 494

Yu, Q. & Tremaine, S. 2001, The Astronomical Journal, 121, 1736

Zhou, J. & Lin, D. N. C. 2007, The Astrophysical Journal, 666, 447